Planning and Evaluation of Radio-Therapeutic Treatment of Head-and-Neck Cancer Using PET/CT scanning

Hollensen, Christian

Publication date:
2012

Document Version
Publisher's PDF, also known as Version of record

Planning and Evaluation of Radio-Therapeutic Treatment of Head-and-Neck Cancer Using PET/CT scanning

Christian Hollensen

Kongens Lyngby 2012
IMM-PHD-2012-277

Technical University of Denmark
Informatics and Mathematical Modelling
Building 321, DK-2800 Kongens Lyngby, Denmark
Phone +45 45253351, Fax +45 45882673
reception@imm.dtu.dk
www.imm.dtu.dk

IMM-PHD: ISSN 0909-3192

Summary

Radiation therapy relies in great extent on delineations of tumour and organs on medical images. These delineations are essential for the entire treatment. Unfortunately manual delineations are both prone to variation. At the same time the manual delineation process is time-consuming. This thesis represents a work within the automatic definition of organs and tumours. The thesis includes a description of cancer and radiation therapy as well as a summary of the prior methods employed for automatic segmentation. Variation within and between manual and automatic segmentation methods is documented in the thesis. The first included article of the thesis analyses treatment outcome difference due to manual delineation variation. 3 articles follow, which describes automatic segmentation algorithms of different areas of application for radiation therapy.

Resumé

Strålebehandling afhænger i høj grad af indtegning af organer og tumor på medicinske billeder. Disse indtegninger er afgørende for behandlingen. Imidlertid er disse manuelle indtegninger følsomme overfor variation mellem indtegnere. Samtidig er manuelle indtegninger tidskrævende. Denne afhandling omhandler arbejde inden for automatisk definition af organer og tumorer. Afhandlingen omfatter en beskrivelse af kræft og strålebehandling samt et resumé af de kendte metoder til automatisk indtegning. Variation imellem manuelle og automatiske segmentering metoder er dokumenteret i afhandlingen. Den første omfattede artikel i afhandlingen analyserer resultatet i behandling på grund af manuel indtegningsvariation. 3 artikler følger, som beskriver automatiske indtegningsalgoritmer til anvendelse indenfor forskellige områder af strålebehandling.

Preface

This thesis was prepared and finished at Rigshospitalet and at the Department of Informatics and Mathematical Modelling, the Technical University of Denmark in fulfilment of the requirements for acquiring the Ph.D. degree in engineering. The thesis deals with different aspects within radiotherapy and image analysis. The thesis consists of a summary report and a collection of four research papers written during the period 2009–2012.
The thesis starts out with a general introduction. In the next chapter some of the methods used in the included papers are discussed along with the future possibilities for automatic image segmentation in radiotherapy.
Hereafter follows the four papers which are the foundation of the thesis, first a paper describing the variation of manual contours and its impact on treatment planning, secondly a paper describing an automatic method for the segmentation of the parotid gland, thirdly a paper describing the segmentation of gross tumour volume using symmetry and lastly a paper describing the continuous segmentation of lung tumours using electric flow lines for graph cuts.

Lyngby, November 2012

Christian Hollensen

Papers included in the thesis

- Christian Hollensen, Gitte Persson, Liselotte Højgaard, Lena Specht, and Rasmus Larsen. Differences in radiotherapy delivery and outcome due to contouring variation. *Lecture Notes in Computer Science - MICCAI Workshop on Clinical Image-based Procedures: From Planning to Intervention*, 2012.

- Christian Hollensen, Mads Fogtmann Hansen, Liselotte Højgaard, Lena Specht, and Rasmus Larsen. Segmenting the parotid gland using registration and level set methods. *Proceedings from the 13th International Conference on Medical Image Computing and Computer Assisted Intervention, Medical Image Analysis for the Clinic: A Grand Challenge*, 305-312, 2010.

- Christian Hollensen, Liselotte Højgaard, Lena Specht, and Rasmus Larsen. Segmentation using symmetry. *IEEE transactions on Medical Imaging.* (submitted)

- Christian Hollensen, George Cannon, Donald Cannon, Søren Bentzen, and Rasmus Larsen. Lung Tumor Segmentation Using Electric Flow Lines for Graph Cuts. *Lecture Notes in Computer Science, Image Analysis and Recognition*, 7325:206–213, 2012.

Acknowledgements

I first and foremost wish to express my utter thanks to my supervisor Rasmus Larsen at the Department of Informatics and Mathematical Modelling at the Technical University of Denmark. Our discussions, his overview of image analysis and his patience for a Ph.D.-student within the world of radiation therapy heightened the level of this thesis.
I sincerely want to thank both Liselotte Højgaard and Lena Specht for being part of this project and giving me valuable feedback from a clinical point of view.
Furthermore I would like to thank the people at University of Wisconsin and especially Søren Bentzen for providing me with the chance to go to the University of Wisconsin.
Likewise I also want to extend my thanks to all my coauthors who has been patiently contributing and involving themselves.
I would also like to thank my wonderful colleagues at both Rigshospitalet and the Technical University of Denmark. For their patience and hand whenever I needed it.
Lastly I would like to give a warm and special thanks to my family who provided me with help when I was needing it the most and especially my father for his help in preparation of the thesis.

Accronyms

Abbreviations

AAM Active Appearance Model

ASM Active Shape Model

CC Cross-Correlation

CTV Clinical Target Volume

GTV Gross Tumour Volume

HN Head and Neck

MRI Magnetic Resonance Imaging

NMI Normalized Mutual Information

NTCP Normal Tissue Complication Probability

OAR Organ at Risk

PET Positron Emission Tomography

PRV Planning Organ at Risk Volume

PTV Planning Target Volume

SSD Sum of Square Difference

TCP Tumour Control Probability

VOI Volume Of Interest

Mathematical Symbols

α Dose Confidence Level Factor from systematic error

$\alpha(v)$ Cell surval term

a Affine transformation parameter

A Transformation matrix

AIV Average Intensity Volume

β Dose Confidence Level Factor from random error

CC Cross-Correlatio

D Dissimilarity measure

$D(v)$ Dose given to voxel v

E Electric potential

ΔF Symmetric Functional Difference

I Image

J Jacobian

NR Non-Rigid Transformation

Φ Cumulative Probability Distribution

Q Surface Function

ρ Cell density

r Direction vector

σ Standard deviation of random error

Σ Standard deviation of systematic error

s Voxel size

θ Rotation transformation parameter

t Translation transformation parameter

v Volume size

ΔVol Symmetric Volume Expansion Difference

w Weighting Parameter

x Coordinate

$\tilde{x}$ Transformed coordinate

Contents

Summary i

Resumé iii

Preface v

Papers included in the thesis vii

Acknowledgements ix

Accronyms xi

1 Introduction 1
- 1.1 Cancer . . . 2
- 1.2 Imaging Modalities . . . 8
- 1.3 Radiation therapy . . . 17
- 1.4 Manual Contours . . . 28
- 1.5 Segmentation of Normal Tissue . . . 32
- 1.6 Segmentation of Gross Tumor Volume . . . 39

2 Contributions 45
- 2.1 Differences in Radiotherapy Delivery and Outcome Due to Contouring Variation . . . 45
- 2.2 Segmenting the Parotid Gland Using Registration and Level Set Methods . . . 46
- 2.3 Segmentation Using Symmetry . . . 47
- 2.4 Lung Tumor Segmentation Using Electric Flow Lines for Graph Cuts . . . 48
- 2.5 General Perspective . . . 49

3 Conclusion **53**

4 Differences in Radiotherapy Delivery and Outcome Due to Contouring Variation **57**
4.1 Abstract . . . 57
4.2 Introduction . . . 58
4.3 Methods . . . 59
4.4 Results . . . 62
4.5 Discussion . . . 63
4.6 Conclusion . . . 64

5 Segmenting the Parotid Gland Using Registration and Level Set Methods **67**
5.1 Abstract . . . 67
5.2 Introduction . . . 67
5.3 Data . . . 68
5.4 Methods . . . 69
5.5 Results . . . 71
5.6 Discussion . . . 74
5.7 Conclusions . . . 75

6 Segmentation Using Symmetry **79**
6.1 Abstract . . . 79
6.2 Introduction . . . 80
6.3 Theory . . . 80
6.4 Experiments . . . 82
6.5 Results . . . 86
6.6 Discussion . . . 88
6.7 Conclusion . . . 92

7 Lung Tumor Segmentation Using Electric Flow Lines for Graph Cuts **95**
7.1 Abstract . . . 95
7.2 Introduction . . . 96
7.3 Methodology . . . 97
7.4 Results . . . 100
7.5 Discussion . . . 101
7.6 Conclusion . . . 103

A Further Contributions **105**
A.1 Journal Articles . . . 105
A.2 Conference Abstracts . . . 106

Chapter 1

Introduction

Computed tomography (CT) and positron emission tomography (PET) are modalities of increasing clinical application for radiation therapy. The combination of the images supplies the medical personnel with information about both anatomy and physiology. This information is indeed important in the clinical workflow of radiation therapy in the treatment of cancer.
Radiation therapy is a complex discipline which involves clinical personnel of many different professions, as nurses, chemists, physicists, dosimetrists as well as nuclear medicine physicians, radiation oncologists and radiologists. The inclusion of all these professions requires cooperation and understanding as well as a clear clinical workflow.
The process of planning and delivering radiation treatment requires images in all parts of the workflow. The different regions of interest are contoured on images, the dose delivery plan is optimized on the basis of images, quality assurance is based on images and the position of the patient is ensured using images.
With the introduction of new imaging technologies and the streamlining of older imaging modalities the amount of image data has increased dramatically. The increased amount of data increases the load of conventional manual methods in the clinic. This combined with the ever increasing demand on healthcare system to increase efficiency and quality without increasing costs has increased the demands for smarter procedures and application of technologies that reduces the workload of healthcare personnel.
Image analysis seems to be one of the solutions for this problem in radiation

therapy. Automatic segmentation can deliver quantitative contours and decrease the workload of physicians when contouring organs and pathologies on images. Registration can find points of correspondence between images of the same patient at different time points for treatment evaluation. Registration can also find points of correspondence between images of different patients allowing quantitative comparison between patients. Extraction of features of dose plans and manual contours also allows an evaluation of errors in the clinical workflow. The overall objective of this thesis is the examination of the applicability of image analysis for the analysis of CT and PET images in planning and evaluation of radiation therapy.

1.1 Cancer

Cancer is a multifaceted disease, which can occur in almost every part of the body. An elaborate description of cancer is outside the scope of this thesis. This section is meant as a short introduction to cancer. It describes some of the basic mechanisms of developing cancer as well as some of their characteristics[144]. The section ends with a description of the head and neck cancer volume, and why this subject is the main theme of the thesis.

1.1.1 Origin of cancer

Cancer is a disease that arises, when the cells of our body starts proliferating at an abnormal level without any regards to the normal boundaries within our body[144]. This state is called neoplasia, new (neo) formation/creation (plasia) in greek. Neoplasia is the last step of a change process, that a cell undergoes towards becoming a cancer cell, which can be seen sketched in figure 1.1. The process usually starts with stress,that damages the cell in some way. The stress can arise from heat, physical damage, infection, ionizing radiation, chemical interaction and the functions of the cell itself. In response to the irritation the cell repairs itself and typically goes into the state of metaplasia.
Metaplasia is a reversible process, where the cell changes (in greek: meta) from one type to another type, that is more capable of withstanding the stress. An example could be the interaction between the epithelium (surface) in the respiratory passages and cigarette smoke, which after chronic irritation changes into squamous epithelium, where the cells are more capable to resist the pathological interaction of the smoke. The degree of stress, which is necessary for a cell to change, is cell type dependent and also different from individual to individual. In general cells, which have a higher frequency of cell division, are

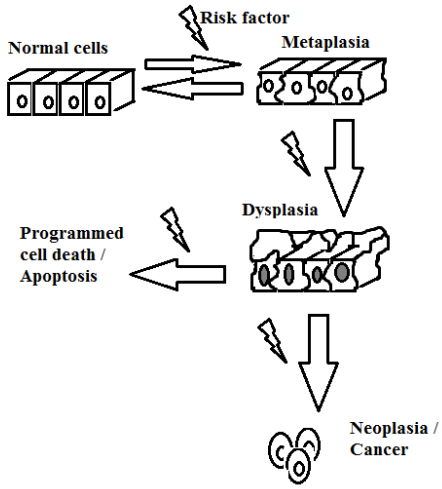

Figure 1.1: A general schematic of the pathway from normal cell to neoplasia.

more vulnerable to ionizing radiation. This is caused by the vulnerability of the cell DNA, when the cell is in the mitosis process, where the cell separates the chromosomes in the cell into two identical sets in two seperate nuclei. In this phase the DNA repair mechanisms are decreased, and the replication of DNA makes small changes even more risky.
A more persistent or severe stress or irritation of the cell can induce dysplasia (greek: malformation). Dysplasia is an irreversible alteration of the cell, and cells with signs of dysplasia are often categorized as a precursor of cancer by pathologists when seen with a microscope in a tissue sample. The cells with dysplasia have often lost some of their original characteristics. Cells with dysplasia will display unequal size and abnormal shape within same tissue, heightened levels of DNA in the cell and higher number of dividing cells.
There are several grades of dysplasia, going from mild disorder to a severe grade, which is hard to distinguish from neoplasia. The definition of dysplasia is dependent on site and on cell type. Cells with dysplasia do not necessary alter into neoplastic cells. It is dependent on the environment of the cells and their own DNA. If the alterations of the cell are too severe, it develops into a neoplasia, which we normally call cancer.
The mechanism, which alters a cell from one of the above mentioned states, are not fully understood. But it has been possible to identify environmental factors which promote the alterations such as excessive UV radiation, burned meat , smoking and certain vira, see figure 1.2. Even though these risk factors have been identified, their interaction and promotion of cell alterations are not

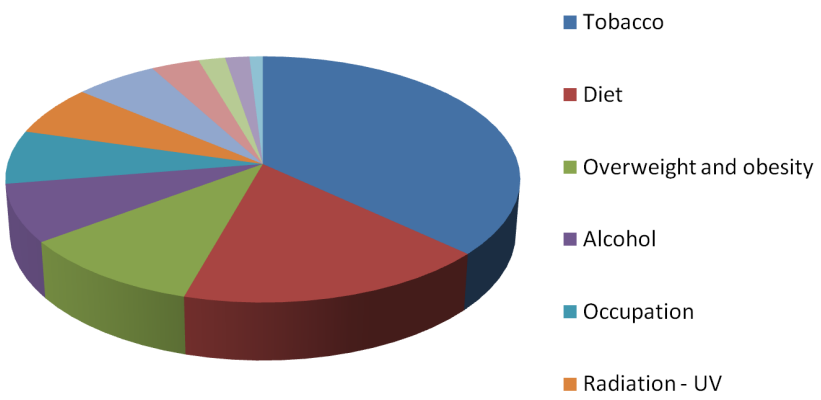

Figure 1.2: Percent of cancer cases in the UK attributable to different exposures. The pie does only account for 42.7 % of all incident cancer cases. [112]

always understood.

1.1.2 Genetics of cancer

Cancer cells lack some of the characteristics of normal cells, which would stop the cell from developing into uncontrolled growth[144]. The characteristics are generally related to either the development or activation of oncogenes on the DNA or the lack of tumour suppressor genes as it can be seen in figure 1.3. The oncogenes code for proteins that stimulate cell growth, differentiation and proliferation. These genes are then responsible for the uncontrolled rise in cell number and the differentiation of the cells. The increase in cancer cells can eventually spread the cancer and provide a pressure on surrounding tissue and tissue boundaries. The differentiation of the cell increases the alterations in DNA. These alterations can increase the number of oncogenes or deactivate tumor suppressor genes making the cancer even more dangerous. It can also alter the cell, so that it can survive in other environments, than it normally was supposed to, and change its appearance making it less vulnerable to the immune system.
The tumour suppressor genes are genes, which code for proteins, that repress genes, which are essential for the cell cycle, or couple the cell cycle to DNA damage, inhibiting cell division. Tumour suppressor genes include genes that code for DNA repair proteins, which can repair mutations on the DNA. The cell should normally initiate apoptosis (programmed cell death), if it does not succeed in repairing damage to the DNA. Some tumour suppressor genes are

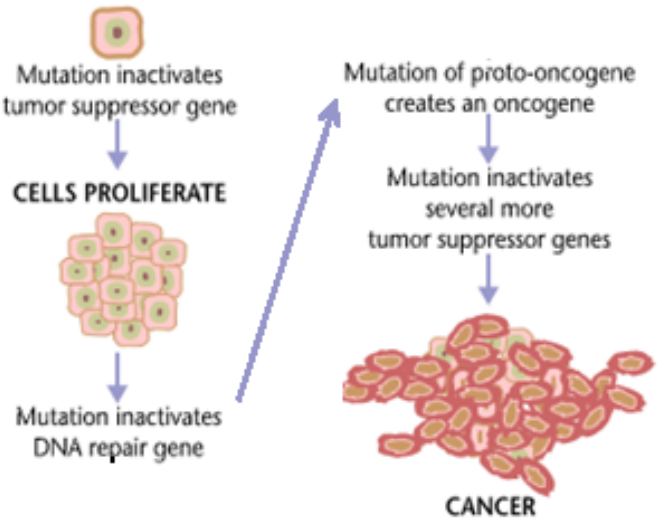

Figure 1.3: The mechanisms of cancer oncogenes and tumor suppressor genes modified from [112].

necessary for this initiation.
A last group of tumour suppressor genes code for adhesion proteins, that are responsible for cell adhesion, hereby inhibiting metastasis. As it can be seen, the loss or reduction of these functions will increase the risk of cancer.

1.1.3 Cancer spread

Cancer cells proliferate at an increased rate compared normal cells without any regard to its surroundings[144]. The growth will result in a mass of cell concentration, the tumour. The tumour cells will consume an increased amount of glucose to ensure the increased amount of cell proliferation. The cell growth of the tumour can even be so high, that it stops the supply-arteries for the core cells, either killing the cells or inducing a state of hypoxia, the deprivation of oxygen.
It is possible for the tumour to spread to nearby tissues by tumour growth into bordering tissue. It is also possible for cancer cells to spread to other tissues using the transport systems of the human body, which is called metastasis. The process of metastasis is complex and requires further mutations of the cancer

cell as inhibition of adhesion proteins and invasion of bordering nodes or blood vessels. Common sites and symptoms of metastasis are illustrated in figure 1.4. The lymph vessels of the immune system can be used by metastasising cells.

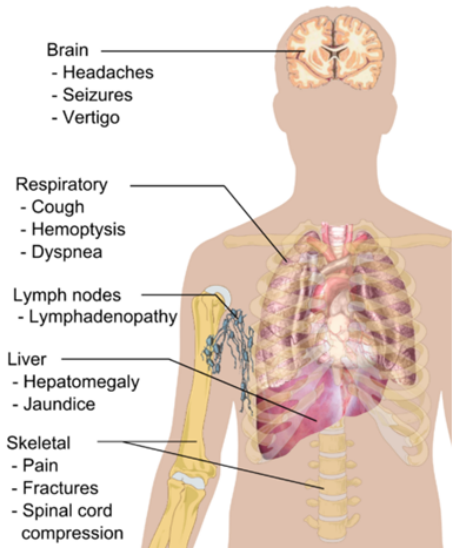

Figure 1.4: Common sites and symptoms of cancer metastasis [144].

The tumour cells can penetrate the boundaries of the nearby lymph nodes, and if the adhesion of the cells is lacking the cancer cells will spread through the lymph node. Since the lymph nodes are regional the cancer cells entering the lymph node can only spread to a certain volume of the body.
The cancer cells can also invade nearby veins or arteries. This allows the spread of the cancer cells to distant parts of the body. Cancer cells will usually have a difficulties surviving outside its original tissue. Accordingly metastasising cells will situate in organs with similar characteristics as their origin tissue.
Metastasis will usually decrease the probability of tumour management dramatically since it increases the spread of cancer and decreases the number of effective treatments.

1.1.4 Classification of cancer

Cancer is classified in multiple manners. The most common classification is between benign and malign tumours. Benign tumours are usually characterised by their lack of invasive properties. Usually a benign tumour has some kind of

sheath covering it. Even though benign tumours lack the invasive property they can provide a health risk by compression of vessels and vital tissue. Some benign tumours also possess the hormone secretion properties of its origin tissue and can pose a danger by oversecretion of these hormones. Malign tumours include all other cancer tumours and are typically more dangerous.
The TNM system describes the extent of cancer spread in the body[94]. T describes the primary tumour size, N the regional lymph nodes involved and M the metastasis spread.
The primary tumour size is ascribed from 0 to 4, where 0 signifies no sign of primary tumour and 4 is the largest possible extension of the tumour for involved tissue. The regional lymph node description is given from 0 to 3, where 0 signifies no nodal involvement and 3 is a spread to all regional nodes.
Metastasis is given as 0 or 1 respectively signifying none or present metastasis. Dependent on the primary tumour location all TNM classification has a direct correlation to the cancer staging system which ranges from 0 to 5. Stage 0 signifies a carcinoma in situ, i.e. cells which have the risk of development into cancer. Stage 5 denotes the spread of cancer to another organ.

1.1.5 World Cancer Burden

For the human race no one single disease is as encompassing as cancer. Cancer is one of the deadliest human diseases, responsible of 7.6 million deaths in 2008[1]. It is hereby responsible for 13 % of all deaths in the world. Furthermore there are over 12 million new incidences of cancer every year[86]. And the burden of cancer will increase further due to population growth and aging, and by 2030 the number of incidences is predicted to increase by 75 % relative to 2008[21].

1.1.6 Head and Neck cancer

Head and neck cancer is the main focus of this thesis. The volume of head and neck was chosen because of the difficulties mentioned below and the absence of tools to support the manual contourer of the tumour.
The head and neck volume includes the head and neck except the brain, esophagus (commonly known as the gullet) and the vertebrae. All tumours of this volume are normally classified to an origin in oral cavity, oropharynx, nasopharynx, hypopharynx and larynx. All the volumes can be seen in figure 1.5. The volume is characterized by predominantly soft tissue and a high density of vital organs. The first feature makes HN (Head and Neck) cancer extremely hard to delineate, since the edge contrast between different the soft tissues is difficult to perceive on the CT-scan. The second feature emphasizes the need for reliable

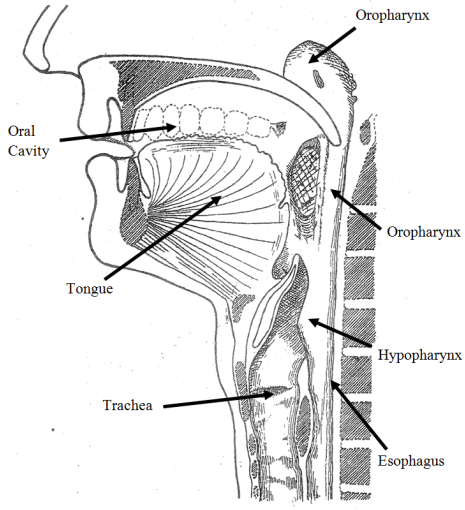

Figure 1.5: The anatomy of the head-and-neck volume. Illustration produced by Rigshospitalet for clinical purposes

contours of the gross tumour volume (GTV) as well as the normal tissues, which are vulnerable to the radiation, such as the spinal cord and the parotid glands. This is reflected in the fact that approximately 50 % of the patients are dead 5 years after treatment[74]. Another feature is the fact, that none of the delineations based on imaging modalities such as MR, CT and PET are capable of capturing the entire volume of gross tumour infiltration [35], and that the delineations are subject to large inter- and intra-operator variation [27][22][123] compared to other volumes[137].

1.2 Imaging Modalities

In this section a short description of the different image modalities is presented. The image modalities presented are part of the work included in this thesis as well as other imaging modalities of interest in radiotherapy.

1.2.1 Computed tomography (CT)

Computed tomography is built upon the principle of x-ray imaging. X-rays are photons with a wave length between 0.01 to 10 nanometers with energies rang-

ing from 100 eV to 100 keV. X-ray radiation is electromagnetic radiation.
X-rays are produced in an x-ray tube, as illustrated in figure 1.6 below. Inside the tube a vacuum exist with only two other components inside: a cathode and an anode. The cathode is a wire with a current, which is heated, and the anode is usually made from a material with a high atomic number such as tungsten. There is high voltage in the circuit, which connects the anode and cathode.

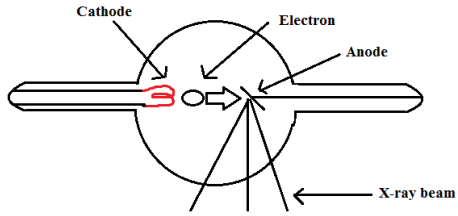

Figure 1.6: Illustration of the x-ray tube.

The voltage and heating of the cathode promotes release and acceleration of electrons from the cathode towards the anode. The speed of the electrons is proportional with the voltage. The electrons interact with the anode when they hit it. Two different interactions, the atomic processes of x-ray fluorescence and Bremsstrahlung, create the x-rays.
The x-rays produced are emitted from the anode and usually directed towards the object under investigation, i.e. an extremity with suspected breakage or the lungs. A proportion of the x-rays are absorbed by the tissue through photoelectric processes. The probability of these processes increases with the electron density of the tissue. This signifies that tissue with low atomic number, such as air, allows passage of a high proportion of rays. Tissue with a high atomic number such as bone only allows passage of low proportion of the x-rays. The ability to block the x-rays is also called the attenuation of the tissue.
An x-ray sensor is necessary to get a depiction of the attenuation of the tissue of investigation. A x-ray sensor, as a photographic film or scintillation detector, is placed underneath the object of investigation. Hereafter it is possible to get a two-dimensional depiction of the object, that the rays have been passing through.
On photographic films a proportion of the x-rays interact when hitting the film, and hereby colouring it. In a scintillation detector the interacting x-ray photon is converted into a visual photon, which can be detected by a photomultiplier delivering an electric signal. The resulting image signal will be inversely proportional to the electron density of the tissue, that the x-rays have passed through.
Collimators are placed between the x-ray sensor and the object to ensure, that the x-ray sensor does not detect scattering x-rays from the interaction between the object and the incident x-rays. An example of a x-ray image can be seen

Figure 1.7: An x-ray of the thorax acquired from Rigshospitalet.

in figure 1.7. The same technique is used in CT to extract electron density of the entire volume. The x-ray tube is rotated around the object while emitting x-rays in a fan shaped beam. An x-ray sensor is located at the other side of the rotation circle opposite the object. Figure 1.8 is photo of a CT scanner from Rigshospitalet. It is possible to make a tomographic, 3-dimensional, reconstruc-

Figure 1.8: CT-scanner at Rigshospitalet.

tion of the object from these projections, using methods like filtered backprojection (FBP)[46], algebraic reconstruction[7] or Ordered Subset Expectation Maximization (OSEM)[81]. The reconstruction depicts the mean attenuation of the object in discrete locations, the voxels of the scan. The attenuation is given on the Hounsfield scale, which spans from -1024 to 3071 Hounsfield units (HU), where 0 HU is the attenuation of water, -1000 HU is the attenuation of air, and

bone attenuation ranges between 400 and 2000 HU.
Modern CT-scanners use helical rotation of x-ray tube and sensor on a gantry to increase the speed of the image acquisition. The image quality from these scanners is dependent on the pitch of the scan, i.e. the length of the table travelled per rotation divided by the x-ray beam width. Increasing the pitch will decrease the quality of the images and decrease the amount ionizing radiation and scan time.
CT scanners produce images with high contrast between different tissues of different material content. They excel at the distinction between soft tissue, bone and air cavities. Organs are easy to locate and allows a reasonable distinction of tissue by adjusting the spectrum of the HU, that is visualised on the image. A good visualisation can be acquired by injecting contrast liquids into vessels prior to the scan. The acquisition time of the scan image is relatively short(minutes for a full body scan on modern scanners) making it possible for a fast visualization of the entire body.
But CT scans are also limited by their own technology. They can only visualize boundaries between tissues of different densities. This is especially problematic in volumes with soft tissue, where there is small or no differences in density.
Another issue with CT as an imaging modality is the ionising radiation dose delivered to the patient, which can range from 1-30 mSv in effective dose [97] [131], thus increasing the risk of inducing cancer.

1.2.2 Cone Beam Computerized Tomography (CBCT)

During the last decade a new form of clinical CT scanners has been introduced to radiotherapy, where the beam of the x-ray tube is cone shaped[84]. The cone beam computerized tomography (CBCT) scanner is usually part of an integrated scanner and delivery system, see figure 1.9. Having a scanner integrated with the delivery system does provide some advantages regarding setup of the patient, But the new geometry also poses some new reconstruction obstacles [46]. The images are usually characterized by inferior quality due to increased scatter and reduced contrast [17]. It is possible to increase image quality by increasing the number of sample angles, while increasing the dose to the patient. The dose distributed to the patient is lower than conventional CT [154].

1.2.3 Megavoltage Computerized Tomography (MVCT)

The patient can also be visualized by detecting the photons that passes though the body by using a linear accelerator. Acquiring projections at different angles around the patient provides the possibility for megavoltage computerized

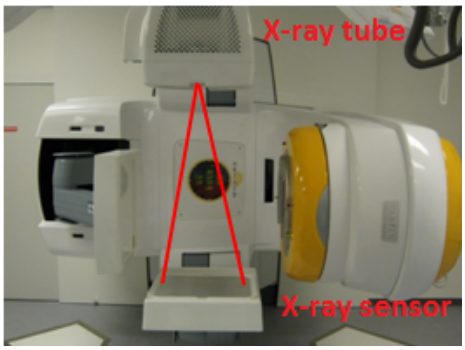

Figure 1.9: Integrated cone beam CT and medical linear accelerator at Rigshospitalet.

tomography (MVCT). These photons produced by a linear accelerator are of a higher energy than the conventional CT, typically 6 MeV compared with the normal level of about 30 KV in a conventional CT.
The image acquisition technique is similar to conventional CT or CBCT dependent on the delivery system. A conventional linear accelerator is placed on an arm, that is rotated around the patient, while helical tomotherapy deploys a linear accelerator on a ring gantry. The images from an MVCT image provide inferior tissue contrast compared to kilovoltage CT (KVCT) as it is seen in figure 1.10. But the attenuation coefficients in MVCT are more closely proportional to the attenuation coefficients of the treatment energy. Unfortunately the dose due to imaging using MVCT are higher than KVCT[154].

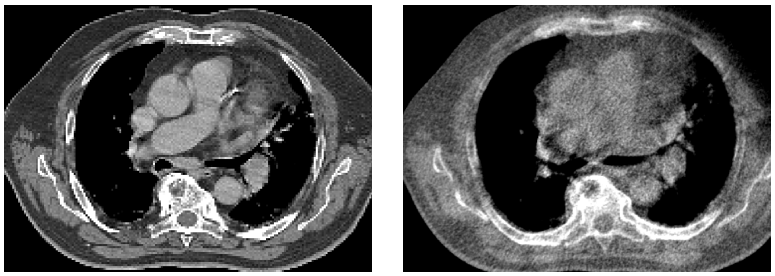

(a) (b)

Figure 1.10: Two images of the same patient acquired with conventional CT (a) and MVCT(b).

1.2.4 Positron Emission Tomography (PET)

The imaging modalities mentioned above all provide structural and anatomical information about the patient, but none of the conventional images from the other modalities provide functional information about the physiological processes in the tissue. One way of acquiring volumetric functional imaging is positron emission tomography.
In PET a radioisotope is injected into the patient. The radioisotope will usually be incorporated with a tracer molecule with biological properties building a tracer compound. Once injected into body, e.g. through the veins of the patient, the molecule with the radioisotope will distribute itself throughout the body. The distribution of the tracer will depend on the biological properties of the tracer. The different radioisotopes used in PET are discussed below.
The radioisotope undergoes positron emission decay at a given time and emits a positron. The positron travels a short distance, until it interacts with an electron. Since the two particles have opposite charges, they are both annihilated by the encounter. This annihilation produces a pair of gamma photons with opposite direction and energy of 511 keV, the energy equal to the mass of the positron or electron, the process is illustrated in figure 1.11. A ring of detectors

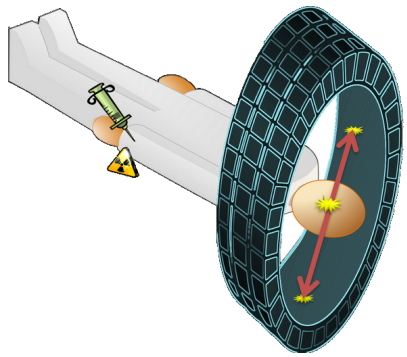

Figure 1.11: Illustration of a PET scan. The scan is performed after injection of the radioisotope. Upon annihilation of the positron and electron, two photons are emitted and detected by the ring of detectors[107].

are surrounding the patient in a PET scanner. The detectors of the ring resemble the scintillation detectors of the CT scanner. If two photons of 511 keV are registered at the same time in the detector ring, it is possible to infer a straight line of coincidence between the two blocks of the ring. It is assumed that the positron decay has taken place on that line of coincidence. Though false positives are possible, the knowledge about opposite direction and the energy of the photons provides a higher signal-to-noise ratio.

Table 1.1: Overview of the tracer compounds used in oncology [157] [26]

Tracer compound	Targeted process
F^{18}-fluorodeoxyglucose (FDG)	Glucose metabolism
C^{11}-methionine (MET)	Amino-acid transport and metabolism transport and metabolism
F^{18}-fluoride	Bone remodelling
C^{11}-Thymidine	DNA synthesis
F^{18}-fluormisonidazole (FMISO)	Hypoxia
O^{15}-water	Perfusion
F^{18}-fluorthymidine	DNA synthesis
F^{18}-fluorethylthyrosine	Amino-acid
C^{11}-choline	Choline metabolism
F^{18}-fluormethyltyrosine	Amino-acid transport
I^{124}-iodo-fluoro-deoxy-arabino-furanosyl-uracil (FIAU)	Herpes simplex thymidine kinase gene expression
CU^{60}-diacetyl-bis (N4-methylthiosemicarbazone) (CU-ATSM)	Hypoxia

The image can be reconstructed using FBP and OSEM, but the calculations are somewhat complex because of the decreased number of coincidences compared with CT. It is possible to improve the image quality by making

- Correction for random coincidences
- Estimating and compensating for scattered photons
- Compensating for detector dead-time
- Detector sensitivity correction
- Decay correction
- Attenuation correction based on CT acquired prior to the PET scan.

The functionality of PET depends on the radioisotope and the tracer molecule, that has been used. A number of different radioisotopes are used in PET imaging the most usual being C^{11}, N^{13}, O^{15} and F^{18}. Not all tracers can be combined with the different radioisotopes. A list of radioisotopes and tracer compounds and their targeted process can be seen in table 1.1. The most widely used tracer compound for PET imaging is by far FDG. FDG is applicable for oncology but also for functional analysis of brain, heart and lungs.
FDG is a glucose analogue, and it is taken up by most tumours because of their

increased cell proliferation, that increases their uptake of glucose to abnormal levels. Once inside the cell it stays there, because it cannot be metabolised like normal glucose.
The half-life of F^{18} of 110 min makes it an ideal radioisotope. It allows time for a half hour distribution after injection of the compound in the body before the actual scan. Normally a patient should have been fasting at least 6 hours before the injection to ensure low blood sugar. During the distribution time of the compound the patient should be physically inactive to reduce the signal of muscles.
A typical dose of FDG is 400 MBq. The FDG scan usually visualizes a tumour quite clearly, as it is seen in figure 1.12. As it is noticed from the figure, the voxels of PET are somewhat larger than the voxels of CT, which arises from the uncertainties of PET image acquisition arising from factors as positron travel length and detector block size. Since the amount of blood volume differs between

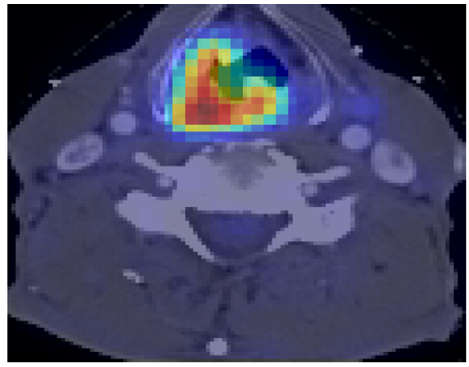

Figure 1.12: CT/PET image of a head and neck cancer patient with cancer at hypopharynx. The CT image is given in black and white while the PET image is superposed as color coding from 0 SUV in dark blue to 5 SUV in red. The tumor is lighted up on the PET image.

patients, and hereby changes the concentration of the compound in the blood from patient to patient. To get a quantitative signal, which can be compared between patients a standardized uptake value (SUV) has been introduced[18]. SUV is defined as,

$$SUV = \frac{Ac}{Dose/BW} \tag{1.1}$$

where Ac is the measured decay corrected activity in kBq/g, $Dose$ is the injected dose in MBq and BW is the body weight of the patient given in kg. As it can be seen SUV does not have any unit. As described before, SUV should make it possible to quantitatively compare image values.
Unfortunately SUV is prone to differences between patients due to 3 different factors[18]

- Biological factors as blood glucose level, uptake period, patient motion, patient comfort and inflammation
- Manual factors as lack of cross calibration between PET instruments, residual activity in injection syringe, incorrect synchronisation between instruments, use of injection time for decay correction and paravenous injection
- Technical factors as scan acquisition parameters, image reconstruction settings, region of interest definition and use of contrast agents in the CT for attenuation correction

To reduce the influence of these factors a strict protocol must be composed and complied for every scan as well as routines for calibration and quality assurance of both scanner and dose calibration instruments.
When introducing PET imaging or introducing SUV in a clinical setting Boellaard et al.[18] has provided excellent reviews describing both influencing factors and a protocol for standardised PET image acquisition and quantitative data analysis.

1.2.5 Magnetic Resonance Imaging (MRI)

Even though magnetic resonance imaging (MRI) is not used in any of the studies for this thesis it is still included because of its large importance and applicability. The theory behind image acquisition and generation of the signal as well as the vast amount of different acquisition types is outside the scope of this thesis. Here follows a brief description of the imaging mechanism and the anatomical pictures of MRI usually acquired for radiation oncology.
MRI uses a strong magnet to align the spin of specified nuclei type within the body of the patient. A constant magnetic field is applied along one direction. A magnetic pulse is then induced by the magnet and the following signal from the patient is measured by receiver coils. The signal arises due to the relaxation of the spin nuclei, which had just been aligned in the magnetic field and now is returning to the direction of the constant field. The sequence of magnetic pulses is repeated while measuring resulting radio frequency from the nuclei spin it is possible to get image values for the entire patient.
Applying magnetization across the entire body of the patient makes the interconnection between spin signal and its actual location in the patient a complex problem. This is solved by applying different field gradient phases and frequencies along the three axes of the patient.
The two signals, which are measured in conventional MRI, are T1 and T2. Both of these signals arise as the hydrogen nuclei are manipulated by the induced

magnet field. The T1 image reflects the time to reduce the difference between a longitudinal magnetization and the equilibrium magnetization, the so-called spin-lattice relaxation time or T1. The T2 image reflects the rotation of the nuclei spin in the transverse plane. A magnetization is applied in the transverse plane orthogonal to the equilibrium field. While the nuclei spin returns to the equilibrium state it will emit radio frequency signal in the transverse plane. The relaxation time of this spin-spin signal is the T2 signal.
The T1 and T2 images are dependent on the water concentration in the specific location of the body. As such the image quality of MRI is better to locate boundaries between soft tissues. As mentioned above MRI allows many different anatomical and functional imaging capabilities. Furthermore patients do not receive ionizing radiation, when scanned, opposed to the other imaging modalities of this section.
Unfortunately the MRI does not provide the same clear boundaries between bone and surrounding tissue. At the same time MRI does not provide attenuation coefficients for the tissue. This means that the MRI modality is not suitable for the attenuation necessary for PET and for radiotherapy planning. Practical solutions for these problems are emerging, and they can eventually be solved by segmenting the image into different tissue types and distribute attenuation coefficients according to tissue type.

1.3 Radiation therapy

Radiation therapy is a therapy strategy with increasing application for cancer patients. The radiation dose can be administered in two ways: from outside the body or inside the body. In the first case, called external beam radiotherapy, a linear accelerator gives a beam of radiation dose either consisting of photons or particles, as electron or protons. In the second case, called brachytherapy a radiation source is distributed close or inside the cancer volume. The advantages of radiation therapy compared with alternatives as surgery and chemotherapy lie in the absence of direct intervention/surgery and the ability to concentrate treatment at the tumour volume.
In this section of the thesis the mechanisms of radiation therapy is summarized. A description of the clinical workflow of radiation therapy is included with special emphasis on the contouring process. At the end of the section the treatment delivery and treatment adaption is briefly described.

1.3.1 Mechanism of Radiation Therapy

The principle behind radiation treatment is the capability of ionizing radiation to damage the DNA of cells. The damage either kills or causes the cells to reproduce more slowly. Ionizing radiation has a larger effect on cancer cells, since they reproduce more frequently. Cells in general are more vulnerable to ionizing radiation during cell division also called mitosis. Therefore the organs with high cell proliferation are also more vulnerable to ionizing radiation. Cancer cells also have reduced repairing mechanisms of the DNA. This means that damage to the DNA, which could be repaired in normal cells, can be lethal for cancer cells. The radiation dose can be spread over time, giving the dose in fractions with smaller doses. This allows normal tissue to repair between radiation dose fractions in a higher degree than the cancer cells.
In the history of radiation treatment there has been a ongoing controversy between hypofractionation, few treatment sessions with large dose, and hyperfractionation, more treatment sessions with lower dosis. On the practical side in clinical workflow the hypofractionation scheme poses benefits regarding patients, since fewer treatment sessions require less setup time for the patient. The patient also benefits from fewer sessions both regarding attendance at the clinic and psychological stress of treatment. Furthermore the progress in technology has increased the potential to direct the high dose of ionizing radiation to the tumour while sparing the surrounding tissue to some degree[100].
But regarding normal tissue complication hypofractionation has some demands to the course of treatment. The cells of the normal tissue, which receive ionizing radiation, must be allowed to repair between the treatment sessions [16].
Hyperfractionation is still the preferred strategy for some tumours. For head and neck cancer patients hypofractionation has so far not shown any benefit[34], regarding cure or after-effects of the treatment. This could be due to the concentration of critical organs in the head and neck volume[74]. Furthermore the normal tissue is not adequately spared or given enough time to repair itself under a hypofractionation strategy. But common to all treatment strategies, ionizing radiation always kills normal cells in the body. Consequently the success of the treatment and complication prevention depends on the capability to administer a sufficiently strong dose to the tumour while reducing dose to normal tissue to levels with the lowest risk of normal tissue complication. That makes the definition of tumour and tissue a vital step in the preparation of radiation therapy.
Radiation treatment can also be given with palliative intent, where the intention is not cure. This form of treatment seeks to relieve symptoms and suffering of cancer for the patient. This is usually done to shrink tumours close to organs such as the brain, spine or esophagus.

1.3.2 Clinical Workflow

The clinical workflow varies from clinic to clinic. Some of the differences are due to the technical capabilities of the clinic, i.e. not having imaging modalities as MR and PET to guide treatment planning. Other clinics do not own advanced delivery equipment, and hence they are not using them. Preparation, planning, execution and quality assurance also varies among clinics, and a description of the variation between clinical settings is out of the scope of this thesis.
In the following sections a general description of the clinical workflow at Rigshospitalet for radiation therapy is given. The description is based upon the practical experiences and knowledge of the author.

1.3.2.1 Clinical Diagnosis and Examination

The initial diagnosis or suspicion of cancer is usually conceived at the primary medical caretaker of the patient. The patient usually arrives at the caretaker with a suspicion based on general symptoms in the body such as pain. Localized growth or the discovering of "lumps" in parts of body such as breast or skin can also be the first sign of cancer.
The primary medical caretaker, which is usually the general practitioner of the patient, will examine the patient and then refer the patient to an oncology department.
In head and neck cancer the suspicion can also arise at the dentistry upon examination of the teeth and oral cavity. The patient is usually referred to an ear-nose and throat specialist, who will refer the patient to an oncology department upon positive findings.
Upon arrival to the oncology department the patient will be given a clinical examination. A systematic examination of the patient function and symptoms will be performed both by manual examination and questioning of the patient. With head and neck cancer suspicion the oral cavity is examined as far down as the larynx as well as the outside of the neck and nose cavity. In figure 1.13 an example of the usual depiction sheets can be seen, which are used to visualize the location of the suspected cancer, which have been found at the examination of the patient.

1.3.2.2 Imaging and Staging

The patient is hereafter referred to the imaging modalities, which are relevant for the patient. For all patients with suspected cancer a CT scan is a minimum. PET is also taken for certain patient groups, where it has been proved [48] or

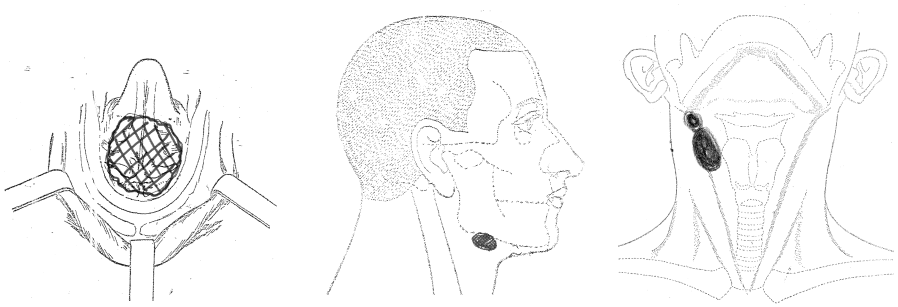

(a) (b) (c)

Figure 1.13: Depiction sheet for tumour location in three different patients from Rigshospitalet. Left picture pharynx and the oral cavity is seen, center picture the head from the right and right picture the neck seen from below the head.

supposed beneficial as with head and neck cancer at Rigshospitalet. An MRI scan is usually carried out with volumes of soft tissue involved as in brain or cervical cancer. All scans in preparation for radiotherapy should be performed on a flatbed, so that the scan situation resembles the treatment situation as much as possible. In the same way the patient should wear any immobilization equipment during the scans.
Based on the images and the clinical examination the patient is then staged and assigned for a treatment. The referred treatment depends on the cancer site and spread. Localised tumors with no suspected spread, which are easily accessible, should be removed by surgery if possible followed by chemotherapy to handle any risk of microscopic invasion.
Radiation treatment combined with chemotherapy is the conventional treatment for head and neck cancer with lymph node involvement. Any patients with metastasis should not go through radiation treatment with the intent of a cure.

1.3.2.3 Treatment Planning

The following section gives a general summary of the elements associated with the definition of volumes of interest (VOI). The volumes described below is sketched in figure 1.14. The patient is usually scanned with the techniques available and suitable for the suspected disease volume. The tumour volumes and normal tissue is defined on the CT-scan. It is elected for radiation therapy planning because of its inherent properties:

- It visualizes the volume of the body

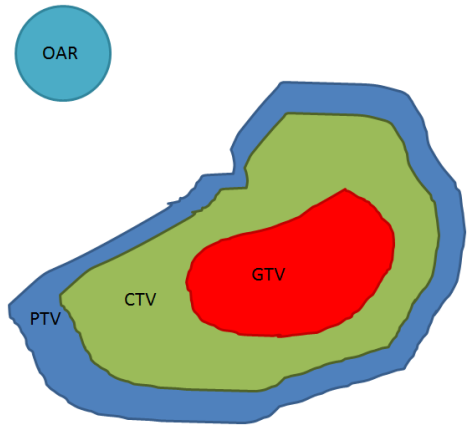

Figure 1.14: Presentation of the different volumes of interest (VOI). Gross tumour volume (GTV), clinical target volume (CTV), planning target volume (PTV) and organ at risk (OAR).

- The edges between soft and hard tissue are clearly visualised (e.g. between muscle and bone)

- It provides the linear attenuation coefficient in the visualized tissue. This enables a computation of the distributed radiation dose in the body.

The VOI are outlined by a radiation oncologist or a radiologist, hereafter denoted the contourer.

1.3.2.4 Gross Tumour Volume (GTV)

The GTV includes the gross demonstrable extent and location of the tumour[83]. The contour is defined on two dimensional slices by the contourer.
The GTV is contoured on the basis of all imaging modalities available and the results of the clinical examination of the patient. The GTV comprises the volume of the primary tumour along with any metastatic regional nodes and distant metastasis, which can be differentiated by the system, and naming the volumes accordingly.

1.3.2.5 Clinical target volume (CTV)

The clinical target volume (CTV) is defined after the GTV. The CTV includes the GTV and tissue, that contains "a subclinical malignant disease with a certain probability of occurrence relevant for therapy"[83]. The volume should include all areas with suspected microscopic disease. It is contoured on the basis of the probability of pathologic lymph node involvement [62]. Like the GTV it can be differentiated into volumes of different risk. The delineation of CTV is, like the delineation of GTV, based on the individual and collective clinical experience, making it vulnerable to variation.
Among some radiation oncologist there is a belief that the CTV should include a subjective margin to compensate for contour variation. If it was possible to subjectively assess the possible variation subjectively the contourer should just automatically include the tissue in question as suspected tumor.

1.3.2.6 Planning target volume (PTV)

The administration of the radiation dose is the subject of variation due to geometrical errors. They are generally divided into preparation and execution errors. The nomenclature of error is a broad definition, which also includes uncertainties and variation. The errors, which occur in the preparation process, become systematic errors. They originate from:

- Imaging, including errors caused by imaging modality and difference between imaging setup and treatment setup
- Image fusion, when using multiple modalities
- VOI delineation

Sources of errors in the execution phase are:

- Patient setup error
- Movement during and/or between treatment sessions

It is essential to avoid and minimize the influence of any errors, but there is a difference in between the consequences of systematic and random errors, which arise from preparation and execution errors respectively. Systematic errors causes geometrical miss of the intended target. This applies for all or, in the

case of inter-fraction system errors, for all remaining treatment fractions. As the name indicates, random errors cause geometrical miss of a random volume. It is possible to take precautionary measures against the errors by including a margin on the target volume[147]. This implies, that the magnitude of the error is known or estimated. The planning target volume (PTV) is the concept of this assumption.
The PTV was introduced to ensure that the CTV absorbs the prescribed dose. The concept was introduced in ICRU Report 50[82] but without any recommendations for magnitude of the margins that should be applied. Bel et al.[13] introduced the first method for margin estimation on the basis of a quantification of the translations. During the next 6 years, 6 other studies were published with recommendation for margins around the CTV [8][98][111][138][146][148]. At the same time recommendation for the PRV margins was published [44][43] [99][149]. These margins are implemented to account for execution and some preparation errors. The most widely accepted margin definition is given by van Herk et al [148] as :

$$m_{PTV} = \alpha \cdot \Sigma + \beta \cdot \sigma - \beta \cdot \sigma_p \tag{1.2}$$

where α is derived from a chi-square distribution which is dependent on the desired dose confidence level (in percent of patients) and the dimension of the systematic errors, Σ is the standard deviation of the systematic error, β is derived from a one-side cumulative normal distribution which is dependent on the desired CTV dose level (as percentage of the prescribed dose), σ is the execution errors magnitude and σ_p is the standard deviation describing the effect of the penumbra of the delivery beam.
It was not until 2012 that the impact of CTV shape variation was estimated[104]. In the study the shape variation of CTV but only to account for difference due to repeated delineation. The author recommends an increase of α from 2.5 to 3.2 to assure 95 % of the prescribed dose to 90 % of the patients.
An uniform dose level is then prescribed to the PTV. In head and neck it is usually 66 Gy. Since the delivery techniques of the clinical practice seldom provide a uniform dose over the entire PTV, it is generally reported using a dose volume histogram (DVH). The DVH describes the minimal cumulative dosage, that the VOI have received An example can be seen in figure 1.15. The PTV can be divided into different subvolumes like the GTV and the CTV, which are prescribed a dose reflecting the proximity of an organ at risk (OAR) or knowledge about the tumour, that justify a decreased dosage, while retaining the same tumour control probability (TCP). TCP is defined as the probability of cure, given a certain treatment[165]. Cure is here defined as the long-term recurrence-free survival of the patient. TCP increases with increasing dosage level and coverage[39], and is governed by tumour type and cell density.

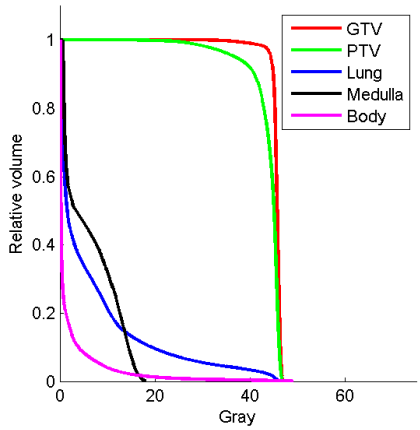

Figure 1.15: Example of a dose volume histogram (DVH) for a lung cancer patient. It is seen the gross tumour volume (GTV) and planning target volume (PTV) receives a high uniform dose. The prescribed dose for stereotactic body radiation therapy (SBRT) is 45 Gy. The normal tissue has a lower and heterogenous dose as it can be seen in the lower left of the figure.

1.3.2.7 Organs at risk

The ambition of radiation therapy is the highest degree of TCP. This can be achieved by increasing margins and prescribed dosage. But that comes with a price for the surrounding normal tissue. The normal tissue complication probability (NTCP) describes the probability of normal tissue complication due to radiation dose [24] . NTCP behaves like the TCP, but varies between tissue types due to the difference in cell types, reflecting cell division rate among other things, and tissue organisation, parallel and/or serial[159].
Delineation of OAR is therefore vital for the treatment success, defined as both cure and lowest impact on vital body function due to the radiation treatment. In clinical practice this does not mean a delineation of all organs in the body, but rather a delineation of the organs, that have vital function. This is again influenced by the therapy. Adding an uncertainty margin allows the contourer to delineate the planning organ-at-risk volume (PRV), which represents the theoretical location of the organ - due to errors. Dosage given to the OAR is represented in the DVH as with the PTV. In head and neck cancer the OAR will typically be the salivary glands, the spinal cord and the optic nerve. An example of some of the VOIs can be seen in figure 1.16.

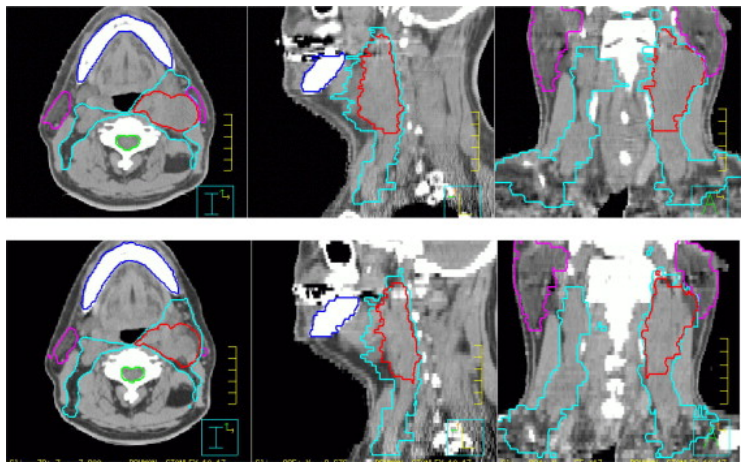

Figure 1.16: VOIs for head and neck cancer in a head and neck cancer patient. In red the gross tumour volume, magenta the parotid gland, blue the mandible, cyan nodes and in green the spine.

1.3.2.8 Defining the planning objectives

After the all VOI has been identified the rest of the treatment planning is executed mainly by a medical physicist or dosimetrist working closely with a radiation oncologist. Defining the planning objectives is an important step of the treatment planning. The objectives should increase the TCP as much as possible while decreasing the NTCP.
To reduce the dimensions of the outcome criteria, the objectives for the VOI are generally given in terms of the DVH. The objective for the PTV is usually set to a uniform dose at the prescribed level. For the OAR, as described above, the levels differ. The objectives for a serial organ with vital function, such as the spinal cord, are set to dosage below a critical dose level, because organ function can be influenced with radiation damage to a single subunit of the organ. The objectives for a parallel organ, such as the parotid gland, should be set as low as possible. But they could allow a high dose levels, given to part of the volume, so that the function of the organ can be maintained, even though subunits are damaged by the received radiation.
The objectives of PTV and OAR are also weighted according to the success criteria of the treatment. Delivering the prescribed dose to the PTV should have a higher significance than lowering dose to an organ, like the parotid gland. This is due to risk recurrence of tumour if not treated adequately, while a decreased salivary function of the parotid gland is not necessarily lethal.
The delivery plan are usually given as the amount of dose, that a proportion of

an organ should receive or not receive, e.g. all of the PTV must receive at least 95 % of the prescribed dose, or half of PRV should not receive more than 30 % of the prescribed dose.

1.3.2.9 Optimising the treatment plan

The treatment plan is then optimised. Given the weights and the objectives it is possible to define an objective function, which depends on the dose given to PTV and PRV. The dose plan is calculated as a result of the delivery parameters. Delivery parameters depend on the delivery technique. The parameter settings, e.g. number of beams, beam direction, collimator settings, beam strength. The dose distribution is calculated using these parameters in a treatment-planning system.
Calculating the dose distribution can be done on several complexity levels ranging from pencil based to Monte Carlo methods[133]. Since the objective can be non-convex, the resulting optimised parameters are dependent on the initial parameter settings and potential locked settings.

1.3.2.10 Evaluation of the treatment plan

The plan is then finally evaluated in the third iteration step. It is evaluated, whether the treatment plan meets the initial objectives to an acceptable level. The need for additional VOI (due to the resulting treatment plan) is assessed, and it is evaluated, whether the objectives should be constrained or relaxed to have a suitable treatment plan. It is also assessed, whether the optimised parameters are a result of a local minimum in the objective function based on the initial settings of delivery parameter.
In the clinical setting this is usually done subjectively on the basis of experience with the optimisation software and data on NTCP and TCP. The planning objectives are then redefined, and the treatment plan is reoptimized, until it satisfies the clinical demands.

1.3.2.11 Treatment delivery

There are many different methods for delivering radiation therapy. This section describes intensity modulated radiation therapy (IMRT). In IMRT ionizing radiation is delivered with high precision using multi-leaf collimators and using radiation beams from several angles. A quality assurance of the treatment plan must be made prior to any treatment delivery. The dose plan must be controlled

with a phantom. First the dose plan is recalculated for the phantom geometry. The plan is then delivered to the phantom while measuring the given dose at several locations in the phantom, see figure 1.17. If the measured dose varies from the prescribed dose the dose plan must be rechecked and eventually optimized again. If the measures and prescribed dose continues to vary the delivery system must be checked for errors. The treatment can be delivered to the pa-

Figure 1.17: The phantom for the quality assurance of tomotherapy. The two cables going into the phantom are for the ion chambers that measure the delivered dose. Picture taken at the University of Wisconsin, Madison, Department of Human Oncology

tient using a medical linear accelerator(linac), see figure 1.18. The linac delivers a photon beam in a manner, that resembles the x-ray tube. The electron is produced by an electron gun. After this it is accelerated using an accelerating waveguide. The accelerated electron is directed by a bending magnet to the photon source. The impact of the electron on the photon source produces photons, which are stopped, unless they pass toward the patient through a primary collimator. Hereafter the beam gets a uniform strength by using a flattening filter. In the end the photon beam is modulated using a secondary collimator, called a multi leaf collimator. The linac can also deliver an electron beam by removing the photon source. The gantry of the linac rotates around the patient delivering the beam from different angles. To reduce errors in the delivery of the treatment the patient is placed in the same position at every treatment session. In head and neck cancer the patient is immobilized using an immobilization mask possibly a biting block. Patient position relative to the delivery system is also ensured using lasers on the scanner and in the treatment room. For tumors which moves due to breathing it is also necessary to ensure breathing control which ensures that treatment is delivered during the same timing of the breathing phase.

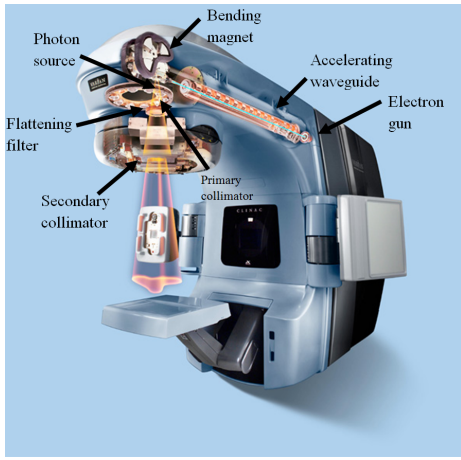

Figure 1.18: Medical linear accelerator and an overview of the components[151].

1.3.2.12 Treatment Adaption

The shape, size and location of the tumor can change during treatment in response to the received dose. The tumor can shrink because of cell death and immune response due to the ionizing radiation. At the same time the surrounding tissue also changes due to the treatment. Cancer patients also generally loose weight during the course of the treatment. It is necessary to adapt to these changes to ensure tumor coverage and minimize NTCP.
Therefore imaging capabilities have been introduced to the delivery room. These can produce either CBCT or MVCT images. These images are used primarily to check the position of the tumour and surrounding tissue. If the tumor appearance or position shift dramatically during treatment, it will be necessary to replan the patient. This includes new contours of the patient on the new images and reoptimizing the dose plan for the new situation.

1.4 Manual Contours

In this section we will touch upon the subject of manual contours. Firstly some results in the literature for intra- and inter-operator variation is presented for the head and neck cancer whereafter the standards for tumour evaluation is described.

1.4.1 Contour Variation

The variation for manual contours can be divided into inter- and intra-operator variation. Inter-operator variation is the variation between different contourers delineating the same VOI, i.e. doctor A, B C, and so on delineating a GTV. The difference between contourers arises from the different education and experience of the different contourers. The inter-operator variation can be seen as a systemic variation.
Intra-operator variation is the difference between delineations by the same contourer, i.e. doctor A delineating a GTV at time t_1, t_2, t_3, and so on. The intra-operator variation is to some degree a random error unless the contourer is provided additional information.
In head and neck cancer, Breen et al.[22] estimated the inter-operator variation to 2.21 cm^3 and intra-operator variation was estimated to 2.04 cm^3 for GTV contours on CT. There are other studies of variation for contours, [101] [122][79][85][27], but it is generally difficult or impossible to compare the variation of these studies since they report different metrics of variation. Furthermore the available imaging modalities vary as well as the number of patients and contourers. Chao et al.[27] showed that the inter-operator variation decreases when the contourers are given a preliminary contour.

1.4.2 Evaluation of contours

The evaluation of contours is a challenge in relation to GTV. In opposition to normal tissue, which has visible boundaries to some degree, tumour is characterized by microscopic infiltration of bordering tissue. These infiltrations are impossible to detect on any image modality[35]. This leaves only two methods for evaluation of the contours: specimen or board of experts.

1.4.2.1 Specimen

The gold standard of contour evaluation is the comparison with a surgical specimen. This means that the patient get the appropriate image scans and then the tumour is surgically removed along with certain degree of the surrounding tissue [35]. After surgery the specimen is placed in a container and frozen down for a couple of days. Hereafter the specimen is cut into slices in the same plane as the images. A pathologist evaluates the slices hereafter for gross tumour infiltration. In the end the slices are coregistered to the image plane of the imaging modalities. The process is complex and requires consistent preparation and implementation.

This procedure requires severe ethical consideration to the patient certifying that the patient is receiving the optimal treatment for his or her specific disease. If surgical removal is not the conventional treatment at the clinic it is highly unadvisable. Furthermore all steps of the procedure must be prepared and any error risk must be eliminated or decreased as much as possible. Any error throughout the procedure will be systematically increased with every following step.

1.4.2.2 Board of Experts

It is also possible to use manual segmentations to evaluate the quality of a GTV contour. If the evaluation is just done between contours made by different contourer we only acquire inter-operator variation as mentioned above. Another strategy is to let a board of experts make the evaluation contour together. But some assumptions are taken when using a board of experts as evaluation of contours.

- The combined experience will decrease their risk of disregarding parts of the tumour or including normal tissue in the GTV
- The board of experts are less prone to the intra-operator variation.

To this authors knowledge there is no studies which can confirm either of these assumptions. Taking the board of experts does not necessarily improve the evaluation of a contour but it should provide some sort of quantitative manner of evaluating contours by a single contourer.

1.4.3 Comparison measures

Several comparison methods exist for the evaluation of contours[67]. The simplest way of comparing contour of two volumes is the estimation of the simple volume. The simple volume can be assessed by simply adding the combined area of the contour on all slices and multiplying with its slice thickness. The simple volume of a contour can also be extracted estimating a three-dimensional shape of the contours and then estimating the simple volume of this shape. No matter how the simple volume is extracted it does not pose a good comparison measure. It is possible to acquire the extract the same estimation of the simple volume for two different contours which have different shapes or locations.
Another way of method of comparing volumes is the centre of mass. Comparing

the centre of mass is also a very poor comparison measure since it is possible for two contours with the same centre of mass to have no overlap. Illustration of the problem with this measure is illustrated in figure 1.19.

The overlap measures typically reported in radiation therapy are Jacard Index

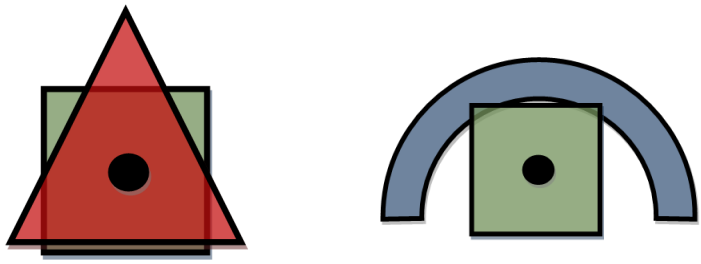

Figure 1.19: Problems regarding comparison measures. Both pairs of contours have the same centre of mass marked by the black mark. All three shapes have the same area.

and Dice coefficient

$$Jacard(A,B) = \frac{|A \bigcap B|}{|A \bigcup B|} Dice(A,B) = \frac{2|A \bigcap B|}{|A| + |B|} \tag{1.3}$$

wher $|A|$ is the simple volume of contour and $|A \bigcap B|$ is the simple volume of the overlap of A and B, see figure 1.20. For both of these measures a total overlap renders the same result and no overlap renders 0. The difference between these measures is the mathematical term used to divide the volume of the overlap, where Jacard index uses the volume that encompasses both volumes and Dice coefficient uses the mean of the volume. These measures have a problem regarding the clinical significance of them. Another method of assessing comparing

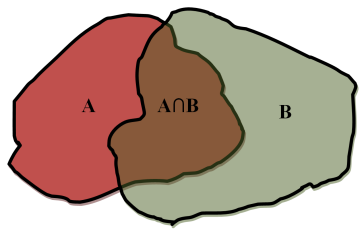

Figure 1.20: Illustration of the overlap situation overlap.

two volumes is mismatch and disconcordance index

$$Mismatch(A,B) = A - \frac{|A \bigcap B|}{|B|} Disconcordance(A,B) = 1 - \frac{|A \bigcap B|}{|A|} \quad (1.4)$$

The advantage of these mismatch is its correlation with the difference in the final dose plan[78].

1.5 Segmentation of Normal Tissue

Normal tissue segmentation is important to decrease NTCP. The following section describes the general approach of normal tissue segmentation, with a primary emphasis on registration, followed by a short description of the contribution to the field.
Segmentation of normal tissue is a general segmentation problem, where the definition of a VOI inside an object is requested. Using the normal characteristics of the VOI it is possible to define the outer contour of itself. These characteristics are usually the boundary of the organ tissue, similar intensity values inside the organ, known location and shape variations.
In radiotherapy for HN cancer correspondence is computed between images with a given VOI and the object without VOI delineation, the so-called atlas approach. The problem has two general approaches:

- Atlas based, where correspondence is found between objects with known definition of the VOI and the object without definition of the VOI
- Model based, where a model of the VOI requested is constructed from data

Both approaches assume has two presumptions:

- Data is available, which describes the object and/or VOI
- That the VOI and object has a level of variation which is possible to define

For automatic segmentation of normal tissue in radiotherapy the data consists of CT or MR scans of previous patients with manual delineations of the normal tissue. These are usually based on the former experience of the contourer and anatomical knowledge of the human body.

1.5.1 Atlas Segmentation

In atlas based segmentation the correspondence is defined between two objects, one with defined VOI, the template, and one without, the reference, using registration[124]. The desired result is the obtainment of the geometrical transformation, which gives point correspondence from every point on the reference to the template. The registration transformation is obtained by performing the following minimization.

$$\min_{T} \left(\int_{x} D\left(I_R\left(x\right), I_T\left(x+\tilde{x}\right)\right) + R\left(\tilde{x}\right) dx \right) \tag{1.5}$$

where D is a dissimilarity measure, I_R is the reference image, I_T is the template image, $\tilde{x}$ is the geometrical transformation and R is a regularizer of the transformation. The geometrical transformation is optimised using a optimization algorithm [12] until convergence or another preset criterion. The process is depicted in figure 1.21.

1.5.1.1 Dissimilarity

The dissimilarity measure forces the registration towards a transformation with the most similarity. The dissimilarity measure increases with increasing image dissimilarity. Minimal value of dissimilarity should imply that the transformed image is identical or absolute similarity. The typical measures of dissimilarity are:

- Sum of squared difference (SSD)
- Correlation coefficient (CC)
- Normalized mutual information (NMI)

In medical registration SSD is a basic way of finding correspondence when using the same image modality on similar objects, e.g. patients scanned with the same scanner. CC can be applied for images coming from different scanners using the same or similar imaging modality which will produce correlated intensity values at corresponding locations, e.g. CT-scanners with different energies. NMI is a an advanced and computationally heavier dissimilarity measure which can be used to perform registration across image modalities[118].

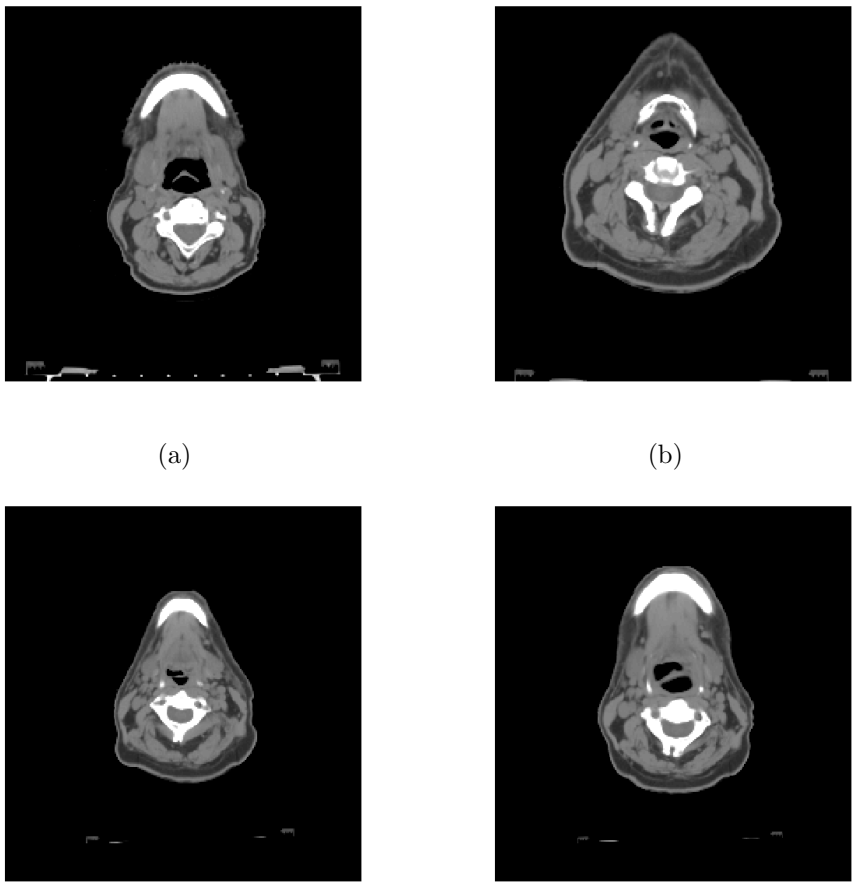

(a) (b)

(c) (d)

Figure 1.21: Depiction of the registration process from one patient to another. (a) is the reference and (b) is the template image. (c) is the affine transformed template image and (d) is the template image after non-rigid transformation. Registration is performed in 3 dimensions. Point correspondence is not necessarily present between (a) and (b).

1.5.1.2 Geometrical transformation

Geometrical transformation gives the displacement, $\tilde{x}$, of a point x between two images. Geometrical transformations are typically divided into linear transfor-

mations and non-linear transformations. The linear transformations are characterized by simple linear functions with few parameters with a low level of sophistication. Non-linear transformations, also called deformable or non-rigid, are a group of transformations which can perform non-linear transformation with a higher level of sophistication.

1.5.1.3 Linear transformations

The linear transformations are

- Rigid
- Similarity
- Affine

Rigid transformation is a relatively simple transformation, which allows rotation and translation, i.e. 3 rotation and 3 translation parameters in 3 dimensions. A similarity transformation allows scaling, contraction or expansion, between the two objects and therefore includes yet another parameter which scales the transformation, i.e. allowing registration between large and small objects with similar appearance. Affine transformations, in this nomenclature, allows shearing and hereby adds another 5 parameters compared to the similarity transform[135].

1.5.1.4 Non-linear transformation

All the linear transformations described maintain linear correspondence, as straightness of lines. Since correspondence between similar locations on images of different subject, or even the same subject at different time, are not necessarily linear, a non-linear geometrical transformation can be used instead. The non-linear transformations can offer an increase in the degrees of freedom. Registration using non-linear transformation functions is usually denominated non-rigid registration.
The non-linear transformation is parameterised using a given mathematical function, usually called basis functions. Among the basis functions used are fourier series [6], thin plate splines[59], b-splines[91], piecewise linear splines[49], multiquadrics [127] or Gaussian [9]. The function used in a specific image registration application is usually chosen because of their solvability, efficiency, differentiability and locality influence.

It is also possible to make a non-linear transformation which is non-parametric. The most popular implementation is an analogy to Maxwell's demon. A demon is placed inside each pixel or voxel of the template image which is attracted to similar voxels in the reference image[143]. To some degree the difference between the parametric and non-parametric methods lie more in the degree of discretization and the number of points which are evaluated.

1.5.1.5 Regularizer

The non-linear transformations allow registration of increased flexibility. But this increased flexibility may also allow inconsistencies in the transformation arising from folding of the transformation. Folding due to the transformation is usually indicated by negative Jacobian determinant of the transformation,$|\nabla T|$. Negative Jacobian determinants arise when the transformation collapses part of the image.
If the registration represents a change for a subject, the transformation should also be bounded by the possible physical restrictions. When making registration between subjects it is also desired to achieve a transformation with the same structures to a certain degree.
The regularizer is included to restrict the transformation to be reasonable. The regularizer should penalise transformation inconsistencies. A simple implementation is a quadratic penalty on the displacements. Further more advanced and complex regularizers are elastic [11], fluid [23] and diffusion[80]. It is possible to vary the regularizer for different materials reflecting the different physical attributes of the visualised material[126].
Consistency of the achieved transformation can also be achieved by reducing invertibility errors. These errors can be minimized by ensuring that it is possible to perform a transformation a consistent transformation both ways between template and reference. This is achieved by including another constraint on the optimization [30]. Since an atlas can be built from the collection compilation of several patient atlases a transitivity error can be taken into account by including a transivity constraint[31].

1.5.1.6 Segmentation Strategies

A single transformation between reference and template can produce a segmentation of the desired VOI[89]. But normally the variation of all possible patients is not represented in one atlas. Therefore an average atlas is constructed[32] which is then used as template. There exist several procedures to combine the different segmentations. A simple approach is voting, where the segmentation

is the volume segmented by a certain proportion of the transformed atlases. It is also possible to weight the atlas according to its similarity with the reference using a measure like the measure of dissimilarity defined above [125]. The simultaneous truth and performance level estimation (STAPLE) [155] computes a probabilistic estimate of an assumed true segmentation on the basis of maximum-likelihood estimation using an expectation-maximization algorithm.

1.5.2 Model Segmentation

Model segmentation builds on the assumption that a training data set is available. As opposed to atlas segmentation there is no assumption of correspondence between the individual VOI in the training set and the VOI. Instead it is assumed that the model contains the possible variation of the VOI.
One approach for model based segmentation is the active shape models (ASM) and active appearance models(AAM)[73]. The distinction between these two approaches is the difference between modelling the contour only, ASM, and the entire appearance of the object, AAM. The general approach to model segmentation consists of the following steps:

- Alignment of delineations putting them into the same frame of reference, e.g. using Procrustes alignment [60] [56]
- Finding point correspondence between the two shapes or volumes [139]
- Dimensionality reduction of the delineation, reducing the number of parameters necessary to represent the variation of the delineations, e.g. using principal component analysis [38]
- Finding point of correspondence between the model volume/mesh and the new VOI by minimizing a measure of dissimilarity by model parameters optimization.

The model segmentation is generally chosen if the objective is not only a contour of the VOI but also information about the VOI. These information can be extracted from the model parameters. Where atlas segmentation provides the correspondence between the whole object and provides every VOI in the atlas, model segmentation usually focuses on a single VOI.
The two approaches employ the same mathematical tools and are sometimes closely related. It is also possible to construct hybrids using elements from both approaches. Since contours are the general requisite for radiotherapy the methods employed here have generally been atlas segmentation.

Table 1.2: Result of the literature review for normal tissue segmentation

OAR	Atlas	Model	Hybrid
Mandible	[64] [167] [168]	[10] [88]	[66] [57] [120]
Thyroid	[28]		[66]
Parotid	[27] [65] [76] [121] [167] [161]		[66] [55] [58] [120]
Submandibular			[66] [120]
Brain stem	[27] [64] [167]	[10] [88]	[66] [58] [120]
Spinal cord	[27] [167]		[66]
Masseter			[66]
Nodal	[33] [142] [167] [119]	[29]	[66] [120]

1.5.3 State-of-the art

The volumes which have been segmented automatically in head-and-neck cancer patients are generally the OAR for radiotherapy. These volumes with their respective relevance and complications in case of radiation are:

- Mandible: Bone destruction
- Parotid and submandibular (spit) glands: Digestion and teeth dysfunctions as well as xerostomia.
- Thyroid gland: Hormone dysfunction
- Brain stem: Cognitive problems
- Spinal cord: Perception or movement dysfunction
- Masseter and pterygoid (jaw) muscles: Digestion and talking dysfunction
- Node regions: Immune system and possible tumour involvement

A literature review of normal tissue segmentation for head neck cancer using the Population-Intervention Comparison Outcome (PICO)-approach was performed $1/5 - 2010$ and again $1/7 - 2012$. The review returned the following studies categorised according to OAR and approach in table 1.2.

It is quite difficult to compare most the methods in the table above. [64], [168], [10], [88] and [57] were all part of the same workshop MICCAI clinical challenge to automatically segment the mandible and the brainstem. The goal of the challenge is to quantatively evaluate segmentation algorithms on the same data set. Han et al.[64] segmented both of the organs better than the other groups. The approach separated itself from the other proposed methods by using STAPLE

[155] to fuse the transformed atlases. The dense mutual-information deformable registration between the atlas image and the new patient was accelerated compared to the other methods using the computational efficiency of the graphical processing unit. The mandible segmentation was refined using a deformable surface model. Even though the method excelled all the other proposed methods it did not fulfil the clinical target of the challenge.
In the following workshop challenge the parotid gland was the target for segmentation. [65], [76], [121], [161], [55] and [58] participated in this challenge. Han et al.citeHan2010 performed better than the other proposed methods. The method was similar to [64] except that a deformable model was used to refine the surface of the parotid gland. Chen et al. [28] performed an evaluation of the strategy for atlas combination. None of the approaches performed significantly better than all the other approaches. Using the weighted correlation coefficient between the images as a weight for the combination of atlases gave the best result for both overlap and distance to the manual contour.

1.6 Segmentation of Gross Tumor Volume

This part of the thesis deals with autosegmentation of the gross tumour volume for head and neck cancer. Segmentation is a large field within image analysis. The emphasis of the first section lies on the state-of-the-art implementations which have been developed for the head-and-neck volume. The systems for evaluation of segmentation algorithms are then described. In the end the contribution is introduced.

1.6.1 State-of-the-Art

The segmentation methods for GTV in HNC patients are generally developed for PET/CT images. The methods can generally be divided into the following groups:

- Thresholding
- Background ratio
- Feature based
- Markov Random Fields
- Deformable model

1.6.1.1 Thresholding

Thresholding methods use a fixed level PET-signal for segmentation which determine the segmentation[129]. All voxels with a value above the fixed PET-level is segmented. The method can be implemented automatically using a preset fixed level, either retrieved from phantom experiments or clinical experience. The method can also be implemented semi-automatically where a user defines the threshold level based on the patient.
Thresholding methods are the simplest methods to automatically determine the GTV and are the least computationally expensive methods. It is sensitive to partial volume effect. Partial volume effect is the perceived decrease in activity due to volumes sizes and resolution of the imaging modality. There is severeal thresholding levels implemented in published studies but no rational approach to determine the fixed level for threshold exists.

1.6.1.2 Background ratio

The background ratio methods considers the background signal inside the bode of the PET-image and the actual tumour volume[36]. The methods are all based on a phantom experiment with a water-filled cavity with spherical containers of different volumes. The spherical containers are filled with a radioactive activity in the range of clinical signal-to-background range. The optimal threshold or background ratio is calculated on the basis of the signal to background ratio between the spherical containers of different volumes. The problem with the phantom experiments is that they do not represent the actual GTV situation. The tracer does seldom distribute uniformly over the GTV. The method might miss microscopic infiltration which needs to be treated.

1.6.1.3 Feature based

Feature based methods computes texture features from the available image scans[164]. A texture feature is a numerical appearance representation or description which describes a neighbourhood of voxels. The features can be divided into order dependent on their dimensionality:

- First order features are simple measures like mean, variance or kurtosis. First order features lacks any ordering information.
- Second order features represent the connection between the voxels in the neighbourhood. A matrix is constructed which represent the connection

between all the voxels in the neighbourhood. These matrices are called gray level coocurrence, gray level difference and gray level sum[69]. The features are computed by performing statistics on the matrices.

- Higher order features can be calculated by constructing gray level run length matrices[141], neighbouring level dependence matrices[140], neighbourhood level matrices[5]. The features are also computed by performing statistics on the matrices. Fourier features can also be extracted locally as features of the image. There exist an abundant amount of feature types which can be used to extract descriptors of the image volume.

Having a feature or descriptor does not deliver an automatic segmentation. A classification must be derived which distinguishes between tumour and tissue specific voxels. This is usually performed using machine learning. In machine learning for classification you typically have a training data set with known labels. In our instance the labels would be either tumour or another non-tumour label.
The machine learning algorithm then derives a classifier based on the given training set which determines which voxels are segmented as tumour and tissue. Feature based segmentation is never better than the training set from which it is built.
Using machine learning on features that have no anatomical or functional meaning can make it hard to comprehend the resulting classification. Furthermore if the initial training set does not adequately represent the system or the classification of it is uncertain you risk magnifying the uncertainty of your segmentation. Features in medical images vary with scanner and reconstruction setting[51]. This poses a problem for feature based segmentation across institutions.

1.6.1.4 Markov Random Fields

Markov random field segmentation is performed using a Bayesian framework[96]. Having the image Y we want to extract the desired segmentation X. Both image and segmentation are ruled by random processes. We then want to maximize the joint distribution of P(X|Y), the likelihood of having the segmentation X given the image Y. This requires an estimation of probability of the different classes of the image, tumour and background in the simplest case, and a spatial correlation between voxels. This information is used to construct a connectional graph with specified costs of assigning a voxel to one or the other class. The segmentation can be achieved by using a graph-cut algorithm[19].
Markov random fields methods allow segmentations where the connectional information of the voxels are taken into account. Furthermore using graph cut ensures that you have an optimal solution to the problem that you defined. The

Achilles Heel of the approach is of course the parameter specification. The success of the method is dependent upon the process where the model, the a priori parameters and the initializations are estimated or specified.

1.6.1.5 Deformable model

Deformable model methods require that you define an objective function[135]. The function can be governed by forces that arise either from outside the deformable model, as image intensities or gradients, or from the deformable model itself, as the shape of the deformable model. One of the popular segmentation approaches for 3-dimensional volumes is the level set methods. In level set methods you define a level set function. The function is defined in the same domain as the image. The level set function value is initially set to the distance of every voxel to an initial segmentation shape. Hereby all the voxels, with a level set value of zero, are the outer bounds of the segmentation. The value is signed so that the inside of the shape is set to negative values and the outside is set to positive values. The level set function is then set free to evolve according to a speed function. The speed function consists of different forces, which are defined according to the desired segmentation. For a description of formulation and practical implementation the reader is referred to [135].

1.6.1.6 Application of segmentation

Segmentation algorithms often use elements from different methods even though a distinction between methods has been made above. A Markov random field implementation will use a machine learning algorithm to estimate parameters. A feature based method could use deformable models to refine a segmentation. A subset of the implementations of GTV segmentation is categorized according to the primary algorithm of the approach in table 1.3. In [166] a comprehensive survey of the methods PET guided delineation methods is provided. To use a contour as evaluation reflects a pragmatic approach to the topic of segmentation evaluation. The available automatic segmentation methods should not be automatically implemented but rather used as a first guess and a time saver for the clinician[92].

Table 1.3: Categorisation of implementations for GTV segmentation for radiotherapy. The method marked with * are head and neck implementations.

Method	PET	PET/CT	CT
Thresholding	[103] [61]* [108]		
Background ratio	[36] [145] [54]* [53]* [152] [35]		[90]
Feature based	[14]	[163]* [164]*	
Markov random field	[70] [72] [71]	[63]*	
Deformable model		[102] [95]	

Chapter 2

Contributions

This chapter describes the 4 different contributions that are part of this thesis. The contributions are shortly introduced followed by a discussion of the results based on the knowledge of the author.

2.1 Differences in Radiotherapy Delivery and Outcome Due to Contouring Variation

The study was designed to answer some of the questions posed in the first chapter of the thesis regarding margins and operator variation. Using delineations from a study of inter-operator variation for lung tumour patients [116] dose differences were used to quantify the differences in dose and the differences in TCP given that one of the volumes is the true GTV.
The paper presents that the conventional compensation is not adequate for inter-operator variability and that TCP increases if the assumption of the approach is correct. This means that the inter-operator variation can have severe implications if adequately compensation is not made. The foreground-to-background ratio between tumour and the air cavity is high for lung cancer tumour. Consequently lung tumours are typically the easiest to contour. This indicates that the problem could be larger for other tumour sites. It is already a problem

that the variation is reported in so many diffent ways making it even harder to compare the variation between studies.
In the future a more thorough analysis of contour variation should be performed. The analysis should include margins for setup errors and the using monte carlo simulations for the delivered dose to a phantom tumour like Van Herk et al.[148]. The phantom should simulate the contour variation by simple quantitative differences, such as spherical harmonics.

2.2 Segmenting the Parotid Gland Using Registration and Level Set Methods

This article describes an application for segmentation of the parotid gland using non-rigid cubic-spline registration for a preliminary segmentation and then a refinement using level set methods. The approach was constructed to be able to segment 10 patients online at the conference workshop within 30 minutes. The approach would be able to contribute additional OAR if provided in the training data set. All the algorithms of the challenge delivered results which were clinically unsatisfactory. The proposed algorithm delivered inferior results compared to the winner of the clinical challenge. The winning algorithm[65] differentiated itself from the contributed algorithm by using NMI as dissimilarity measure and using the GPU for registration.
The contributing algorithm of this thesis had already been accelerated by parallel distribution of the cubic-spline registration computations on the CPU, but it is certain that the computing time could be further decreased by distributing the registration computations to the GPU. Han et al. describes how the GPU implementation gives a speed-up of 25 times to the registration. This increased computation capability could also be used to increase the number of levels for the registration or to implement NMI as a dissimilarity measure. NMI was initially rejected as a dissimilarity measure because it increased the computation time above the time constrains of the clinical challenge.
The proposed algorithm could be improved, by optimizing the parameters of the cubic b-spline registration method in a more quantitative method. The parameters used for the clinical challenge was estimated using a grid search. Some parameters and settings were already set on the basis of a qualitative assessment between two patients in the training set. The preset settings were the number of levels for the cubic-spline registration(3), the resolution of the downsampling (8,4,2) and the distance between cubic-spline knots on each level(32,16,8). These parameters should also have been optimized instead it was only the amount of regularization for each registration level and the parameters of the level set method that were optimized.

It can be seen from the figure 5.1 and 5.3 that the registration apparently misses the boundary head for some of the registered patient atlases since part of the resulting segmentation is situated outside the head. This could also suggest that the registration did not work properly for all of the patients. The winning algorithm also distinguished itself by using the STAPLE algorithm for combination of the transformed atlases where the contributing algorithm uses majority vote. On the basis of the results of Chen et al.[28] it could be interesting to analyse the effect of using the weighted correlation coefficient for the combination of the transformed atlases.
The deformable model of Han et al. seems to differ on the number evaluation points. Where the level set method evaluates the function in all the voxels, in our approach only the voxels close to the boundary are evaluated. Hereby the method only evaluates voxel and not discrete points The alternative algorithm seems to evaluate the energy function only in the points of the surface and should have subvoxel precision. It can be argued that a method that has sub-voxel precision produces a better segmentation of the parotid gland. The performance for the clinical challenge was evaluated on the basis of a delivered binary matrix. Therefore there was no incentive to acquire a subvoxel segmentation. Furthermore it is possible to extract a discrete surface from the level set function if necessary.

2.3 Segmentation Using Symmetry

This contribution is a novel method for GTV segmentation. It features a novel registration-based approach to derive symmetrical descriptors of the image. The method reflects to some degree the situation in the clinic where the radiologist evaluates high-dimensional descriptors as image symmetry and tissue expansion. The image is compared to the impression of normality given from the atlas.
A lot of parameter testing was performed before choosing the final parameters for the algorithm. It is always possible to examine the parameters of the registration method and change the number of registration levels, downsampling, spacing between and regularization. All these parameters were optimized using a grid search on the phantom and the method which parameter settings were the least suspectible to noise, rotation and translation.
It was chosen to represent segmentation only by thresholding. This was performed to reflect the value of the method by itself and not its implementation with another segmentation algorithm. The extracted symmetry feature can be used as input to more advanced segmentation methods as deformable models, machine learning and markov random fields methods.
So far the algorithms proposed in this field for segmentation uses either the raw intensity image values or classical texture features of both the CT and PET

images. A new segmentation algorithm would benefit from a thorough data mining process to identify features for tumour classification. An algorithm was implemented on the patients from Rigshospitalet which did improve the results of conventional automatic PET segmentation methods[77]. The algorithm provided improvement of segmentation results similar to the published algorithms using textural features[164]. But the algorithm had some problems with artefacts in the images with features that resemble tumours usually identified as inflammation of normal tissue
The new feature should be extracted along with typical texture feature and then tested against other features using machine learning algorithms such as adaboost[50] or random forest[75]. In order to increase the robustness of the algorithm the bootstrap-like method should be applied to examine whether the certain feature selections are influenced by outliers.

2.4 Lung Tumor Segmentation Using Electric Flow Lines for Graph Cuts

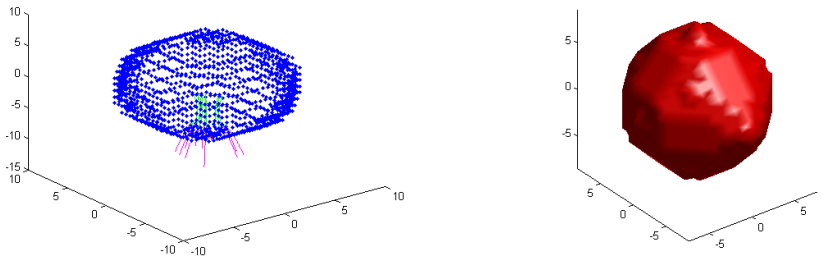

(a) (b)

Figure 2.1: Illustration of the simulated phantom with electric flow lines. (a) The contour points and electric flow lines. (b) The volume of phantom.

This contribution consists of an article describing adaptable segmentation framework for lung cancer patients. The method uses electric flow lines to construct a segmentation graph. The change in the cancer type reflects the available image type available. On megavoltage computerized tomography (MVCT) images the outline between different types of soft tissue is almost non-existent and therefore it is laborious to manually contour the GTV for head and neck cancer. Furthermore these contours would be prone to larger intra- and inter-operator variation. Therefore an easier cancer type was chosen for the development and

evaluation of the method. Lung cancer is easier to contour since the tumours are surrounded by air to a certain degree.
The parameters of the approach was estimated using a simulated phantom illustrated in figure 2.1. The parameters were estimated after simulation of dilation/expansion of the volume, rotation of the volume, translation and signal-to-noise levels. The phantom consists of a sphere with 2 hemispheres and 2 pyramid. The two different types of surface features were included to check whether the method would robust against rotation. The surface features were placed 90 degrees apart for different kinds of surface features, i.e. pyramid to hemisphere, and 180 degrees apart for surface feature of the same kind.
The study shows that a method that is adaptive to the shape of the tumour is better for adaptive segmentation of tumour. Reflecting on the conventional method of non-rigid registration you realise that the argument for this relative failure maybe lies in definition of the problem when using non-rigid registration. Lung tumours does retain some of the shapes characteristics from the CT to later MVCT images. But the image quality does make it hard to find point correspondence and sometimes the theoretical question would be whether the point correspondence is achievable under these conditions.

2.5 General Perspective

Coming from the discipline of science and working in the twilight zone of biology, physics, and pathophysiology you generally yearn for a piece of golden truth to improve and evaluate your methods. In the instance of image analysis for radiation therapy this is generally hard to ascertain. Even in the instance of surgical removal of tumour specimen the procedure to acquire the sample and points correspondence are attached with many potential errors. Even so, all the studies presented in this thesis should be evaluated using the highest possible evidence before using them in a clinical setting. The performance ambition of developing automatic methods for segmentation should be higher than the conventional and manual methods already applied in the clinic.

2.5.1 Segmentation algorithms

As it can be seen from the thesis and the reviews in table 1.2 and 1.3 there is presently a high number of different segmentation algorithms available. With increasing number of algorithms the need for a criterion of robustness and performance must be developed[93].
In [130], 30 different contouring methods are evaluated on 7 different VOIs.

Four of the VOI are coming from an phantom which has been created to resembled a patient but with the knowledge of the geometry and control of the activity. The remaining 3 VOI are coming from 3 different patients. Unfortunately the number of VOIs is not high enough to clearly distinguish the different methods. They report that future studies should involve more data and they report that they would make the evaluation data available in the future.
Another commendable initiative has been the grand challenge of the MICCAI conference[113][114]. In this setting all the involved algorithms get the same data set and the same amount of time to do the segmentation of the normal tissue. The same challenges could be performed for tumour segmentation if reliable GTV contours were available.
The American Association of Physicists in Medicine has started a task group with the aim to classify PET segmentation methods according to assumptions, algorithmic approach, detail, complexity and goal[2]. The task force expires by the end of 2012 and should provide a report on the subject by then.
But the field of radiation therapy should increase cooperation on collecting patient scans with reliable segmentations. Having scans available from multiple institutions with tumor definition would enable identification of the most reliable algorithms for different segmentation tasks. The methods developed for this thesis are good candidates and does not involve any assumptions which makes it suitable for the data coming from other institutions.
Implementation of the algorithms in the clinic is not straightforward. Before clinical introduction, segmentation algorithms should be adequately tested to evaluate their impact on clinical practice. [136] shows an example of evaluation of a lymph segmentation method. In this study the VOI is countoured manually and automatically whereafter the automatic segmentation were manually modified. The results show that it is possible to reduce manual variability. Similar studies should be performed before implementing automatic segmentation methods.

2.5.2 Future of radiation therapy planning

The development of automatic segmentations and better understanding of tumour specific image features allows a new approach to VOI definition. It allows a progression within radiation therapy towards a new understanding of target definition. Since surgical specimen removal is the only approach which delivers an absolute definition of tumour infiltration, segmentation methods should rather deliver probabilities of tumour presence. Different components of the segmentation or delineation do not have the same level of uncertainty. This is illustrated in figure 2.2 with manual segmentations. The internal core of the segmentation should have a lower level of uncertainty than the exterior parts. In the same way tumour definition arising from one image modality should have a

lower level of confidence than a definition which is seen on several image modalities and in the clinical examination. An quantitative algorithm should deliver the uncertainty information of the VOI segmentation and not only a binary segmentation.

The other components of the planning procedure of radiation therapy already

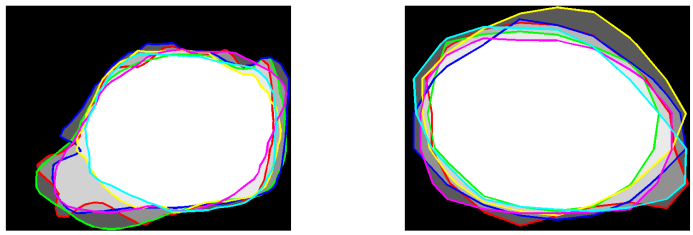

(a) (b)

Figure 2.2: Illustration of the GTV probability. 6 manual contours of the same GTV in different colours. The underlying image coulour defines a theoretic GTV probability on the basis of the contours. (a) and (b) illustrates the difference between a tumour with respectively a low and high level concordance.

work with uncertainties of the dose delivery and treatment execution. Using the new segmentation probabilities in the frame of treatment planning could increase adaptability for the individual patient. Today the dose plan is defined due to a specified GTV location given the uncertainties of preparation and execution errors. At this level the uncertainty of the segmentation is partly disregarded. Instead an increase of the margin is included to account for any uncertainty. The future dose plan should be defined due to the probability of GTV location given the uncertainties of execution and planning errors. The new method would reflect the actual segmentation situation and the underlying images while increasing planning complexity. Specification of GTV probability necessitates automatic segmentation since manually it is only practically possible on the basis of a multitude of time consuming manual delineations from several experts using STAPLE [155]. The GTV probability could rely on the result from several algorithms. The algorithms would then be weighted on their performance of on data sets from different institutions consisting of images with a reliable GTV definition.

Chapter 3

Conclusion

This thesis descibes the use of algorithms for automatic segmentation along with their subject area. It is shown that it is possible to automatically segment tumour volumes and organs. It is also shown that great care must be put into the construction of these volumes since they have great importance for the treatment outcome. If the variation due to manual contouring is not adequately compensated it can lead to decreased TCP.
It was shown that it is possible to segment GTV and normal tissue using automatic segmentation. The automatic methods should always be supervised and edited upon need. Even so they have the potential for increasing the workflow of the contouring of normal tissue and GTV and decreases the bottleneck it poses for the modern radiation treatment clinic.
Furthermore a new method for adaptive contours has been presented. The method is less susceptible to the image quality than the conventional methods for this application. These images taken during the course of treatment does have a lower quality than the conventional CT and therefore it is important to use methods that are less prone to the image quality.
The work of this thesis is a step towards the application of more advanced image analysis in the clinic to improve care of the patients and decrease the need for manual labour for radiation treatment planning.

Differences in Radiotherapy Delivery and Outcome Due to Contouring Variation

Chapter 4

Differences in Radiotherapy Delivery and Outcome Due to Contouring Variation

4.1 Abstract

Gross tumor volume (GTV) delineation is central for radiotherapy planning. It provides the basis of the clinical target volume and, ultimately, the planning target volume which is used for dose optimization. Manual GTV delineations are prone to intra- and inter-operator variation and automatic segmentation methods also produce different results. There is no consensus on how to account for the contouring uncertainty, but it has been suggested to incorporate it into the planning target volume (PTV) margin. Current recipes for the PTV margin are based on normal distribution assumptions and are more suitable for setup and execution errors. In this study we use the GTV delineations made by 6 experienced clinicians to create delineation-specific dose plans. These dose plans are then used to calculate theoretic tumor control probabilities (TCP) differences between delineations. The results show that current margin recipes are inadequate for maintaining the same TCP despite manual delineation variation. New methods to account for delineation variation should be developed.

4.2 Introduction

Cancer is one of the deadliest human diseases, responsible of 7.6 million deaths in 2008 [1]. The yearly incidence is 12.7 million new cancer cases annually and with cancer incidence rising along with the worldwide increasing life expectancy, it is one of the largest large burdens upon the health systems of the world.

Treatment of cancer with radiotherapy has increasing application in the modern clinic. Radiotherapy is based on a specification of the tumor volume called the Gross tumor volume (GTV). In the present day clinic this volume is manually contoured by a radiologist and/or a radiation oncologist. The GTV is contoured upon the basis of the physical examination of the patient and available images from different modalities such as Computerized Tomography (CT), positron emission tomography (PET) and magnetic resonance imaging (MRI) [83]. The delineation of the GTV is subject to both inter- and intra-operator variation [137] [67].

After the GTV has been defined a clinical tumor volume is defined to account for volumes with suspected or probable microscopic malignant disease. Finally a planning target volume (PTV) is defined to account for geometrical errors both systematic and random. These errors arise due to uncertainties in delineation, setup and equipment. Several studies have been performed with the aim of determining margin recipes for PTV [147]. These models all build on the assumption of random normal distributed errors, which might not be correct for delineation variation that arises from manual delineation.

When the (PTV) is finally constructed it is possible to make a dose plan with a dosimetric goal for the tumor. The radiotherapy delivery parameters such as field size, position, and dose profile are then optimized to create a plan with an optimal tumor control probability (TCP) and the lowest possible normal tissue complication probability (NTCP). NTCP refers to the damage of organs at risk (OAR) due to radiation which will cause complications with some probability. The whole radiotherapy workflow is shown in figure 4.1.

For all these steps from the tumor delineation to the dose plan, the present study evaluates the practical implication of different contours on the final treatment plan. We use manual contours on images from previously treated patients to compute dose plans. With the differences in dose plans available it is also possible to quantify the difference in TCP assuming that each of the contoured GTVs represents the true tumor volume.

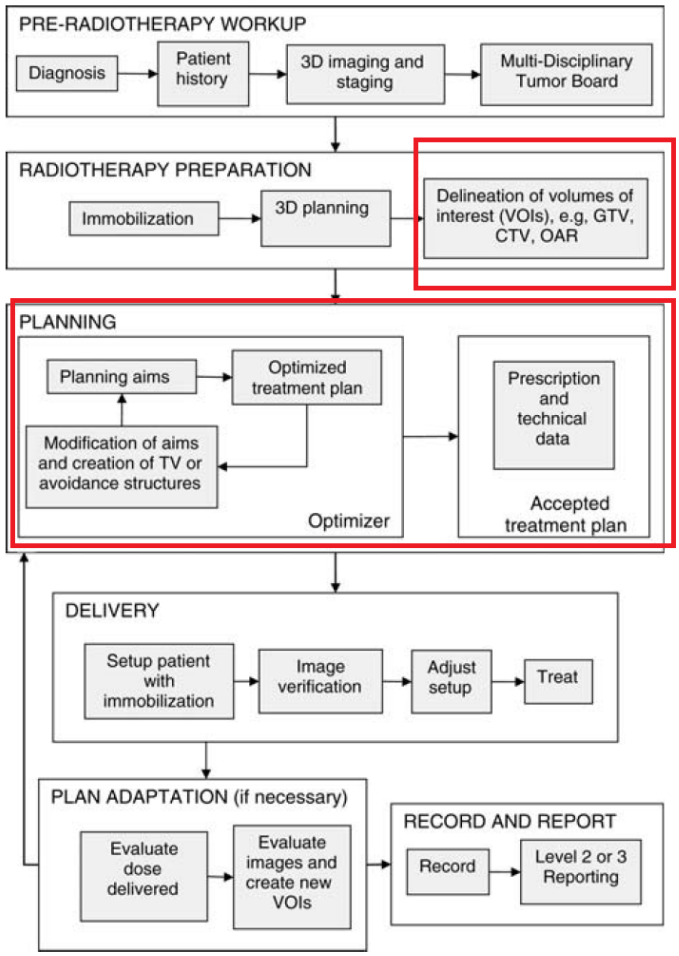

Figure 4.1: Illustration of the radiotherapy workflow. The red marking indicates the parts which are handled in this study. Adapted from [83]

4.3 Methods

The workflow theory of the present study is defined and the experiments made are explained in this section. With a GTV contour, $GTV_{(p,c)}$, for patient p made by the manual contourer c the PTV, $PTV_{(p,c)}$, can be calculated as

$$PTV_{(p,c)} = GTV_{(p,c)} \bigoplus M \tag{4.1}$$

where $\bigoplus$ is a morphological dilation and M is the margin dilation volume, which can be dependent on location. To acquire a margin of x width M should be a sphere with radius x but it is also possible to use other volumes to account for other margin definitions. When the $PTV_{(p,c)}$ is acquired it is possible to optimize a dose plan, $D(r_{(p,c)})$. The radiotherapy delivery parameters, $r_{(p,c)}$, are then optimized to acquire the plan with the highest TCP and lowest NTCP. TCP can be defined as

$$\arg\max_{r_{(p,c)}} = w_{TCP} \cdot TCP\left(r_{(p,c)}\right) - w_{NTCP} \cdot NTCP\left(r_{(p,c)}\right). \tag{4.2}$$

where w_{TCP} and w_{NTCP} are parameters weighting for TCP and NTCP, respectively. TCP is defined as [156]

$$TCP(\mathbf{D}) = \prod_{v \in GTV} \exp[-\rho(v) \cdot s \cdot \exp\left(-\alpha(v) \cdot D(v)\right)] \tag{4.3}$$

where v is a volume size inside the tumor volume(could be a voxel), ρ is the density of cells, s is the size of the voxel, $\alpha(v)$ is the cell survival term from the linear-quadratric model [39] and $\mathbf{D}$ and $D(v)$ are the doses given to the whole volume and the subvolume.
In practice, TCP is not calculated in the clinic, but the optimization is performed by setting constraint parameters for the DVH [42], a 2D summarization of the 3D dose distribution. These constraints emphasize the importance of a high dose to the tumor and low dose to the OAR. These constraints and their weighting are set from experimental in vitro data and analyses of dose plans and outcomes from historical patients. Using $D(r_{(p,c)})$ for the different clinicians it is possible to calculate the relative risk in TCP due to contours as

$$\begin{aligned}\Delta TCP(c_1, c_2, p) = \prod_{v \in GTV(p,c_1)} & \exp\left[-\rho(v) \cdot s \cdot \left(\exp(-\alpha(v) D(r_{(p,c_1)})(v)\right)\right. \\ & \left. - \exp\left(-\alpha(v) D(r_{(p,c_2)})(v)\right)\right)\Big]\end{aligned} \tag{4.4}$$

c_1 and c_2 are the two contours for which the dose plans are being evaluated. If 100 % TCP is expected using c_1 then 4.4 gives the new TCP when c_2 is used to create the dose plan.

4.3.1 Experiments

The data consisted of contours and images from 10 patients referred for stereotactic body radiotherapy in 2008. All patients had NSCLC and were treated at our institution. All patient tumors were delineated independently by 3 radiologists and 3 oncologists who had CT images and the PET information on each

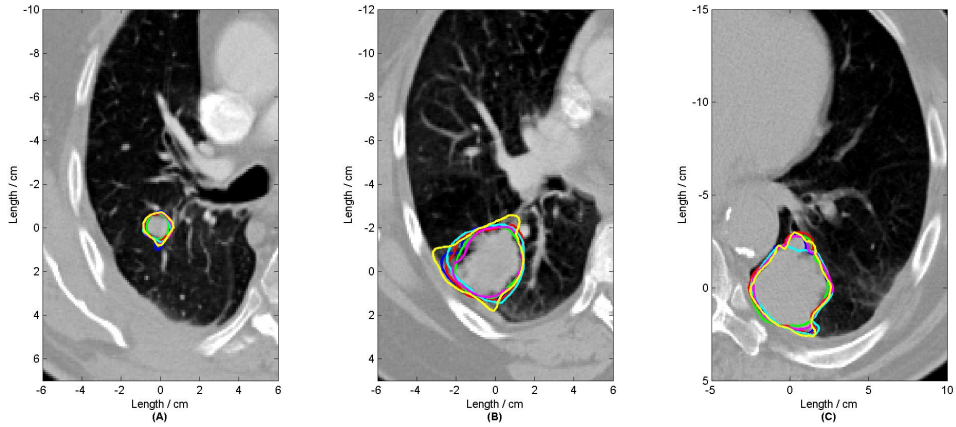

Figure 4.2: Examples of the contours for three patients. (A), (B) and (C) illustrate the transaxial plane of two different patients. The delineations are shown in different colors.

patient. PTVs were constructed by dilating all delineations using an ellipsoid volume. The ellipsoid was constructed to satisfy margin recipe [148] with errors calculated from the contours [115]. An example from two patients can be seen in figure 4.2.
Each of the PTVs were the imported into the Eclipse planning system and the dose plans were optimized using the software. The plans were made using the settings for both IMRT and RA delivery methods. These two methods represent the most widely used delivery methods. IMRT has a number of beams to give the radiotherapy where RA delivers the radiation over an arc therefore further accommodating the radiation field to the planning volumes. Therefore we evaluated both methods to survey any differences between the methods. Constraints for normal tissues and tumors were kept uniform for all the patients. Normal tissue sparing was performed for the lungs and the spinal cord. The dose plans were then evaluated using equation 4.4 with $\alpha = 0.35$ from in vitro experiments [39] The cell concentration was set isotropic to $10^{-7}cm^3$ within the GTV with decreasing cell concentration towards the last centimetre to the edge. Since we are only interested in TCP reductions from c_1 to c_2 we ignore all contributions from voxels , v_n, with a dose larger than the minimal dose within the GTV. I.e.

$$v_n \in \left\{ v | \left(D(r_{(p,c_2)})(v) \geq \min_{v \in GTV(p,c_1)} \left(D(r_{(p,c_1)})(v) \right) \right) \right\} \tag{4.5}$$

Hereafter the TCP differences were tested using a one-way student t-test with a significance level of 0.05. The data is probabilities between 0 and 1 so the data is

logit transformed to satisfy normal assumptions. Comparisons were only made between dose plans optimized for the same delivery methods.

4.4 Results

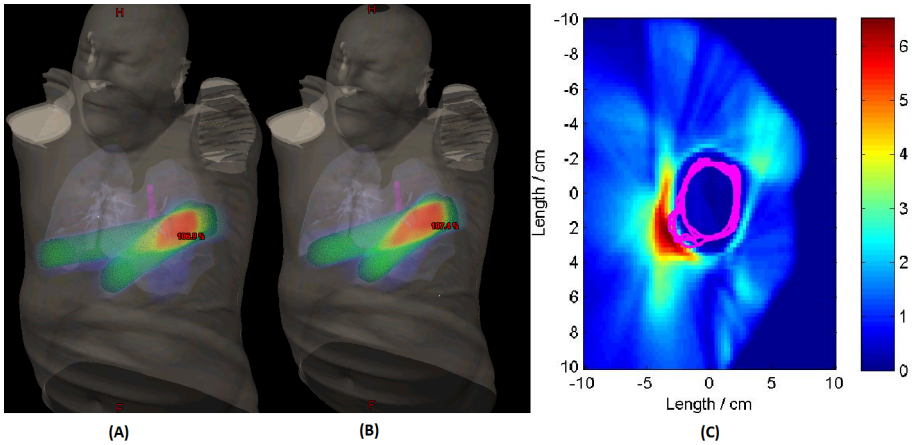

Figure 4.3: Examples dose plans and their variation. (A) and (B) 3-dimensional view of the same patient with a dose plan optimized for two different delineations. (C) 2-dimensional view of the variation between all the dose plans for a single patient on a slide with the original GTV contours given in magenta. The color indicates the standard deviation for each voxel between the dose plans.

120 plans were optimized for the ten patients. An example of the plans is shown in figure 4.3. There were dose differences between the PTVs of the different delineations and they varied both between methods and patients.
The TCP calculation gave a mean of 81 %, standard deviation of 32 %, median of 96 %, and a range of [0−100] for RA and a mean of 77 %, standard deviation 35 %, median of 98 %, and a range of [0−100] for IMRT. A student t-test rejected the null hypothesis with $p<0.0001$ for both delivery methods with ranges of [0.96-0.99] and [0.94-0.99], for IMRT and RA respectively. The 600 TCP results (10 patients · 6 contours · 5 comparisons · 2 delivery methods) are seen summarized in figure 4.4.

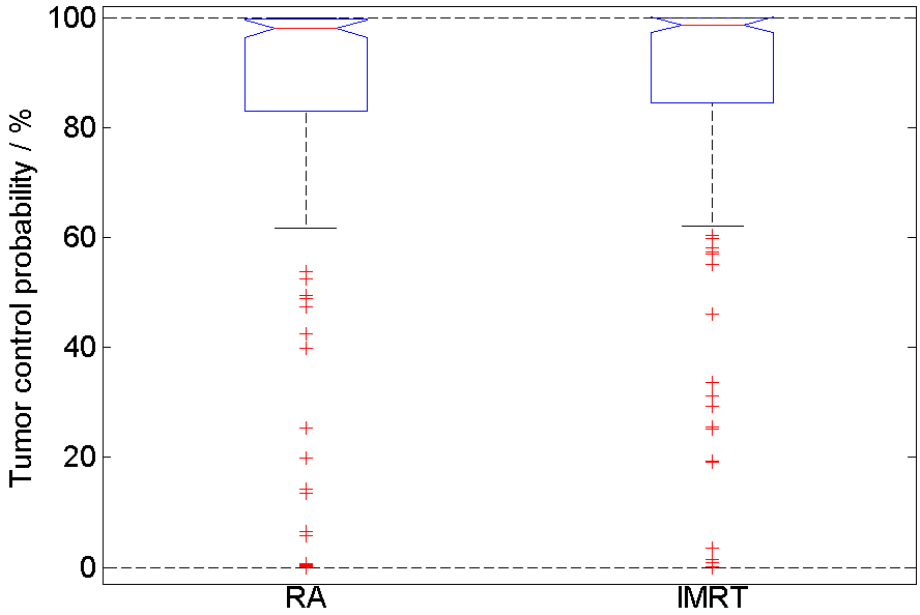

Figure 4.4: Box plot illustrating the inter-delineation TCP for intensity-modulated radiation therapy and Rapidarc©. On each box the central red mark is the median, the edges of the box are the 25th and 75th percentiles, the whiskers corresponds to approximately 2.7 SD, outliers are plotted as a line individually. The notches correspond to the confidence interval of the median.

4.5 Discussion

The results of this study show that current methods to employ margins to account for delineation variation are not sufficient to ensure the same level of TCP with contours done by different physicians. Generally a even larger TCP relative risk can be expected as lung tumors have relatively high tumor contrast and are easily contoured with less variation than tumors in other sites.
But there are also several assumptions underlying these calculations. First of all we assume that all delineations are correct by themselves in the calculation of TCP. However, this is definitely not correct since there exist only one tumor volume. The assumption is made just to show the implication of different delineations on the final dose plan.
Furthermore it is assumed that there is a perfect setup and execution of the dose delivery. This means that the margins only have to account for delineation errors. This assumption is due to the purpose of the study. Adding other margins would increase the TCP results but these margins account for other errors

and should not be employed to account for delineation errors. The margins are constructed on the basis of a margin recipe [147] which is determined using normal distribution errors, and the margin recipe was originally constructed to account for setup and execution errors.
There are also biological assumptions about the tumor biology which are not necessarily true. However, these parameters are extracted from the only available experimental data and therefore they are the most appropriate for this study. An isotropic cell density throughout the tumor. This is probably not true but it has not been possible to find applicable data to account for this. The assumption of isotropic cell density and biology should give a conservative measure of the actual TCP implication.
The present study indicates that new methods to account for delineation variation should be developed. It should be possible to find tumor specific margins which depend on both tumor- and nodal-stage. Furthermore delineation studies might reveal image features which correlate with delineation variation. It also shows the need for additional studies which correlate image data with actual tumor specimen taken from patients as [35] and [150]. Studies which correlate tumor probability with image feature could be a stepping stone to a sophistication towards probabilistic definition of tumor cells instead of the current tumor/not tumor definition. It is important though, that these studies are performed across institutions. This would ensure that the results are not biased by specific patient populations and especially equipment, which has been shown to give variations in image features [51]. These studies should be performed on a larger scale and across institutions so the obtained features do not reflect a single scanner.
The present study does not touch upon the subject of NTCP calculation. Using the same method it is also possible to look at the NTCP differences arising from delineation variation of GTV and OAR definition. The NTCP is also influenced by delineation variation but with increasing distances from the GTV to the OAR the effect would be negligent.

4.6 Conclusion

This study shows that current methods are not sufficient to account for delineation variation arising from inter-operator delineation variation. Better margin recipes specifically constructed for delineation variation are needed.

Segmenting the Parotid Gland Using Registration and Level Set Methods

Chapter 5

Segmenting the Parotid Gland Using Registration and Level Set Methods

5.1 Abstract

The bilateral parotid glands were segmented using a registration scheme followed by level set segmentation. A training set consisting of computerized tomography from 10 patients with segmentation of the bilateral glands was used to optimize the parameters of registration and level set segmentation. The method was evaluated on a test set consisting of 8 corresponding data sets. The attained total volume Dice coefficient and mean Haussdorff distance were 0.61 $\pm$ 0.20 and 15.6 $\pm$ 7.4 mm respectively. The method has improvement capabilities for potential clinical introduction.

5.2 Introduction

Cancer is the greatest killer worldwide accounting for more than 7,5 million deaths[52]. Radiotherapy has become a large part of the clinical treatment of

cancer. Newer, more sophisticated and intelligent methods for applying radiation has allowed clinicians to radiate volumes precisely with greater doses[15]. This leads to a demand for precise contouring methods for cancer tissue as well as healthy tissue which should be spared from the harmful radiation. Manual contouring on computerized tomography (CT) images has been the prevalent method used in the clinic for delineating volumes of interest (VOI).
But manual contouring has shown to have several drawbacks. The method shows variability both inter-subject and intra-subject in contouring tumors[22] as well as healthy tissue[136]. The method is also time consuming in a clinic with increasing patient flow and a high emphasis on budget control. Automatic segmentation methods seem to be the solution to these problems [66]. These methods could pre-process the images of the patient creating contours for VOI. Leaving the radiation oncologist to evaluate and modify the contours instead of manual contouring.
In this paper we show that automatic contouring of the bilateral parotid glands is possible by combining registration and level set methods. The registration method uses a diffusive regularizer and uses basis functions to interpolate the image[68]. All patients with segmented parotid glands are registered into the patients with unknown segmentations. The volume where most of the transformed segmentations are located is taken as an initial guess for the level set segmentation. The level set segmentation is based on the work by Osher and Sethian[110] and is dominated by extrinsic and intrinsic forces.

5.3 Data

The provided data set consisted of 18 CT datasets from Princess Margaret Hospital representing a subset of a real clinical patient population. The CT resolution was 0.98 mm in both direction of the transversal plane and 2.0 mm along its axis. The data was given as values between 0 and 4096 with a value of 1000 regarded to be 0 HU. In the transversal plane the dimensions were 512 by 512 voxels and with 108-191 slices along the transversal axis.

10 of the datasets were supplemented with manual segmentations of the bilateral parotid glands, henceforth called the training set. The manual segmentations had been created by a clinical expert using standard manual delineation tools. The segmentations were provided as a volumetric binary mask with the same dimensions as the corresponding CT. The remaining 8 datasets without segmentations are referred to as the test set.

5.4 Methods

To decrease the computational load of the registration the CT data were initially reduced. The reduction was performed automatically to remove slices below the upper part of the neck and above the lower part of the nose. The coronal axis was cut at the front of the mandibles and in the back around the ears. The saggital axis included all of the head.

5.4.1 Image Registration

The registration used in this work is shortly summarized in this section. For more extensive information about the methods used the reader is referred to[68]. The registration consists of two individual transformations. A preliminary affine registration to align head position and size followed by a cubic b-spline registration to align organs, bones, and surfaces. The parameters of the registration was found by minimization of the objective function

$$C[R, T; \phi] = D[R, T \circ \phi] + \alpha S[\phi], \tag{5.1}$$

where R is the reference image, and T is the template, with a segmentation, which we will transform into the reference. ϕ is the transformation, D is the dissimilarity measure, in this instance sum of squared difference, S is the regularizer described below, and α is a trade-off constant.
The scale space of the image was used for the registration to avoid a local minimum solution. Afterwards the CT data was interpolated by combinations of 1 dimensional cubic b-splines. The knots of the splines were placed at each sampling point and provided spatial derivatives. In order to find the coefficients of the splines a linear system was set up

$$\mathbf{Bw} = I, \tag{5.2}$$

where $\mathbf{B}$ is a sparse matrix consisting only of the spline basis for one knot along each row, $\mathbf{w}$ is a matrix consisting of the spline coefficients, and I is the image matrix that we are interpolating.
Afterwards the transformation of the template could procede. Each of the transformations are parametrically defined as

$$\phi(\mathbf{x}; \mathbf{p}) = \mathbf{x} + \mathbf{u}(\mathbf{x}; \mathbf{p}) = \mathbf{x} + \mathbf{A}(\mathbf{x})\mathbf{g}(\mathbf{p}), \tag{5.3}$$

where $\mathbf{x}$ is the position vector, $\mathbf{p}$ is the transformation parameter vector, $\mathbf{A}$ is the spatial basis, and $\mathbf{g}$ is the parameter kernel.
For the affine transformation a solution is found relatively easy because of the

few number of parameters. But when making the cubic b-spline transformation a regularizer is needed. The used diffusive regularizer was defined as

$$S_{dif}(\phi) = tr(\nabla \mathbf{u}^T \nabla \mathbf{u}^T), \tag{5.4}$$

where $\nabla \mathbf{u}$ is the relative displacement gradient.
Once the problem has been defined and discretized it is then possible to optimize the transformation parameters using a limited memory Broyden-Fletcher-Goldfarb-Shanno algorithm[105].

5.4.2 Level Set Method

We are interested in surfaces when using the level set methods for segmentation. A matrix of the same size as our image is defined and the surface voxels are represented with 0 and every other voxel represented as the distance to the closest point of the surface, negative inside and positive on the outside of the surface. These are the level set values. The result of the registration was employed as the initial surface. The surface evolves iteratively by using the following equation

$$\eta^{n+1,\mathbf{x}} = \eta^{n,\mathbf{x}} - \Delta t \left(\mathbf{V}(\mathbf{x}) \cdot \nabla \eta^n(\mathbf{x}) + \mathbf{a}(\mathbf{x}) - \mathbf{b}(\mathbf{x}) \right), \tag{5.5}$$

where η is the level set value, n is the current evolution, Δt is the time step for each iteration, and the three force fields: $\mathbf{V}$ is the velocity field, $\mathbf{a}$ is the speed field, and $\mathbf{b}$ is the curvature field.
$\mathbf{V}$ is the force, that pulls the surface towards the edges by influencing the level set value. It is derived by taking the gradient, $G(\mathbf{x})$, of the CT image. The velocity field is then defined as $\nabla |G(\mathbf{x})|$. $\mathbf{a}$ is the force that pulls the surface in the direction normal to the surface. It is defined to be high when the value of the HU is close to the mean of the parotid gland and negative, when away. $\mathbf{a}$ was computed as the value of a gaussian distribution with the mean and standard deviation of the segmented parotid glands of the training set. $\mathbf{b}$ was calculated from the underlying level set values computing the curvature from the gradients. For a more detailed description of the method and its capabilities the reader is referred to [109].

5.4.3 Optimization of parameters

Parameters for the registration and level set segmentation were found by the leave-one-out strategy on the training set. The objective function was the combined Dice coefficient (DSC) of all slices between the new segmentation and

the manual segmentation. The transformed segmentation templates were combined by addition, and then a final registration segmentation was found, using a threshold value.
The parameters were found making consecutive grid searches over the parameter and threshold values in the following order: Registration parameters, threshold of registration combination and level set parameters. Afterwards the test set was segmented using the parameters and thresholds attained from the grid searches. The attained threshold parameter was corrected for the total number of templates (multiplying with $\frac{10}{9}$), when segmenting on the test set.

5.5 Results

The parameters for the registration were found and the individual transformed segmentations were combined as described in section 5.4.1. Figure 5.1 shows examples of the individual registration along with their combination. Table 5.1 shows the DSC results which confirms, that the individual registration results vary and that the resulting combination is a reasonable compromise. In figure

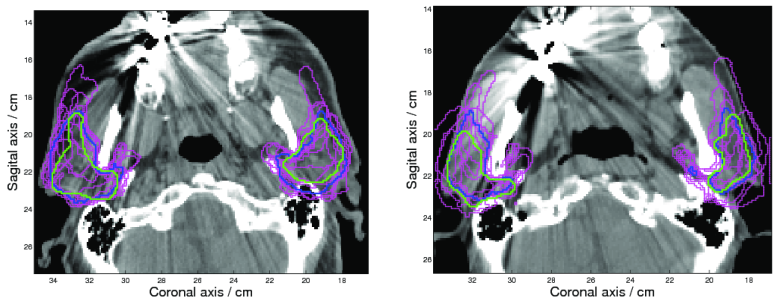

Figure 5.1: Example of the registration result. Manual segmentation in green, individual registration in magenta and combined registration in blue. To the left data set 1, to the right data set 3

5.2 the results of the level set segmentation is seen along with the initial segmentations. It can be seen that the level set segmentation is less smooth than the initial segmentation. The changes are minor, which is also confirmed in table 5.1. It is seen that the level set segmentation increases the DSC slightly, but not significantly, $p = 0.3$, on a pooled t-test. Examples of the test set segmentations is shown in figure 5.3. The contour is coarse and generally includes the dermis and subcutaneous tissue, which are not part of the manual segmentation. The resulting statistics for Hausdorff distance (HD) and DSC can be seen in table 5.2 and 5.3 respectively. In table 5.2 it is seen, that HD is larger than the

	Left parotid			Right parotid			Combined		
Set	**Ind.**	**Com.**	**L.S.**	**Ind.**	**Com.**	**L.S.**	**Ind.**	**Com.**	**L.S.**
1	0.5 ± 0.2	0.53	0.54	0.54 ± 0.2	0.65	0.63	0.52 ± 0.2	0.59	0.58
2	0.53 ± 0.1	0.76	0.78	0.59 ± 0.2	0.77	0.78	0.56 ± 0.1	0.77	0.78
3	0.62 ± 0.1	0.79	0.8	0.66 ± 0.1	0.82	0.84	0.64 ± 0.1	0.8	0.82
4	0.52 ± 0.1	0.55	0.69	0.53 ± 0.1	0.46	0.6	0.52 ± 0.1	0.51	0.64
5	0.59 ± 0.1	0.64	0.69	0.62 ± 0.1	0.6	0.71	0.61 ± 0.1	0.62	0.7
6	0.46 ± 0.1	0.6	0.66	0.54 ± 0.2	0.7	0.75	0.5 ± 0.1	0.65	0.7
7	0.51 ± 0.2	0.76	0.77	0.51 ± 0.1	0.73	0.77	0.51 ± 0.2	0.75	0.77
8	0.57 ± 0.1	0.58	0.68	0.48 ± 0.1	0.52	0.64	0.53 ± 0.1	0.55	0.66
9	0.62 ± 0.1	0.82	0.84	0.63 ± 0.1	0.84	0.83	0.63 ± 0.1	0.83	0.84
10	0.58 ± 0.1	0.81	0.83	0.5 ± 0.2	0.65	0.7	0.54 ± 0.2	0.73	0.77

Table 5.1: DSC scores of the registration. Ind. is the individual transformed segmentations from the registration scheme, Com. is the combination of the individual segmentation and L.S. is the level set result. The result of the individual segmentations is given as the mean DSC $\pm$ one standard deviation.

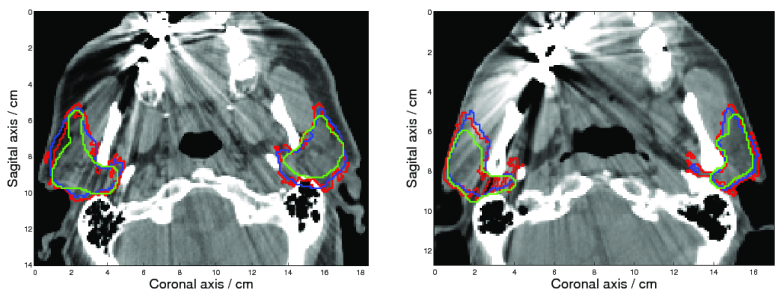

Figure 5.2: Example of the level set results along with the initial segmentation from the registration. Manual segmentation in green, combined registration in blue and level set segmentation in red. To the left data set 1, to the right data set 3

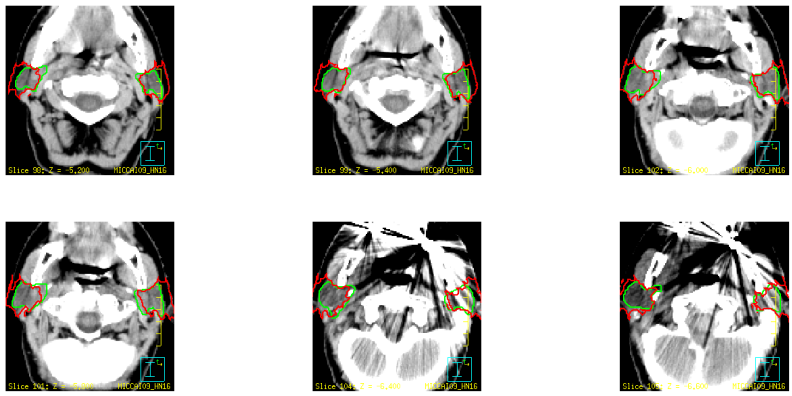

Figure 5.3: Example of the registration result from different slices of data set 16 of the test set. Manual segmentation in green and the final segmentation in red.

	Mean HD		Median HD		No. of slices (HD > 3 mm)	
Set No.	Left	Right	Left	Right	Left	Right
11	12.97	8.36	12.69	8.05	34 (34)	32 (32)
12	18.56	17.71	18.57	16.00	28 (28)	30 (30)
13	8.73	10.59	8.79	10.74	26 (26)	26 (26)
14	15.49	14.87	13.21	12.70	24 (24)	24 (24)
15	11.09	10.61	10.55	9.67	23 (23)	26 (26)
16	10.80	8.60	9.81	8.37	29 (29)	31 (31)
17	18.46	19.66	18.20	19.53	33 (33)	27 (27)
18	34.07	29.62	32.21	28.44	24 (24)	25 (25)

Table 5.2: Hausdorff distances (HD) statistics for left and right parotid segmentation in the testing datasets.

clinically acceptable 3 mm deviation on all slices for all data sets. In table 5.3 it is seen that the DSC lie in the same range as the training set, except for data set 18. The initial segmentation (not shown) from the registration is located over the temporal parts of the skull.

	Average slice		**Median slice**		**Total volume**	
Dataset No.	Left	Right	Left	Right	Left	Right
11	0.62	0.77	0.66	0.81	0.68	0.81
12	0.53	0.56	0.57	0.59	0.56	0.59
13	0.78	0.70	0.80	0.74	0.78	0.72
14	0.62	0.55	0.71	0.60	0.67	0.60
15	0.77	0.78	0.82	0.82	0.81	0.82
16	0.55	0.61	0.63	0.63	0.61	0.67
17	0.46	0.47	0.53	0.54	0.52	0.57
18	0.11	0.15	0.11	0.14	0.14	0.20

Table 5.3: Dice coefficient statistics for left and right parotid segmentation in the testing datasets.

5.6 Discussion

The results in table 5.2 show that the proposed method underperformed in relation to the clinically acceptable HD. This is mainly due to the fact, that the parameters have been optimized to increase the DSC as much as possible. Instead of optimizing the method based on the DSC, one could make an optimization based on an intermix of HD and DSC.
Furthermore it did not achieve an DSC above 0.5 for data set 18. This did not happen in the training set. This could be caused by dissimilarity between the patient of data set 18 and the patients of the training set. As commented earlier the segmentation from the initial registration is dislocated, which could be corrected by adjusting registration parameters.
The method was constructed to be a fast segmentation method. At the current time it can segment a new patient on an average of 60 seconds. A number of parameters could be changed to increase the performance of the method but also increase the computation time. The number of cubic b-spline registrations could be increased to increase the DSC of the initial registration. This could be achieved by increasing the number of cubic b-spline registrations with initial high downsampling and high scale space to align the overall structures followed by registrations of lower or none downsampling and lower scale space to align

tissue, bones and surfaces. The number of iterations for both transformations was set low to ensure fast segmentation. By increasing the number of iterations the performance could have been increased but at the expense of computational time of the segmentation. A tolerance limit for the registration algorithm could also solve the problem without setting the number of iterations.
The level set method did improve the initial segmentation, but it was devised as a final refinement of the results, and hence it did not change the segmentation significantly. Moreover the curvature parameter was decreased so much, that it produced a coarse surface. Future studies could inspect an optimization scheme based on an intermix of HD and DSC, which could have improved the results of the level set segmentation.

5.7 Conclusions

We have shown that it is possible to segment the bilateral glands automatically using registration and level set methods. The method has development possibilities which could be harnessed to enable clinical introduction.

Acknowledgements The authors acknowledge the Head & Neck Site Group of the Radiation Medicine Program at the Princess Margaret Hospital, Toronto ON Canada for providing the data sets. Mr. Hollensen thanks the graduate school programme IT Everywhere from the Danish Agency for Science Technology and Innovation.

Segmentation Using Symmetry

Chapter 6

Segmentation Using Symmetry

6.1 Abstract

The manual delineation of gross tumour volume(GTV) for radiation therapy for head and neck cancer patients relies in some degree on pathological deviation from normal anatomical symmetry. This study introduces a novel 3-dimensional symmetry quantification method and evaluates it for the segmentation of GTV. The method uses deformable registration on computed tomography (CT) to find anatomical symmetry deviations of head-and-neck squamous cell carcinoma. The information is combined with the signal from positron emission tomography (PET) images. The method allows the use of anatomical and symmetrical information from CT and PET scans to improve automatic delineations. 30 head-and-neck patients with PET/CT scans were automatically segmented in this study. The proposed method delivers a mean area under the curve of 0.87 for receiver operating characteristics and delivers a higher true positive rate than comparable PET thresholding methods for PET images at low false positive rate.

6.2 Introduction

Symmetry is an obvious quality of many biological systems. This may stem from the biological fact that the basis of life is performed by mitosis, cell division. Symmetry in the human body has a lot of benefits, e.g. an additional backup in case of the breakdown of one organ.
In previous studies symmetry shape distortion due to pathology has been quantified using registration [106] [37] [41]. Tumor development is exactly a disturbance to the anatomical as well as physiological symmetry in the body. It is used to some degree in manual localization and contouring the gross tumor volume (GTV). But it is hard to quantify and therefore hard to use for automatic segmentation.
The development of anatomical atlases for segmentation of different organs [134] [28] makes it possible to locate the same volumes across patients. Hereby it is possible to refer every point inside a single patient to a common atlas. This enables one to make an atlas of the variation of physiological functions such as brain activity[25].
In this study we develop a general framework for segmentation using symmetry properties. The applicability of symmetry for GTV segmentation is inspected. Non-rigid registration is used to quantify symmetry in the head-and-neck (HN) volume for patients without known pathologies. These symmetries are then transferred to a common atlas accounting for the normal variation in this volume. Segmentation of GTV on HN patients is then acquired by comparing their symmetries with the variation in the symmetry atlas. At the same time the symmetry information is used to compare the positron emission tomography (PET) signal across the plane of symmetry for segmentation.

6.3 Theory

In this section the theory behind the new symmetry features is explained. In the first subsection the method to find matching points across a plane of symmetry is outlined. It is described how it is possible to use the non-rigid registration to extract a feature that represents the difference in shrinkage and expansion across the plane of symmetry. The second subsection explains how the symmetry matching can be used with objects with functional properties to extract differences in functional symmetry.

6.3.1 Symmetry

To quantify symmetry for an object we perform the following registration optimization

$$\min_{T} \left(\int_{x} D\left(I\left(x\right), I\left(T\left(x\right) + \tilde{x}\right)\right) + R\left(T\left(x\right)\right) dx \right) \tag{6.1}$$

where D is a given dissimilarity measure function between two images, I is the image, x is the original location in the image, $\tilde{x}$ is the coordinate mirrored through a plane, R is the regularizer. The mirror plane is defined as the set all vectors

$$X = \begin{bmatrix} x_1 \\ x_2 \\ \vdots \\ x_n \end{bmatrix} \tag{6.2}$$

where $A \cdot X^T = p$, A is the unit normal vector of the plane and d is the directional distance from origo to the plane which gives $\tilde{x} = x - 2A(Ax^T - p)$. R is the regularizer keeping the deformation field from invalid expansion/shrinkage and T is the transformed location defined as

$$T(x) = T_R(x) + NR(x) \tag{6.3}$$

where T_R is the rigid transformation to bring the mirrored onto each other and NR is the non-rigid deformation. This deformation actually maps each point on one side of the object to its symmetric point on the other side. The transformation concept is depicted in figure 6.3.1. Achieving the symmetry

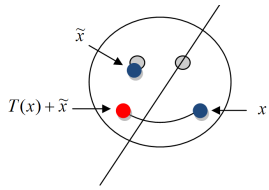

Figure 6.1: Depiction of the symmetry registration principle. A random mirror line is set to illustrate that the method is not dependent on the location and direction of the mirror line.

registration allow one to compute the differences in expansion and shrinkage due to the nonrigid transformation across the symmetric plane. These symmetric volume differences are calculated by

$$\Delta Vol(x) = J(NR(x)) - J(NR(Tx + \tilde{x})) \tag{6.4}$$

where J is the Jacobian, a number below and above 1 signifies respectively a shrinkage or expansion of the region.ΔVol is the symmetric across volume since

$$\Delta Vol(x) = \Delta Vol(Tx + \tilde{x})) \tag{6.5}$$

This does not mean that the integral of $\Delta Vol(x)$ is 0, because of the shrinkage and expansion correspondingly does not have the same volume in an asymmetrical object but $\int_x \Delta Vol(x) \cdot J(NR(x))dx = 0$. Since the method is highly dependent on the initial registration which has local minima it is recommended to place the symmetrical plane in the centroid of the object.
To use $\Delta Vol(x)$ to segment abnormal asymmetric structures it is necessary to find a certain threshold for the segmentation. It is possible to determine normal levels of $\Delta Vol(x)$ if a data set representing the normal variation in the object population is available. Using subjects without the pathology of interest, an atlas containing the symmetry information of the subjects is computed and used as an indicator of normal symmetry.

6.3.2 Functional symmetry

If functional information is available on the object it is also possible to find functional differences across the plane of symmetry. If the object has a functional value, F(x), it is possible to get the symmetrical difference by

$$\Delta F(x) = F(x) - F(Tx + \tilde{x}) \tag{6.6}$$

where ΔF has the same properties as $\Delta Vol(x)$ and $\int_x \Delta F(x) \cdot J(NR(x))dx = 0$.

6.4 Experiments

In this section the experiments performed in this study is explained. The first subsection describes the initial experiments with a simulated object. In the following subsection the patient material is defined. In the third subsection the procedure to build the symmetry atlas is elucidated and in the last subsection the method to use symmetry for tumour segmentation is described.

6.4.1 Simulation

The method was initially tested in a simple way using rigid and non-rigid registration [153]. For the non-rigid registration 3-dimensional b-splines were used

for the deformation field, a sum-of-squares dissimilarity measure was used and an elastic regularizer. The factor of regularization was set as low as possible while still giving positive Jacobians for all deformation fields, i.e. no transformation discrepancies. Non-rigid registration henceforth refers to this approach. A 3-dimensional trigonal trapezohedron was used as object for the symmetric registration. F(x) inside the object was set as two different situations

1. Uniform: Set as the level set value, i.e. the shortest distance to the margin of the object.
2. Asymmetrical: A point source placed in one side of the treapezohedron with decreasing value towards the edge.

The object and its potential can be seen in figure figure 6.2. The mirroring was applied by flipping the image along the axis of asymmetry. Parameters as length of the trapezohedron, signal-to-noise (SNR) level, rotation and regularization was evaluated on a grid of set values to survey the stability of the method.

6.4.2 Patient material

The data set consisted of 55 patients. 30 of those patients had head-and-neck cancer (HNC) located in the hypopharynx treated with radiotherapy at Department of Radiation Oncology, Rigshospitalet, Denmark, these are henceforth denominated segmentation patients. All the segmentation patients had a delineation of the GTV produced by an experienced radiologist and radiation oncologist which was used as a reference for the tumor volume. The remaining 25 patients were cancer patients without involvement in the hypopharynx volume, these patients are henceforth denominated atlas patients. All patients had a x-ray computed tomography (CT) and FDG positron emission tomography scan in head-supine position.

6.4.3 Atlas Construction

Atlas construction is in itself a topic of research [4]. In this study we primarily used the survey results of atlas-based constructions methods [28] and the results from a segmentation challenge for a head-and-neck organ [114] as basis for our framework. The atlas is necessary as a reference for location in a new patient. It is used as a reference of normal symmetry deviations to determine whether the symmetrical expansion is pathologic. The atlas was constructed by picking

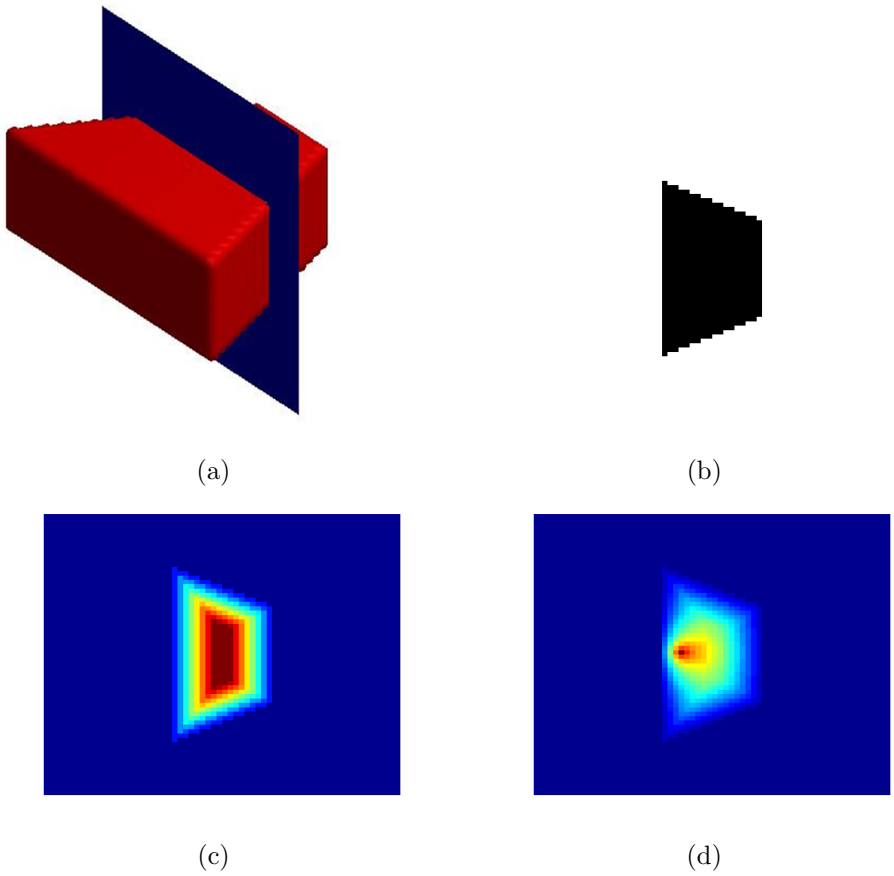

Figure 6.2: Illustration of the simulated trapezohedron. (a) illustrates the trapezohedron in red and the mirror plane in blue. (b) illustrates central slice of the object. (c) illustrates the center slice in the first functional setting with a "uniform" value. (d) illustrates the center slice in the asymmetrical functional setting. In (b-c) the value ranges from 0 to 1.

a random patient as a reference from the atlas patients without tumour in the hypopharynx. The other 24 atlas patients were then registered to the reference using affine and non-rigid registration. After registration an average intensity volume (AIV) was calculated by calculating the average of all the transformed volumes and the initial reference. Afterwards the correlation coefficient between the atlas and the 24 transformed atlas patients was calculated [28]

$$CC = \frac{\sum_x (AIV(x) - \overline{AIV})(I'(x) - \overline{I'})}{\sqrt{\sum_x (AIV(x) - \overline{AIV})^2 \sum_x (I'(x) - \overline{I'})^2}} \tag{6.7}$$

where CC is the correlation coefficient, $AIV(x)$ is the intensity of the AIV at coordinate x, $\overline{AIV}$ is the mean intensity value in the AIV, $I'(x)$ is the intensity value of the transformed patient volume and $\overline{I'}$ is the mean intensity value of the transformed patient volume.
The patient with the lowest correlation coefficient is then chosen as a reference and registration of the other 24 atlas patients to the reference is performed where after a new AIV is created. This process is repeated including all former AIVs until 5 different AIVs are constructed. In this way the AIVs should represent the whole set of patients and not just a randomly chosen subset.

6.4.4 Symmetry registration

Symmetry registration was performed for all patient volume. The procedure consisted of the following steps.

1. Get scan values for mirrored coordinates by flipping the images horizontally.
2. Make a rigid registration between original and mirrored volume achieving the transformation $R(x)$.
3. Make a non-rigid registration between the original and the rigidly transformed mirror volume achieving the transformation $NR(x)$.
4. Compute ΔVol using the symmetric point correspondencies and the $NR(x)$.
5. Find point correspondences between patient volume and the AIVs using affine and non-rigid registration.

All non-rigid registrations were performed using a elastic regularizer at a level found in the similar way as with the atlas construction. The point correspondences between the atlas patients and the AIVs were used to construct 5 symmetry atlases which contained the mean and variance of ΔVol of the atlas patients, denominated respectively $\Delta \bar{V}ol$and $\Delta_\sigma Vol$.

6.4.5 Tumour segmentation

Using symmetric point correspondences it was possible to calculate ΔF from the PET-scans for all the segmentation patients. Receiver operating characteristic (ROC) for tumour segmentation was computed for ΔVol and ΔF using the

manual GTV delineation as a ground truth. Using the point correspondences between the segmentation patients and the AIVs it was possible to compute a probability of normal symmetry

$$P_{sym}(m,x) = \frac{1}{5}\sum_{i=1}^{5} w_i \left(1 - \Phi\left(\frac{\Delta\bar{Vol}(AIV_i,\tilde{x}) - \Delta Vol(m,x)}{\Delta_\sigma Vol(AIV_i,\tilde{x})}\right)\right) \tag{6.8}$$

where P_{sym} is the probability that the symmetry difference is normal, x is the position, m is the patient, w_i is the a weighting relating to AIV number i, $\Phi(y)$ is twice the cumulative probability distribution from 0 to y of a normal distribution with a mean value of 0 and a standard deviation of 1. The value of the probability is signed so that volumes with an increased volume are negative and the opposite are positive. $\Delta\bar{Vol}(AIV_i,\tilde{x})$ is the mean symmetrical expansion/shrinkage at $\tilde{x}$,the coordinate corresponding to x in the AIV and $\Delta_\sigma Vol(AIV_i,\tilde{x})$ is the variance of symmetrical expansion/shrinkage at $\tilde{x}$. w_i is calculated as the correlation between the AIV and patient as

$$w_i = \frac{CC_i}{\sum_{i=1}^{5} CC_i} \tag{6.9}$$

where CC_i is defined as noted in equation 6.7. In this way the probability of the AIVs with the most resemblance to the patient is weighted more. ROC for is computed for Psym and for a combination of P_{sym} and ΔF. For comparison the tumour volumes of the patients were segmented using simple PET-thresholding and The ROC was computed for all patients and then a mean ROC was found along with a mean AUC.

6.5 Results

The symmetry registrations on the simulated of the trapezehedron with varying parameters were successful. An example of the results can be seen in figure 6.5. The method does not accept any non-positive jacobians and therefore some of the transformed trapezohedron is located outside the mirrored periphery in figure 6.5 (a). In figure 6.5 (b) it is seen that the trapezohedron is condensed in the broad edge while it expands halfway between the mirror plane and the narrow edge towards the sides. Figure 6.5 (c) depicts the symmetrical comparison of ΔVol It is seen that the shrinkage and expansion volumes is emphasized.
The results of the experiments showed that the symmetry is susceptible to translation if the mirror plane is placed more than the half the width of the object from the centroid, placing the initial mirrored circumference outside the trapezohedron itself. Rotation of the mirror plane had severe impact if it was more than 40 degrees resulting in a rotation that turned the trapezohedron all the

way around, i.e. a vertical registration. Repeated experiments with varying SNR levels showed that the variation between registration results increased as the SNR ratio decreased. Length of the trapezohedron had impact on the registration results as it either reduced or increased the workload of the method. At `http://www2.imm.dtu.dk/~chrho/symmetryvids` it is possible to see some videos illustrating our results.
The functional symmetry comparison for the uniform case seems to emphasize the regions, with the highest degree of transformation.

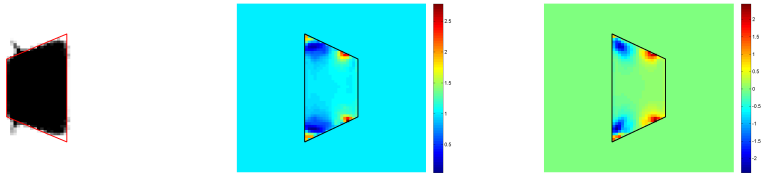

(a) (b) (c)

Figure 6.3: The deformation results of the registration. (a) depicts a slice of the transformed object with the periphery of the trapezohedron depicted in red. (b) illustrates the jacobian of the deformation field, i.e. below 1 shrinkage, above 1 increase in volume. (c) shows the result of the symmetrical difference in volume change. For (b-c) the periphery of the trapezohedron marked in black. The volume lying outside the reference volume is marked with blue circles.

The image, symmetry and deformation atlas was built from the patient without any tumour involvement. An example can be seen in figure 6.5. In (a) it can be seen that the tissue contours are marked less than normal patient images. (b) shows a volume general difference close to the larynx. The difference appeared on all atlases with different magnitude. The image of in (c) shows that the predominant symmetry volume variation appears close to the larynx, to the vertebrae bone and at rear position of the circumference, which arise from differences in shoulder levels on the CT-image slices. The original CT- and PET-image can be seen in respectively (a) and (d) of figure 6.5. The jacobian determinant of the symmetry can be seen in (c). The effect of the shoulder position has the most significant effect. These effects are to a certain degree decreased in P_{sym} due to the comparison with the five atlases. The symmetrical PET function difference,$\Delta F(x)$, is seen in (e). The high function value of the GTV is emphasized while the symmetric spot is marked by a negative signal. The symmetric signal around the larynx is decreased to some degree. In (f) it is possible to see the combination of the P_{sym} and $\Delta F(x)$ used for segmentation.

In figure 6.5 the ROC for the simple PET-thresholding, symmetrical PET, sym-

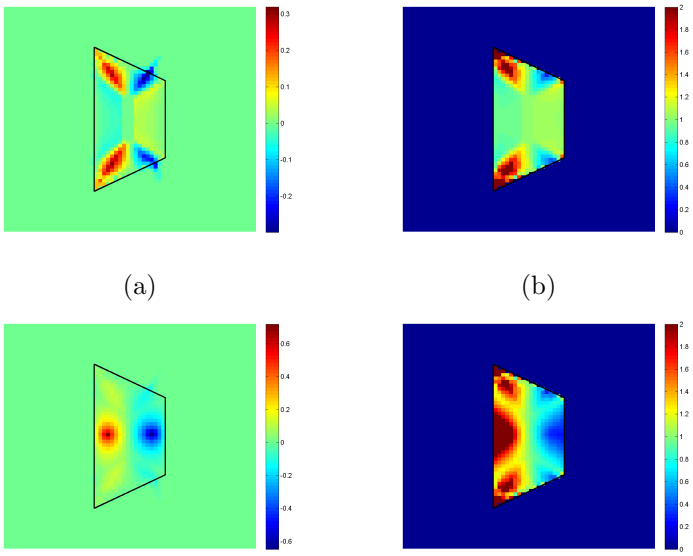

(a) (b)

(c) (d)

Figure 6.4: Symmetrical comparison of functional value. Top row is results from the symmetrical simulations depicted originally in figure 1 (b) and bottom row is from the asymmetrical simulations. Left column is the functional difference results and right column is the ratio results. The circumference of the trapezohedron is represented in black.

metry probability and symmetry combination are seen. It is seen that the symmetrical measures are inferior to the original PET-signal as a classifier. The combination of the two symmetry measures shows an increased sensitivity with a decreased false positive rate. The AUC was 0.89, 0.78, 0.66 and 0.87 for respectively PET-threshold, symmetry probability, PET-symmetry and combination of symmetry measures.

6.6 Discussion

The present study demonstrates that symmetry can be used to segment GTV. To the best of the authors' knowledge it is the first time that it is used for segmentation. The approach is essentially a high dimensional feature extraction using the image in conjuction with prior knowledge from a symmetry atlas. Prior studies have used comparable approaches to quantify asymmetry in sub-

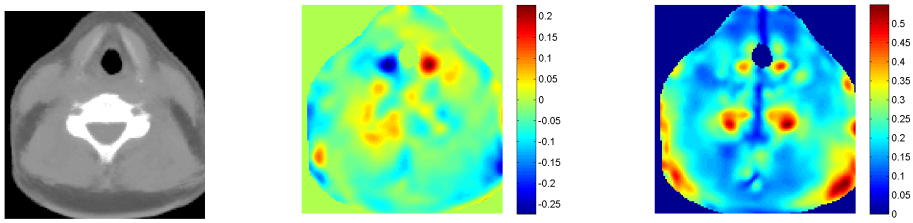

(a) (b) (c)

Figure 6.5: The deformation results of the registration. (a) depicts a slice of the transformed object with the periphery of the trapezohedron depicted in red. (b) illustrates the jacobian of the deformation field, i.e. below 1 shrinkage, above 1 increase in volume. (c) shows the result of the symmetrical difference in volume change. For (b-c) the periphery of the trapezohedron marked in black. The volume lying outside the reference volume is marked with blue circles.

jects with growth changes [106], [41] [37]. But the proposed method differs itself on several levels. First of all, the prior methods focus on surfaces whereas the present method extracts and uses volumetric information. Secondly, prior methods define an axis of symmetry from manually defined points. The present method makes a symmetric transformation but makes no assumption about the actual plane of symmetry. Estimation of the plane of symmetry from the achieved transformation field is possible. But the plane of symmetry arises as a product of a data driven registration and not from manual points. In Figure 4 (c) the plane of symmetry for the atlas can be perceived. This quality makes the present method superior in comparison with automated image segmentation because it does not require any user interaction.
The proposed method delivers results comparable to state-of-the-art automatic methods[130] and manual methods. The earliest developed methods in for head-and-cancer consisted of simple thresholding[145], on PET-images as the one applied as comparison in this study. A further refinement were methods which used an source-to-background assumption derived from phantom measurements[36] [128]. Others use more complex methods as deformable models[102], machine learning[163], Markov random field [63] and fuzzy logic[14] [72] [71]. These methods all use the original CT- or PET-image or they derive features from the image and use these for segmentation. The proposed framework can be combined with any of these methods. It can deliver symmetry features which can be used for segmentation. The approach will have problems with tumours which are symmetric across the plane of symmetry.
The proposed approach takes 2 minutes to derive symmetry information from a CT image of a patient in matrix sizes 512x512x50-100 on a 2.53GHz processor

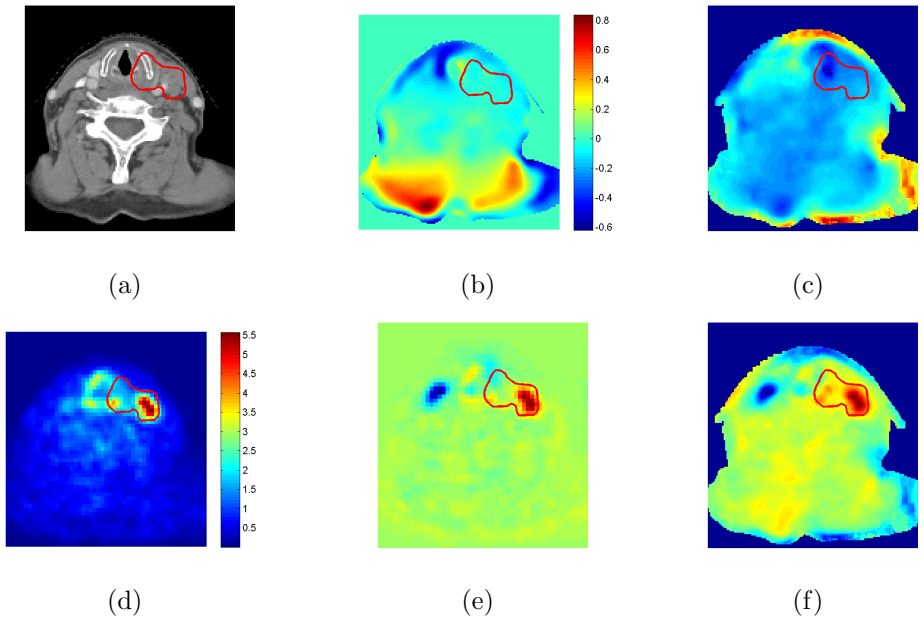

Figure 6.6: Image results from a patient. (a) the original CT-image. (b) Visualization of the symmetry volume difference, . The image intensities has been log2 transformed and the background has been set to 0 to emphasize the result inside the patient. (c) A visualization of the normal symmetry probability, P_{sym}. (d) The original PET-image. (e) The symmetry difference of the PET-image, . (f) the signal of the combination of and used for segmentation. The background has been set to a fixed level in (b-c) and (e-f) to emphasize the signal inside the patient. The red contour is the manual segmentation by the doctors.

with 4 GB of memory. The atlas construction is the most time consuming part of the approach. But once it has been constructed it is possible to derive the symmetry probability within 10 minutes. The registration of the atlas could potentially provide the contours of organs of risk which are also important for radiotherapy planning. The method can also be used for organ function assessment of kidneys, brain and other organs with symmetric distribution in the body. Normal image features from PET images suffer from variability due to scanner, recording and reconstruction methods[51]. An advantage of the symmetry features is that it does not make any assumption about the scanning method and is also compatible with other image modalities. The high sensitivity with low false positive rate is a great advantage of the combined symmetry segmentation compared to thresholding. Since the GTV only occupies a small volume of the head-and-neck volume a false positive rate of 10 % can deliver a

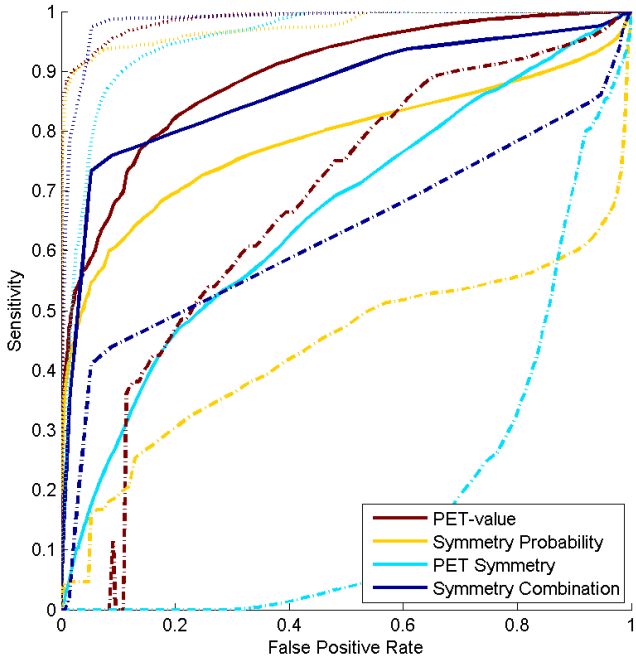

Figure 6.7: The ROC for the four segmentation methods for the 30 patients. The solid line defines the mean ROC for all the patients. The dash-dotted line depicts the minimum sensitivity for all the patiens. The dotted line depicts the maximum sensitivity for all the patients. The horizontal axis represents the rate of false positive or 1-specificity.

false positive volume larger than the actual true positive volume.
The greatest problem with regard to the application of the method is the underlying registration. In this study we kept a conservative procedure to assure the applicability of the method. Settings like transformation, regularizer and masking, can be optimized to deliver better results. But this requires ground truth with some degree of certainty which is better than a manual delineation. If this is not available one risks to develop an approach which could target normal tissue regions.

6.7 Conclusion

A new method for automatic segmentation of GTV using image derived symmetry was developed and tested on 30 patients. The method shows the first uses of symmetry derived features for image segmentation. It provides results which are comparable to the methods applied in current delineation practice.

Lung Tumor Segmentation Using Electric Flow Lines for Graph Cuts

Chapter 7

Lung Tumor Segmentation Using Electric Flow Lines for Graph Cuts

7.1 Abstract

Lung cancer is the most common cause of cancer-related death. A common treatment is radiotherapy where the lung tumors are irradiated with ionizing radiation. The treatment is typically fractionated, i.e. spread out over time, allowing healthy tissue to recover between treatments and allowing tumor cells to be hit in their most sensitive phase. Changes in tumors over the course of treatment allows for an adaptation of the radiotherapy plan based on 3D computer tomography imaging. This paper introduces a method for segmentation of lung tumors on consecutive computed tomography images. These images are normally only used for correction of movements. The method uses graphs based on electric flow lines. The method offers several advantages when trying to replicate manual segmentations. The method gave a dice coefficient of 0.85 and performed better than level set methods and deformable registration.

7.2 Introduction

Treatment response is important in lung cancer treatment. Without treatment response it is impossible to assess the progress or lack of progress of a treatment. With the continued increase of treatment strategies that is available today the possibility of earlier treatment response becomes more and more pertinent. If the patient does not respond adequately to a certain treatment early prediction can spare the patient unnecessary toxic treatment and be used to change treatment strategy. During the last 4 decades 3-dimensional imaging modalities has become one of the most important tools in the clinical assessment of cancer.
Positron emission tomography (PET) has shown to be correlated with treatment outcome [158]. But it is not a conventional tool for early treatment response. Helical Tomotherapy is an external beam radiation therapy system, which has a megavoltage x-ray source making it capable of making megavoltage computerized tomography (MVCT) images. These images are used to provide image guided radiotherapy (IGRT) imaging the target volume to allow adjustment of the patient to optimize treatment. These images potentially includes information about treatment response[132], [20]. But the quantity (up to 30 fractions per patient) of these images makes manual contouring of Gross tumour volume (GTV) unfeasible for clinics.
Several approaches has been developed to segment tumors throughout treatment. Kuhnigk et al [90] developed a method for segmentation of lung lesions and estimation of partial volume effect, Fetita et al.[47] developed a method for lung nodule segmentation and Faggiano et al. [45] developed a registration method to estimate anatomical modification during radiation treatment. Some of these methods are only applicable for kilovoltage computerized tomography (KVCT) images, which are only available for the initial planning scan of these patients. Furthermore, these methods require human interaction for each image sequence.
In this paper we propose a graph based method[160], which uses the principle of electric flow lines (EFL) theory [162], [117] to segment lung tumors on (MVCT) images. The method is novel in regard to utilizing available temporal images of the tumor and makes graphs with unique paths, which are transferable from one fraction to another. Overlap and distance to manual contours are calculated and compared to other automatic methods for segmentation of 3-dimensional images.

7.3 Methodology

We assume an initial pre-treatment scan annotated by manually contouring each slice of the GTV. This will typically be a KVCT scan. At the following treatment sessions a series of scans are then acquired. These will typically be MVCT scans. For each scan in this sequence we want to transfer the GTV outline from the previous scan rigidly to the current scan and to non-rigidly deform this outline to fit to the intensity patterns in the current image. In order to avoid self-intersections we will make this deformation along a graph following EFL derived from simulating an artificial charge at the outline [162], [117] and using a graph cut method to find an optimal tumor outline with respect to smoothness of the outline and correspondence to the underlying image patterns.

7.3.1 Rigid Registration

The rigid registration between scans is performed using correlation as a similarity measure for the volume within 2 cm of the GTV [153]. In the practical application of this method a manual contour was transferred from the KVCT scan to the first MVCT scan. On all following MVCT scans the automatic segmentation was transferred from one scan to the following using the same procedure.

7.3.2 Electric Flow Lines

The initial segmentation from the previous scan is used to generate the EFLs. The electric flow should stem from an electric potential on the surface of the segmentation. The potential, E, is defined as:

$$E(x) = \int Q(\tilde{x})R(\tilde{x} - x)d\tilde{x}, \tag{7.1}$$

where x is the position at which the flow is evaluated and Q is a function which is 1 on the surface and 0 at all other positions. R is the potential at the position x coming from the potential at $\tilde{x}$ defined by Coulombs law as:

$$R(r) = \frac{r}{4\pi\epsilon \cdot ||r||^3}, \tag{7.2}$$

where r is the direction vector from one potential to the point evaluated, ϵ is the electric constant which along with the $4\pi\epsilon$ constant is ignored in practical computations. The surface potential was discretized by performing a Delauney

triangulation of the segmentation points and placing a charge in the barycenter of each triangle. The potential of each triangle was set to its part of the total surface area.
Hereafter an electric line was initiated at each triangle barycenter and iteratively computed in an inwards and outwards direction using the above equations. For the first iteration the potential at the position was neglected because of infinite influence on the potential at the position. Instead an initial step in the direction of the triangle plane normal was used. The image values were extracted along each of the electric flow lines on both the former tumor scan and the current scan on which a segmentation is sought. The correlation between the flow lines from the former and current scan is calculated as a measure of accordance for each position along the EFLs.

7.3.3 Graph Construction

A graph is constructed with vertices, $V_{i,j}$ at each of the positions along the EFL. j corresponds to the individual EFL or columns and i corresponds to each of the positions along it. The graph consists of two types of edges, intra- and inter-column edges. The intra-column edges account for the likelihood that the surface is located at that location. It is formulated as

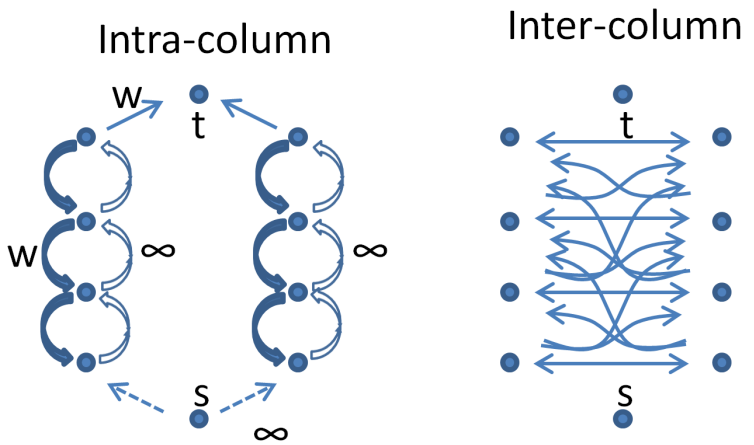

Figure 7.1: Illustration of the edges in the graph. The s and t node are respectively the source and sink. In our implementation there are more layers in each column and there are edges with more than two layer difference.

$$E_{intra}(i \to i-1, j) = \frac{1}{1+e^{c(i)}} \tag{7.3}$$

$$E_{intra}(i \to i+1, j) = \infty \tag{7.4}$$

where $c(i)$ is the correlation value of the ith position along the EFL. A graph consisting only of the intra-column edges would have an optimal solution giving the positions with the highest correlation values. The intercolumn edges are implemented to ensure a smooth segmentation where the segmentation of one EFL is consistent with the surrounding EFLs. The inter-column edges are formulated as

$$E_{inter}(i,k,j,l) = g_{i,k}(j,l), \tag{7.5}$$

$$g_{i,k}(j,l) = \begin{cases} 0 & \text{if } dist(i,k) > 1 \\ 0 & \text{if } i = k \\ 0 & \text{if } j < l \\ w \cdot e^{\frac{-(j-l)}{c}} & \text{else} \end{cases} \tag{7.6}$$

where i and k are line indices referring to EFLs, j and l are position indices on the the EFL and $dist(i,k)$ is the triangulation length between two vertices, which is equal to one when two triangles are interconnected. g is the weighting parameter between EFL, w is the weight constant between EFL and c is a normalization constant. The edges are illustrated in figure 7.1. The specific segmentation solution was found by solving the minimum cut problem on the graph [19].

7.3.4 Graph Parameters

All parameters of the graph were optimised on a spherical phantom with 2 hemispheres and 2 pyramids located on the surface. The phantom had a contour at 0.1 mm from the surface in the image to account for a manual contour not lying exact on the gradient border. The phantom was simulated with a radius variance of 0.2, with different translations, rotations and signal-to-noise levels. A grid search was performed for different parameter settings. The parameters giving the highest dice coefficient were chosen for the actual tumor segmentations.

7.3.5 Evaluating Results

A segmentation for the MVCT scans was extracted using each of the two initial manual scans from the planning KVCT scan resulting in 6 new automatic segmentations for each patient. To evaluate the segmentation results the new

segmentations were compared with both of the manual segmentations on the MVCT scans using dice coefficient, Hausdorff distance and mean distance. The images were also segmented using a level set method [87] and deformable registration [153] for comparison. A paired t-test was performed to assess significant difference from the novel method on a basis of 0.05.

7.4 Results

7.4.1 Experiment Data

The study included images from ten NSCLC patients, 3 female and 7 males, chosen from a larger patient group from a dose escalation study [3]. The patients were treated between 2004 and 2009 at University of Wisconsin Hospital. They were all treated with radiotherapy delivered via helical tomotherapy. All patients were non-metastatic at stage IIIa, IIIb or recurrent histologically confirmed NSCLC with no prior thoracic radiation therapy. The patient selection criteria were a cranio-caudal length of less than 5 cm for the primary tumor the planning CT.

Primary planning KVCT scan images for all patients was exported along with the images of three MVCT scans from the Tomotherapy system from first, mid and last fraction (1, 13 and 25). The time span between planning KVCT and last fraction was between 34 and 41 days. The images were imported into Pinnacle© treatment planning system. If the MVCT image did not include the primary tumor, images from bordering fractions were chosen instead.

All MVCT images were manually registered to the KVCT image using Pinnacle© to replicate the usual clinical procedure. Primary GTV was contoured independently by two experienced radiation oncologists on all patient images, 10 patients times 4 images. Provided along with the images were contours of normal tissue from the original treatment planning on the KVCT images. This means that in all 40 images were provided with 2 contours on each image. The contours and images are exported from Pinnacle© as Dicoms and imported to Matlab© using CERR [40] where further processing was performed.

7.4.2 Experiment Results

It was possible to segment the tumor for all the patients on all of their images. Result examples for the novel segmentation can be seen in Fig. 7.2. The results

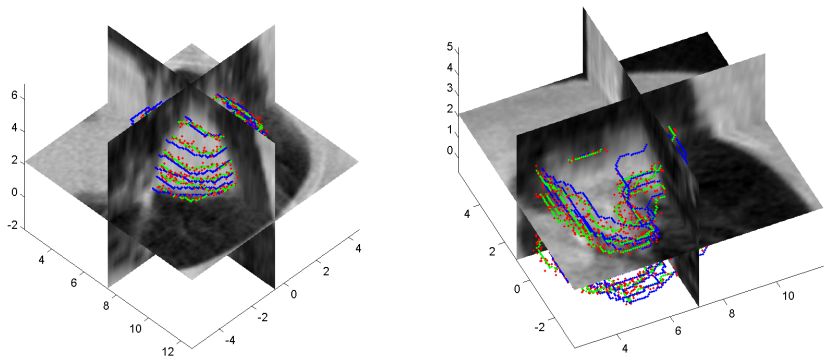

Figure 7.2: Examples of the segmentation on a MVCT image. Green and blue points are the two different manual segmentations. The red point are the automatic segmentation of the novel method.

Table 7.1: The results of the different methods of segmentation. Seg. type: Segmentation type. Haus. Dis.: Hausdorff distance. Mean Dis.: Hausdorff distance. EFL: Electric flow line segmentation. Deformable: Deformable registration. $\star$ The manual segmentations are only compared pairwise to each other, whereas the automatic segmentation are compared to both of the manual segmentations.

Seg. Type	Dice	Haus. Dis.	Mean Dis.
Manual $\star$	0.78± 0.13	0.8± 0.7	0.24 ± 0.10
EFL	0.85 ± 0.11	0.7± 0.5	0.15 ± 0.05
Level set	0.67± 0.22	0.9± 0.6	0.29 ± 0.09
Deformable	0.73± 0.20	0.8± 0.7	0.22 ± 0.08

are seen in Table 7.1. The novel method had significant better dice coefficient and mean difference than the two other methods using a paired t-test of 0.05 but not for Hausdorff distance. Looking at the volume as a treatment outcome the manual segmentations had a mean variation of 7.1 % on the KVCT images and 8.5 % on the MVCT images. The novel method had a mean variation of 4.5 % for the volume on the MVCT images.

7.5 Discussion

The method of parameter optimization should be mentioned as a first point of scrutiny. It is solely performed on a simulated phantom. The phantom is

constructed ideally with normally distributed noise, rotations and translation of the whole phantom. The tumor image sequences have none of these characteristics. But even so it represented an acceptable method for finding segmentation parameters for the tumor segmentation. It would also be possible to find parameters by using manual segmentations on tumor images. But this would just find parameters to replicate one manual contourer. In this approach we created the phantom to have qualities which would suit a manual contourer generally.

It can be seen from table 7.1 that the novel method performs better compared to the other automatic methods here. The novel method performs better than the level set method and deformable registration. The level set method only includes image values and their gradients in its cost function. This can be a problem when attempting to repeat manual segmentations automatically, because the manual segmentations do not necessarily follow image gradients. The same thing also applies for deformable registration. Even though the cost function was based on normalized correlation, it does still have larger problems with circumference of its segmentation.

Segmentations of lung tumors have smaller variations than other tumor sites [137] it is still a hard tumor site because of movement of lungs and heart. These problems have been reduced by 4D-visualization and breath hold techniques but it is still a significant problem for automatic segmentation methods. The quality of MVCT does also increase the variation for manual contours as it can be seen on the difference in volume variation between KVCT and MVCT. One could apply better imaging techniques for these interfractional images to acquire a better outcome for the automatic segmentation methods. But this is not feasible in the current clinical setup. These images are taken to adjust beam and patient position but are not analyzed. This is both due to the amount of images and the lack of resources in the clinic.

The automatic contours are compared to manual segmentations in lack of better segmentations. An optimal comparison would be to the actual tumor volumes. This is feasible in some tumor sites but it is not feasible in treatments with several fraction.

The novel method does have some shortcomings. It does expect some continuation of topology which for our images is optimal, because these tumors tend to retain most of their topology throughout treatment. If the tumors were dividing into several volume components it would pose as a suboptimal solution.

7.6 Conclusion

A novel method for 3-dimensional segmentation of consecutive images have been implemented and have been shown to perform better than level set methods and deformable registration concerning overlap. The method is applicable on clinical images without any modification of clinical practice.

Appendix A

Further Contributions

A.1 Journal Articles

- Paulina E. Galavis, Christian Hollensen, Ngoneh Jallow, Bhudatt Paliwal, and Robert Jeraj. Variability of textural features in fdg pet images due to different acquisition modes and reconstruction parameters. *Acta Oncologica*, 49(7):1012-1016, 2010.

- Gitte Fredberg Persson, Ditte Eklund Nygaard, Anders Peter Roed, Christian Hollensen, Lene Sonne, Anne Kirkebjerg Due, Anne Kiil Berthelsen, Jan Nyman, Elena Markova, Henrik Roed, Per Munck af Rosenschöld, Stine Korreman, and Lena Specht. Inter-observer delineation uncertainty in radiotherapy of peripheral lung tumours. *British Journal of Radiology*, 85(1017), 654-660.

- Eva Serup-Hansen, Helle Westergren Hendel, Helle Hjorth Johannesen, Wiviann Ottosson, Brian Kristensen, Christian Hollensen, Gitte Fredberg Persson, Poul Flemming Geertsen, and Hanne Havsteen. Volumetric and spatial variations in target volume delineations using ct, mri and fdg-pet in planning radiotherapy of anal cancer . *International Journal of Radiation: Oncology - Biology - Physics.*(submitted)

A.2 Conference Abstracts

- Christian Hollensen, George Cannon, Liselotte Højgaard, Lena Specht, Rasmus Larsen, and Søren Bentzen. Temporal volume of lung tumor during treatment with tomotherapy. *International Journal of Radiation: Oncology - Biology - Physics -ASTRO supplement*, 81(2):S797-S798, 2011.

- Christian Hollensen, Peter Stanley Jørgensen, Liselotte Højgaard, Lena Specht, and Rasmus Larsen. Auto-segmentation of head and neck cancer using textural features. *Radiotherapy & Oncology - ESTRO supplement*, 2010.(Accepted for oral presentation)

- Christian Hollensen, Gitte Fredberg Persson, Liselotte Højgaard, and Lena Specht. Does the progress in radiotherapy make higher demand to inter-observer variability correction? a case study of imrt and volumetric arc therapy. *International Journal of Radiation: Oncology - Biology - Physics -ASTRO supplement* (Accepted for oral presentation)

- Christian Hollensen, Gitte Fredberg Persson, Liselotte Højgaard, and Lena Specht. Geometrical comparison measures for tumor delineation, what do they mean for the actual dosis plan? *Radiotherapy & Oncology - ESTRO supplement*, 2012.

- Eva Serup-Hansen, Helle Westergren Hendel, Helle Hjorth Johannesen, Wiviann Ottosson, Christian Hollensen, Gitte Fredberg Persson, Poul F. Geertsen, and Hanne Havsteen. Variation in gross tumor volume delineation using ct, mri, and fdg-pet in planning radiotherapy of anal cancer. *Journal Clinical Oncology*, 30(S4):652, 2012.

Bibliography

[1] *Global status report on noncommunicable diseases 2010.* World Health Organization, 2011.

[2] AAPM. American association of physicists in medicine, task group no. 211 - classification, advantages and limitations of the auto-segmentation approaches for pet,. Internet webpage, July 2012.

[3] J. B. Adkison, D. Khuntia, S. M. Bentzen, G. M. Cannon, W. A. Tome, H. Jaradat, W. Walker, A. M. Traynor, T. Weigel, and M. P. Mehta. Dose escalated, hypofractionated radiotherapy using helical tomotherapy for inoperable non-small cell lung cancer: preliminary results of a risk-stratified phase I dose escalation study. *Technology in Cancer Research Treatment*, 7(6):441–447, 2008.

[4] P. Aljabar, R. A. Heckemann, A. Hammers, J. V. Hajnal, and D. Rueckert. Multi-atlas based segmentation of brain images: atlas selection and its effect on accuracy. *Neuroimage*, 46(3):726–738, Jul 2009.

[5] Moses Amadasum and Robert King. Textural features corresponding to textural properties. *IEEE Transactions on systems, man and cybernetics*, 19(5):1989, Sep 1989.

[6] Amit. A nonlinear variational problem for image matching. *SIAM J. Sci. Comput. (USA)*, 15(1):207–224, 1994.

[7] A.H. Andersen. Algebraic reconstruction in ct from limited views. *Medical Imaging, IEEE Transactions on*, 8(1):50–55, 1989.

[8] J. A. Antolak and I. I. Rosen. Planning target volumes for radiotherapy: how much margin is needed? *Int J Radiat Oncol Biol Phys*, 44(5):1165–1170, Jul 1999.

[9] Arad and Reisfeld. Image warping using few anchor points and radial functions. *Comput. Graph. Forum (UK)*, 14(1):35–46, 1995.

[10] K. Babalola and T. Cootes. Aam segmentation of the mandible and brainstem. 08 2009.

[11] Bajcsy and Kovacic. Multiresolution elastic matching. *Comput. Vis. Graph. Image Process. (USA)*, 46(1):1–21, 1989.

[12] Simon Baker and Iain Matthews. Lucas-kanade 20 years on: A unifying framework. *International Journal of Computer Vision*, 56(3):221–255, 2004.

[13] A. Bel, M. van Herk, and J. V. Lebesque. Target margins for random geometrical treatment uncertainties in conformal radiotherapy. *Med Phys*, 23(9):1537–1545, Sep 1996.

[14] Saoussen Belhassen and Habib Zaidi. A novel fuzzy c-means algorithm for unsupervised heterogeneous tumor quantification in pet. *Med Phys*, 37(3):1309–1324, Mar 2010.

[15] Søren M Bentzen. Radiation therapy: intensity modulated, image guided, biologically optimized and evidence based. *Radiother Oncol*, 77(3):227–230, Dec 2005.

[16] Søren M Bentzen. Preventing or reducing late side effects of radiation therapy: radiobiology meets molecular pathology. *Nat Rev Cancer*, 6(9):702–713, Sep 2006.

[17] Judit Boda-Heggemann, Frank Lohr, Frederik Wenz, Michael Flentje, and Matthias Guckenberger. kv cone-beam ct-based igrt: a clinical review. *Strahlenther Onkol*, 187(5):284–291, May 2011.

[18] Ronald Boellaard, Wim J G Oyen, Corneline J Hoekstra, Otto S Hoekstra, Eric P Visser, Antoon T Willemsen, Bertjan Arends, Fred J Verzijlbergen, Josee Zijlstra, Anne M Paans, Emile F I Comans, and Jan Pruim. The netherlands protocol for standardisation and quantification of fdg whole body pet studies in multi-centre trials. *Eur J Nucl Med Mol Imaging*, 35(12):2320–2333, Dec 2008.

[19] Yuri Boykov, Olga Veksler, and Ramin Zabih. Markov random fields with efficient approximations. *IEEE Computer Society Conference on Computer Vision Pattern Recognition Proceedings*, pages 648–655, 1998.

[20] S. Bral, M. D. Ridder, M. Duchateau, T. Gevaert, B. Engels, D. Schallier, and G. Storme. Daily megavoltage computed tomography in lung cancer radiotherapy: correlation between volumetric changes and local outcome. *International Journal of Radiation Oncology Biology Physics*, 80(5):1338–1342, August 2011.

[21] Freddie Bray, Ahmedin Jemal, Nathan Grey, Jacques Ferlay, and David Forman. Global cancer transitions according to the human development index (2008-2030): a population-based study. *Lancet Oncol*, Jun 2012.

[22] Stephen L Breen, Julia Publicover, Shiroma De Silva, Greg Pond, Kristy Brock, Brian O'Sullivan, Bernard Cummings, Laura Dawson, Anne Keller, John Kim, Jolie Ringash, Eugene Yu, Aaron Hendler, and John Waldron. Intraobserver and interobserver variability in gtv delineation on fdg-pet-ct images of head and neck cancers. *Int J Radiat Oncol Biol Phys*, 68(3):763–770, Jul 2007.

[23] M. Bro-Nielsen and C. Gramkow. Fast fluid registration of medical images. *LECTURE NOTES IN COMPUTER SCIENCE*, (1131):267–276, 1996.

[24] C. Burman, G. J. Kutcher, B. Emami, and M. Goitein. Fitting of normal tissue tolerance data to an analytic function. *Int J Radiat Oncol Biol Phys*, 21(1):123–135, May 1991.

[25] Cindy Casteels, Peter Vermaelen, Johan Nuyts, Annemie Van Der Linden, Veerle Baekelandt, Luc Mortelmans, Guy Bormans, and Koen Van Laere. Construction and evaluation of multitracer small-animal pet probabilistic atlases for voxel-based functional mapping of the rat brain. *J Nucl Med*, 47(11):1858–1866, Nov 2006.

[26] K. S. Chao, W. R. Bosch, S. Mutic, J. S. Lewis, F. Dehdashti, M. A. Mintun, J. F. Dempsey, C. A. Perez, J. A. Purdy, and M. J. Welch. A novel approach to overcome hypoxic tumor resistance: Cu-atsm-guided intensity-modulated radiation therapy. *Int J Radiat Oncol Biol Phys*, 49(4):1171–1182, Mar 2001.

[27] K. S Clifford Chao, Shreerang Bhide, Hansen Chen, Joshua Asper, Steven Bush, Gregg Franklin, Vivek Kavadi, Vichaivood Liengswangwong, William Gordon, Adam Raben, Jon Strasser, Christopher Koprowski, Steven Frank, Gregory Chronowski, Anesa Ahamad, Robert Malyapa, Lifei Zhang, and Lei Dong. Reduce in variation and improve efficiency of target volume delineation by a computer-assisted system using a deformable image registration approach. *Int J Radiat Oncol Biol Phys*, 68(5):1512–1521, Aug 2007.

[28] A. Chen, K. J. Niermann, M. A. Deeley, and B. M. Dawant. Evaluation of multiple-atlas-based strategies for segmentation of the thyroid gland in head and neck ct images for imrt. *Phys Med Biol*, 57(1):93–111, Jan 2012.

[29] Antong Chen, Matthew A Deeley, Kenneth J Niermann, Luigi Moretti, and Benoit M Dawant. Combining registration and active shape models for the automatic segmentation of the lymph node regions in head and neck ct images. *Med Phys*, 37(12):6338–6346, Dec 2010.

[30] Christensen and Johnson. Consistent image registration. *IEEE Trans. Med. Imaging*, 20(7):568–582, 2001.

[31] Gary E. Christensen and Hans J. Johnson. Invertibility and transitivity analysis for nonrigid image registration. *Journal of electronic imaging*, 12(1):106–117, 2003.

[32] Collins, Zijdenbos, Kollokian, Sled, Kabani, Holmes, and Evans. Design and construction of a realistic digital brain phantom. *IEEE Trans. Med. Imaging*, 17(3):463–468, 1998.

[33] Olivier Commowick, Vincent Grégoire, and Grégoire Malandain. Atlas-based delineation of lymph node levels in head and neck computed tomography images. *Radiother Oncol*, 87(2):281–289, May 2008.

[34] Renzo Corvò. Evidence-based radiation oncology in head and neck squamous cell carcinoma. *Radiother Oncol*, 85(1):156–170, Oct 2007.

[35] Jean-François Daisne, Thierry Duprez, Birgit Weynand, Max Lonneux, Marc Hamoir, Hervé Reychler, and Vincent Grégoire. Tumor volume in pharyngolaryngeal squamous cell carcinoma: comparison at ct, mr imaging, and fdg pet and validation with surgical specimen. *Radiology*, 233(1):93–100, Oct 2004.

[36] Jean-François Daisne, Mérence Sibomana, Anne Bol, Thomas Doumont, Max Lonneux, and Vincent Grégoire. Tri-dimensional automatic segmentation of pet volumes based on measured source-to-background ratios: influence of reconstruction algorithms. *Radiother Oncol*, 69(3):247–250, Dec 2003.

[37] T.A. Darvann, N.V. Hermann, S. Demant, P. Larsen, H. Olafsdottir, S.S. Thorup, M. Zak, A.B. Lipira, A.A. Kane, D. Govier, H. Schatz, D. Rueckert, and S. Kreiborg. Automated quantification and analysis of facial asymmetry in children with arthritis in the temporomandibular joint. In *Biomedical Imaging: From Nano to Macro, 2011 IEEE International Symposium on*, pages 1193 –1196, 30 2011-april 2 2011.

[38] F De la Torre and MJ Black. Robust parameterized component analysis - theory and applications to 2d facial modeling. *LECT N COMP LECT NOTES COMPUT SC LECT NOTE COMPUT SCI Lecture notes in computer science*, 2353:653–669, 2002.

[39] J. Deacon, M. J. Peckham, and G. G. Steel. The radioresponsiveness of human tumours and the initial slope of the cell survival curve. *Radiother Oncol*, 2(4):317–323, Dec 1984.

[40] Joseph O Deasy, Angel I Blanco, and Vanessa H Clark. CERR: a computational environment for radiotherapy research. *Medical Physics*, 30(5):979–985, 2003.

[41] Sune Demant, Nuno V Hermann, Tron A Darvann, Marek Zak, Helena Schatz, Per Larsen, and Sven Kreiborg. 3d analysis of facial asymmetry in subjects with juvenile idiopathic arthritis. *Rheumatology (Oxford)*, 50(3):586–592, Mar 2011.

[42] R. E. Drzymala, R. Mohan, L. Brewster, J. Chu, M. Goitein, W. Harms, and M. Urie. Dose-volume histograms. *Int J Radiat Oncol Biol Phys*, 21(1):71–78, May 1991.

[43] M. Engelsman, E. M. Damen, K. De Jaeger, K. M. van Ingen, and B. J. Mijnheer. The effect of breathing and set-up errors on the cumulative dose to a lung tumor. *Radiother Oncol*, 60(1):95–105, Jul 2001.

[44] M. Engelsman, P. Remeijer, M. van Herk, J. V. Lebesque, B. J. Mijnheer, and E. M. Damen. Field size reduction enables iso-ntcp escalation of tumor control probability for irradiation of lung tumors. *Int J Radiat Oncol Biol Phys*, 51(5):1290–1298, Dec 2001.

[45] E. Faggiano, G. M. Cattaneo, C. Ciavarro, I. Dell'Oca, D. Persano, R. Calandrino, and G. Rizzo. Validation of an elastic registration technique to estimate anatomical lung modification in non-small-cell lung cancer tomotherapy. *Radiation Oncology*, 6:31, 2011.

[46] LA Feldkamp, LC Davis, and JW Kress. Practical cone-beam algorithm. *JOSA A*, 1(6):612–619, 1984.

[47] C. I. Fetita, Françoise F. Prêteux, C. Beigelman-Aubry, and P. Grenier. 3d automated lung nodule segmentation in hrct. *LNCS*, 2879:626–634, 2003.

[48] Barbara Fischer, Ulrik Lassen, Jann Mortensen, Søren Larsen, Annika Loft, Anne Bertelsen, Jesper Ravn, Paul Clementsen, Asbjørn Høgholm, Klaus Larsen, Torben Rasmussen, Susanne Keiding, Asger Dirksen, Oke Gerke, Birgit Skov, Ida Steffensen, Hanne Hansen, Peter Vilmann, Grete Jacobsen, Vibeke Backer, Niels Maltbaek, Jesper Pedersen, Henrik Madsen, Henrik Nielsen, and Liselotte Højgaard. Preoperative staging of lung cancer with combined pet-ct. *N Engl J Med*, 361(1):32–39, Jul 2009.

[49] M. Fornefett, K. Rohr, and H. S. Stiehl. Elastic registration of medical images using radial basis functions with compact support. *IEEE Conference on Computer Vision & Pattern Recognition (CVPR)*, 2:402–409, 1999.

[50] Y. Freund and R. Schapire. A desicion-theoretic generalization of on-line learning and an application to boosting. In *Computational learning theory*, pages 23–37. Springer, 1995.

[51] Paulina E Galavis, Christian Hollensen, Ngoneh Jallow, Bhudatt Paliwal, and Robert Jeraj. Variability of textural features in fdg pet images due to different acquisition modes and reconstruction parameters. *Acta Oncol*, 49(7):1012–1016, Oct 2010.

[52] M Garcia, A Jemal, EM Ward, MM Center, Y Hao, RL Siegel, and MJ Thun. Global cancer facts & figures 2007. Technical report, Atlanta, GA: American Cancer Society, 2007.

[53] Xavier Geets, Jean-Francois Daisne, Vincent Gregoire, Marc Hamoir, and Max Lonneux. Role of 11-c-methionine positron emission tomography for the delineation of the tumor volume in pharyngo-laryngeal squamous cell carcinoma: comparison with fdg-pet and ct. *Radiother Oncol*, 71(3):267–273, Jun 2004.

[54] Xavier Geets, John A Lee, Anne Bol, Max Lonneux, and Vincent Grégoire. A gradient-based method for segmenting fdg-pet images: methodology and validation. *Eur J Nucl Med Mol Imaging*, 34(9):1427–1438, Sep 2007.

[55] David Gering and Ben Kalinosky. Automatic segmentation of the parotid glands by situated bayesian classification. *Workshop Proceedings from the 13th International Conference on Medical Image Computingand Computer Assisted Intervention, Medical Image Analysis for the Clinic: A Grand Challenge*, pages 289–296, 2010.

[56] C Goodall. Procrustes methods in the statistical-analysis of shape. *J. R. Stat. Soc. Ser. B-Methodol. J ROY STA B J ROY STAT SOC B MET J ROY STATIST SOC SER B METHO*, 53(2):285–339, 1991.

[57] S. Gorthi, V. Duay, M. Bach Cuadra, P. Tercier, A. Allal, and J. Thiran. Active contour-based segmentation of head and neck with adaptive atlas selection. 09 2009.

[58] Subrahmanyam Gorthi, Meritxell Bach Cuadra, Ulrike Schick, Pierre-Alain Tercier, Abdelkarim S. Allal, , and Jean-Philippe Thiran. Multi-atlas based segmentation of head and neck ct images using active contour framework. *Workshop Proceedings from the 13th International Conference*

on Medical Image Computingand Computer Assisted Intervention, Medical Image Analysis for the Clinic: A Grand Challenge, pages 313–322, 2010.

[59] Ardeshir Goshtasby. Image registration by local approximation methods. *Image and Vision Computing*, 6(4):255–261, 1988.

[60] J. C. Gower. Generalized procrustes analysis. *Psychometrika*, 40(1):33–51, 1975.

[61] Carlo Greco, Sadek A Nehmeh, Heiko Schöder, Mithat Gönen, Barbara Raphael, Hilda E Stambuk, John L Humm, Steven M Larson, and Nancy Y Lee. Evaluation of different methods of 18f-fdg-pet target volume delineation in the radiotherapy of head and neck cancer. *Am J Clin Oncol*, 31(5):439–445, Oct 2008.

[62] Vincent Grégoire, Avraham Eisbruch, Marc Hamoir, and Peter Levendag. Proposal for the delineation of the nodal ctv in the node-positive and the post-operative neck. *Radiother Oncol*, 79(1):15–20, Apr 2006.

[63] Dongfeng Han, John Bayouth, Qi Song, Aakant Taurani, Milan Sonka, John Buatti, and Xiaodong Wu. Globally optimal tumor segmentation in pet-ct images: a graph-based co-segmentation method. *Inf Process Med Imaging*, 22:245–256, 2011.

[64] X. Han, L. Hibbard, N. O'Connell, and V. Willcut. Automatic segmentation of head and neck ct images by gpu-accelerated multi-atlas fusion. 08 2009.

[65] Xiao Han, Lyndon S. Hibbard, Nicolette P. OConnell, , and Virgil Willcut. Automatic segmentation of parotids in head and neck ct images using multiatlas fusion. *Workshop Proceedings from the 13th International Conference on Medical Image Computingand Computer Assisted Intervention, Medical Image Analysis for the Clinic: A Grand Challenge*, pages 297–304, 2010.

[66] Xiao Han, Mischa S Hoogeman, Peter C Levendag, Lyndon S Hibbard, David N Teguh, Peter Voet, Andrew C Cowen, and Theresa K Wolf. Atlas-based auto-segmentation of head and neck ct images. *Med Image Comput Comput Assist Interv Int Conf Med Image Comput Comput Assist Interv*, 11(Pt 2):434–441, 2008.

[67] G. G. Hanna, A. R. Hounsell, and J. M. O'Sullivan. Geometrical analysis of radiotherapy target volume delineation: a systematic review of reported comparison methods. *Clin Oncol (R Coll Radiol)*, 22(7):515–525, Sep 2010.

[68] Mads Fogtmann Hansen. *The Virtual Knife*. PhD thesis, Technical University of Denmark, 2009.

[69] Robert M. Haralick, K. Shanmugam, and Its'hak Dinstein. Textural features for image classification. *IEEE Transactions on systems, man and cybernetics*, SMC-3(6):610–621, Nov 1973.

[70] M. Hatt, F. Lamare, N. Boussion, A. Turzo, C. Collet, F. Salzenstein, C. Roux, P. Jarritt, K. Carson, C. Cheze-Le Rest, and D. Visvikis. Fuzzy hidden markov chains segmentation for volume determination and quantitation in pet. *Phys Med Biol*, 52(12):3467–3491, Jun 2007.

[71] Mathieu Hatt, Catherine Cheze le Rest, Patrice Descourt, André Dekker, Dirk De Ruysscher, Michel Oellers, Philippe Lambin, Olivier Pradier, and Dimitris Visvikis. Accurate automatic delineation of heterogeneous functional volumes in positron emission tomography for oncology applications. *Int J Radiat Oncol Biol Phys*, 77(1):301–308, May 2010.

[72] Mathieu Hatt, Catherine Cheze le Rest, Alexandre Turzo, Christian Roux, and Dimitris Visvikis. A fuzzy locally adaptive bayesian segmentation approach for volume determination in pet. *IEEE Trans Med Imaging*, 28(6):881–893, Jun 2009.

[73] Tobias Heimann and Hans-Peter Meinzer. Statistical shape models for 3d medical image segmentation: A review. *Medical Image Analysis*, 13(4):543–563, 2009.

[74] Liselotte Højgaard and Lena Specht. Pet/ct in head and neck cancer. *Eur J Nucl Med Mol Imaging*, 34(9):1329–1333, Sep 2007.

[75] T.K. Ho. Random decision forests. In *Document Analysis and Recognition, 1995., Proceedings of the Third International Conference on*, volume 1, pages 278–282. IEEE, 1995.

[76] Christian Hollensen, Mads Fogtmann Hansen, Liselotte Højgaard, Lena Specht, and Rasmus Larsen. Segmenting the parotid gland using registration and level set methods. *Workshop Proceedings from the 13th International Conference on Medical Image Computingand Computer Assisted Intervention, Medical Image Analysis for the Clinic: A Grand Challenge*, pages 305–312, 2010.

[77] Christian Hollensen, Peter Stanley Jørgensen, Liselotte Højgaard, Lena Specht, and Rasmus Larsen. Auto-segmentation of head and neck cancer using textural features. *Radiotherapy & Oncology - ESTRO supplement*, 2010.

[78] Christian Hollensen, Gitte Fredberg Persson, Liselotte Højgaard, and Lena Specht. Geometrical comparison measures for tumor delineation, what do they mean for the actual dosis plan? *Radiotherapy & Oncology - ESTRO supplement*, 2012.

[79] T.S. Hong, W.A. Tome, R.J. Chappell, and P.M. Harari. Variations in target delineation for head and neck imrt: An international multi-institutional study. *Int J Radiat Oncol Biol Phys*, 60(1, Supplement):S157 – S158, 2004.

[80] Yoav Horn. Diffusion of technical change in medicine - a case study on oncology in traditional society. *Technol Forecast Soc Change Technological forecasting & social change*, 28(3):175–180, 1985.

[81] H.M. Hudson and R.S. Larkin. Accelerated image reconstruction using ordered subsets of projection data. *Medical Imaging, IEEE Transactions on*, 13(4):601–609, 1994.

[82] International Commission on Radiation Units ICRU and Measurements. Prescribing, recording and reporting electron beam therapy,. *ICRU Report*, 4(71):25–37, 2004.

[83] International Commission on Radiation Units ICRU and Measurements. Prescribing, recording and reporting intensity-modulated photon-beam therapy (imrt). *ICRU Report*, 10(83):41–53, 2010.

[84] David A Jaffray, Jeffrey H Siewerdsen, John W Wong, and Alvaro A Martinez. Flat-panel cone-beam computed tomography for image-guided radiation therapy. *Int J Radiat Oncol Biol Phys*, 53(5):1337–1349, Aug 2002.

[85] Wendy Jeanneret-Sozzi, Raphaël Moeckli, Jean-François Valley, Abderrahim Zouhair, Esat Mahmut Ozsahin, René-Olivier Mirimanoff, and S. A. S. R. O. The reasons for discrepancies in target volume delineation : a sasro study on head-and-neck and prostate cancers. *Strahlenther Onkol*, 182(8):450–457, Aug 2006.

[86] Ahmedin Jemal, Freddie Bray, Melissa M Center, Jacques Ferlay, Elizabeth Ward, and David Forman. Global cancer statistics. *CA Cancer J Clin*, 61(2):69–90, 2011.

[87] P.S. Jørgensen, K.V. Hansen, R. Larsen, and J.R. Bowen. A framework for automatic segmentation in three dimensions of microstructural tomography data. *Ultramicroscopy*, 110(3):216–228, February 2010.

[88] D. Kainmueller, H. Lamecker, H. Seim, and S. Zachow. Multi-object segmentation of head bones. 09 2009.

[89] Kikinis, Shenton, Iosifescu, McCarley, Saiviroonporn, Hokama, Robatino, Metcalf, Wible, Portas, Donnino, and Jolesz. A digital brain atlas for surgical planning, model-driven segmentation, and teaching. *IEEE Trans. Visual. Comput. Graphics*, 2(3):232–241, 1996.

[90] J. M. Kuhnigk, V. Dicken, L. Bornemann, A. Bakai, D. Wormanns, S. Krass, and H.-O. Peitgen. Morphological segmentation and partial volume analysis for volumetry of solid pulmonary lesions in thoracic ct scans. *IEEE Trans. Medical Imaging*, 25(4):417–434, 2006.

[91] Jan Kybic, Philippe Thevenaz, and Michael Unser. Multiresolution spline warping for epi registration. *Proc SPIE Int Soc Opt Eng*, 3813:571–579, 1999.

[92] M. La Macchia, F. Fellin, M. Amichetti, M. Cianchetti, P. Vitali, S. Gianolini, T. Lomax, and L. Widesott. Po-0789 evaluation of three commercial software solutions for automatic segmentation for redelineation of target and oars, May 2012.

[93] John A Lee. Segmentation of positron emission tomography images: some recommendations for target delineation in radiation oncology. *Radiother Oncol*, 96(3):302–307, Sep 2010.

[94] Christian Wittekind Leslie H. Sobin, Mary K. Gospodarowicz. *TNM Classification of Malignant Tumours*. Wiley, 2009.

[95] Hua Li, Wade L Thorstad, Kenneth J Biehl, Richard Laforest, Yi Su, Kooresh I Shoghi, Eric D Donnelly, Daniel A Low, and Wei Lu. A novel pet tumor delineation method based on adaptive region-growing and dual-front active contours. *Med Phys*, 35(8):3711–3721, Aug 2008.

[96] Stan Z. Li. *Markov Random Field Modeling in Image Analysis*. Springer, 2009.

[97] Sören Mattsson and Marcus Söderberg. Radiation dose management in ct, spect/ct and pet/ct techniques. *Radiat Prot Dosimetry*, 147(1-2):13–21, Sep 2011.

[98] A. L. McKenzie. How should breathing motion be combined with other errors when drawing margins around clinical target volumes? *Br J Radiol*, 73(873):973–977, Sep 2000.

[99] Alan McKenzie, Marcel van Herk, and Ben Mijnheer. Margins for geometric uncertainty around organs at risk in radiotherapy. *Radiother Oncol*, 62(3):299–307, Mar 2002.

[100] Jean M Moran, Mohamed A Elshaikh, and Theodore S Lawrence. Radiotherapy: what can be achieved by technical improvements in dose delivery? *Lancet Oncol*, 6(1):51–58, Jan 2005.

[101] Suresh K Mukherji, Alicia Y Toledano, Clifford Beldon, Ilona M Schmalfuss, Jay S Cooper, JoRean D Sicks, Robert Amdur, Scott Sailer, Laurie A Loevner, Phil Kousouboris, and Kian Ang. Interobserver reliability of computed tomography-derived primary tumor volume measurement in patients with supraglottic carcinoma. *Cancer*, 103(12):2616–2622, Jun 2005.

[102] Issam El Naqa, Deshan Yang, Aditya Apte, Divya Khullar, Sasa Mutic, Jie Zheng, Jeffrey D Bradley, Perry Grigsby, and Joseph O Deasy. Concurrent multimodality image segmentation by active contours for radiotherapy treatment planning. *Med Phys*, 34(12):4738–4749, Dec 2007.

[103] Ursula Nestle, Stephanie Kremp, Andrea Schaefer-Schuler, Christiane Sebastian-Welsch, Dirk Hellwig, Christian Rübe, and Carl-Martin Kirsch. Comparison of different methods for delineation of 18f-fdg pet-positive tissue for target volume definition in radiotherapy of patients with non-small cell lung cancer. *J Nucl Med*, 46(8):1342–1348, Aug 2005.

[104] Jasper Nijkamp, Maurits Swellengrebel, Birgit Hollmann, Rianne de Jong, Corrie Marijnen, Corine van Vliet-Vroegindeweij, Baukelien van Triest, Marcel van Herk, and Jan-Jakob Sonke. Repeat ct assessed ctv variation and ptv margins for short- and long-course pre-operative rt of rectal cancer. *Radiother Oncol*, 102(3):399–405, Mar 2012.

[105] Jorge Nocedal. Updating quasi-newton matrices with limited storage. *Mathematics of Computation*, 35(151):773–782, July 1980.

[106] Hildur Olafsdóttir, Stephanie Lanche, Tron A Darvann, Nuno V Hermann, Rasmus Larsen, Bjarne K Ersbøll, Estanislao Oubel, Alejandro F Frangi, Per Larsen, Chad A Perlyn, Gillian M Morriss-Kay, and Sven Kreiborg. A point-wise quantification of asymmetry using deformation fields: application to the study of the crouzon mouse model. *Med Image Comput Comput Assist Interv*, 10(Pt 2):452–459, 2007.

[107] Oline Vinter Olesen, Rasmus Larsen, and Rasmus Reinhold Paulsen. *Markerless 3D Head Tracking for Motion Correction in High Resolution PET Brain Imaging*. Technical University of Denmark (DTU), 2011.

[108] Michel Ollers, Geert Bosmans, Angela van Baardwijk, Andre Dekker, Philippe Lambin, Jaap Teule, Willie Thimister, Ali Rhamy, and Dirk De Ruysscher. The integration of pet-ct scans from different hospitals into radiotherapy treatment planning. *Radiother Oncol*, 87(1):142–146, Apr 2008.

[109] Stanley Osher and Nikos Paragios. *Geometric Level Set Methods in Imaging,Vision,and Graphics*. Springer-Verlag New York, Inc., Secaucus, NJ, USA, 2003.

[110] Stanley Osher and James A Sethian. Fronts propagating with curvature-dependent speed: Algorithms based on hamilton-jacobi formulations. *Journal of Computational Physics*, 79(1):12–49, nov 1988.

[111] Brent C Parker, Almon S Shiu, Moshe H Maor, Frederick F Lang, H. Helen Liu, R. Allen White, and John A Antolak. Ptv margin determination in conformal srt of intracranial lesions. *J Appl Clin Med Phys*, 3(3):176–189, 2002.

[112] D. M. Parkin, L. Boyd, and L. C. Walker. 16. the fraction of cancer attributable to lifestyle and environmental factors in the uk in 2010. *Br J Cancer*, 105 Suppl 2:S77–S81, Dec 2011.

[113] V. Pekar, S. Allaire, J. Kim, and D. Jaffray. Head and neck auto-segmentation challenge. 11 2009.

[114] Vladimir Pekar, St´ephane Allaire, Arish A. Qazi, John J. Kim, and David A. Jaffray. Segmenting the parotid gland using registration and level set methods. *Workshop Proceedings from the 13th International Conference on Medical Image Computingand Computer Assisted Intervention, Medical Image Analysis for the Clinic: A Grand Challenge*, pages 273–280, 2010.

[115] Gitte Fredberg Persson. Uncertainties in target definition for radiotherapy of peripheral lung tumours. *Dan Med Bull*, 58(8):B4314, Aug 2011.

[116] Gitte Fredberg Persson, Ditte Eklund Nygaard, Anders Peter Roed, Christian Hollensen, Lene Sonne, Anne Kirkebjerg Due, Anne Kiil Berthelsen, Jan Nyman, Elena Markova, Henrik Roed, Per Munck af Rosenschöld, Stine Korreman, and Lena Specht. Inter-observer delineation uncertainty in radiotherapy of peripheral lung tumours (in press). *British Journal of Radiology*.

[117] Jens Petersen, Mads Nielsen, Pechin Lo, Zaigham Saghir, Asger Dirksen, and Marleen de Bruijne. Optimal graph based segmentation using flow lines with application to airway wall segmentation. *Information Processing in Medical Imaging*, 22:49–60, 2011.

[118] J.P.W. Pluim, J.B.A. Maintz, and M.A. Viergever. Mutual-information-based registration of medical images: a survey. *Medical Imaging, IEEE Transactions on*, 22(8):986–1004, 2003.

[119] Ian Poon, Nancy Fischbein, Nancy Lee, Pamela Akazawa, Ping Xia, Jeanne Quivey, and Theodore Phillips. A population-based atlas and clinical target volume for the head-and-neck lymph nodes. *Int J Radiat Oncol Biol Phys*, 59(5):1301–1311, Aug 2004.

[120] Arish A Qazi, Vladimir Pekar, John Kim, Jason Xie, Stephen L Breen, and David A Jaffray. Auto-segmentation of normal and target structures in head and neck ct images: a feature-driven model-based approach. *Med Phys*, 38(11):6160–6170, Nov 2011.

[121] Liliane Ramus and Gregoire Malandain. Multi-atlas based segmentation: Application to the head and neck region for radiotherapy planning. *Workshop Proceedings from the 13th International Conference on Medical Image Computingand Computer Assisted Intervention, Medical Image Analysis for the Clinic: A Grand Challenge*, pages 281–288, 2010.

[122] Coen Rasch, Avraham Eisbruch, Peter Remeijer, Luc Bos, Mischa Hoogeman, Marcel van Herk, and Joos V Lebesque. Irradiation of paranasal sinus tumors, a delineation and dose comparison study. *Int J Radiat Oncol Biol Phys*, 52(1):120–127, Jan 2002.

[123] Adam C Riegel, Anthony M Berson, Sylvie Destian, Tracy Ng, Lawrence B Tena, Robin J Mitnick, and Ping S Wong. Variability of gross tumor volume delineation in head-and-neck cancer using ct and pet/ct fusion. *Int J Radiat Oncol Biol Phys*, 65(3):726–732, Jul 2006.

[124] T Rohlfing. *Handbook of Biomedical Image Analysis Quo vadis, atlas-based segmentation?* Springer, 2005.

[125] Torsten Rohlfing, Robert Brandt, Randolf Menzel, and Calvin R Maurer. Evaluation of atlas selection strategies for atlas-based image segmentation with application to confocal microscopy images of bee brains. *Neuroimage*, 21(4):1428–1442, Apr 2004.

[126] Torsten Rohlfing, Calvin R Maurer, David A Bluemke, and Michael A Jacobs. Volume-preserving nonrigid registration of mr breast images using free-form deformation with an incompressibility constraint. *IEEE Trans Med Imaging*, 22(6):730–741, Jun 2003.

[127] Ruprecht and Muller. Free form deformation with scattered data interpolation methods. *Computing, Suppl. (Austria)*, (8):267–281, 1993.

[128] Andrea Schaefer, Stephanie Kremp, Dirk Hellwig, Christian Rübe, Carl-Martin Kirsch, and Ursula Nestle. A contrast-oriented algorithm for fdg-pet-based delineation of tumour volumes for the radiotherapy of lung cancer: derivation from phantom measurements and validation in patient data. *Eur J Nucl Med Mol Imaging*, 35(11):1989–1999, Nov 2008.

[129] Dominic A X Schinagl, Wouter V Vogel, Aswin L Hoffmann, Jorn A van Dalen, Wim J Oyen, and Johannes H A M Kaanders. Comparison of five segmentation tools for 18f-fluoro-deoxy-glucose-positron emission tomography-based target volume definition in head and neck cancer. *Int J Radiat Oncol Biol Phys*, 69(4):1282–1289, Nov 2007.

[130] T. Shepherd, M. Teras, R. Beichel, R. Boellaard, M. Bruynooghe, V. Dicken, M. Gooding, P. Julyan, J. Lee, and S. Lefevre. Comparative study with new accuracy metrics for target volume contouring in pet image guided radiation therapy. *IEEE Trans Med Imaging*, Jun 2012.

[131] P. C. Shrimpton, M. C. Hillier, M. A. Lewis, and M. Dunn. National survey of doses from ct in the uk: 2003. *Br J Radiol*, 79(948):968–980, Dec 2006.

[132] M. L. Siker, W. A. Tomé, and M. P. Mehta. Tumor volume changes on serial imaging with megavoltage ct for non-small-cell lung cancer during intensity-modulated radiotherapy: how reliable, consistent, and meaningful is the effect? *International Journal of Radiation Oncology Biology Physics*, 66(1):135–141, September 2006.

[133] Marcin Sikora, Jan Muzik, Matthias Söhn, Martin Weinmann, and Markus Alber. Monte carlo vs. pencil beam based optimization of stereotactic lung imrt. *Radiat Oncol*, 4:64, 2009.

[134] Richard Sims, Aurelie Isambert, Vincent Grégoire, François Bidault, Lydia Fresco, John Sage, John Mills, Jean Bourhis, Dimitri Lefkopoulos, Olivier Commowick, Mehdi Benkebil, and Grégoire Malandain. A preclinical assessment of an atlas-based automatic segmentation tool for the head and neck. *Radiother Oncol*, 93(3):474–478, Dec 2009.

[135] Milan Sonka and J. Michael Fitzpatrick, editors. *Handbook of Medical Imaging,*, volume 2. Spie Press, 2004.

[136] Liza J. Stapleford., Joshua D. Lawson, Charles Perkins, Scott Edelman ., Lawrence Davis, Mark W. McDonald, Anthony Waller, Eduard Schreibmann, and Tim Fox. Evaluation of automatic atlas-based lymph node segmentation for head-and-neck cancer, March 2010.

[137] Roel J H M Steenbakkers, Joop C Duppen, Isabelle Fitton, Kirsten E I Deurloo, Lambert J Zijp, Emile F I Comans, Apollonia L J Uitterhoeve, Patrick T R Rodrigus, Gijsbert W P Kramer, Johan Bussink, Katrien De Jaeger, José S A Belderbos, Peter J C M Nowak, Marcel van Herk, and Coen R N Rasch. Reduction of observer variation using matched ct-pet for lung cancer delineation: a three-dimensional analysis. *International Journal of Radiation Oncology Biology Physics*, 64(2):435–448, Feb 2006.

[138] J. C. Stroom, H. C. de Boer, H. Huizenga, and A. G. Visser. Inclusion of geometrical uncertainties in radiotherapy treatment planning by means of coverage probability. *Int J Radiat Oncol Biol Phys*, 43(4):905–919, Mar 1999.

[139] M. Styner, S. Xu, M. El-Sayed, and G. Gerig. Correspondence evaluation in local shape analysis and structural subdivision. In *Biomedical Imaging: From Nano to Macro, 2007. ISBI 2007. 4th IEEE International Symposium on*, pages 1192–1195. IEEE, 2007.

[140] Chengjun Sun and William G. Wee. Neighboring gray level dependence matrix for texture classification. *Computer Vision, Graphics, and Image Processing*, 23:341–352, 1982.

[141] Xiaoou Tang. Texture information in run-length matrices. *IEEE Transactions on image processing*, 7(11):1602–1609, Nov 1998.

[142] Chia-Chi Teng, Linda G. Shapiro, Linda G. Shapiro, Ira Kalet, and Ira Kalet. Head and neck lymph node region delineation using a hybrid image registration method. *IEEE Int. Symp. Biomed. Imag. Nano Macro Proc.*, 2006:462–465, 2006.

[143] J.-P. Thirion. Image matching as a diffusion process: an analogy with maxwell's demons. *Medical Image Analysis*, 2(3):243–260, 1998.

[144] A. Gordon Handford Thomas J. Nowak, editor. *Pathophysiology: concepts and applications for health care professionals.* McGraw-Hill Higher Education, 2003.

[145] J.A. van Dalen, A.L. Hoffmann, V. Dicken, W.V. Vogel, B. Wiering, T.J. Ruers, N. Karssemeijer, and W.J.G. Oyen. A novel iterative method for lesion delineation and volumetric quantification with fdg pet. *Nuclear medicine communications*, 28(6):485, 2007.

[146] M. van Herk, P. Remeijer, C. Rasch, and J. V. Lebesque. The probability of correct target dosage: dose-population histograms for deriving treatment margins in radiotherapy. *Int J Radiat Oncol Biol Phys*, 47(4):1121–1135, Jul 2000.

[147] Marcel van Herk. Errors and margins in radiotherapy. *Semin Radiat Oncol*, 14(1):52–64, Jan 2004.

[148] Marcel van Herk, Peter Remeijer, and Joos V Lebesque. Inclusion of geometric uncertainties in treatment plan evaluation. *Int J Radiat Oncol Biol Phys*, 52(5):1407–1422, Apr 2002.

[149] Marcel van Herk, Marnix Witte, Joris van der Geer, Christoph Schneider, and Joos V Lebesque. Biologic and physical fractionation effects of random geometric errors. *Int J Radiat Oncol Biol Phys*, 57(5):1460–1471, Dec 2003.

[150] Judith van Loon, Christian Siedschlag, Joep Stroom, Hans Blauwgeers, Robert-Jan van Suylen, Joost Knegjens, Maddalena Rossi, Angela van Baardwijk, Liesbeth Boersma, Houke Klomp, Wouter Vogel, Sjaak Burgers, and Kenneth Gilhuijs. Microscopic disease extension in three dimensions for non-small-cell lung cancer: development of a prediction model using pathology-validated positron emission tomography and computed tomography features. *Int J Radiat Oncol Biol Phys*, 82(1):448–456, Jan 2012.

[151] Varian. Linac illustration, November 2012.

[152] Hansjörg Vees, Srinivasan Senthamizhchelvan, Raymond Miralbell, Damien C Weber, Osman Ratib, and Habib Zaidi. Assessment of various strategies for 18f-fet pet-guided delineation of target volumes in high-grade glioma patients. *Eur J Nucl Med Mol Imaging*, 36(2):182–193, Feb 2009.

[153] Martin Vester-Christensen, Søren G. Erbou, Sune Darkner, and Rasmus Larsen. Accelerated 3d image registration. *SPIE Medical Imaging*, 2007.

[154] Cornelia Walter, Judit Boda-Heggemann, Hansjörg Wertz, Iris Loeb, Angelika Rahn, Frank Lohr, and Frederik Wenz. Phantom and in-vivo measurements of dose exposure by image-guided radiotherapy (igrt): Mv portal images vs. kv portal images vs. cone-beam ct. *Radiother Oncol*, 85(3):418–423, Dec 2007.

[155] Warfield, Zou, and Wells. Simultaneous truth and performance level estimation (staple): an algorithm for the validation of image segmentation. *IEEE Trans. Med. Imaging*, 23(7):903–921, 2004.

[156] S. Webb and A. E. Nahum. A model for calculating tumour control probability in radiotherapy including the effects of inhomogeneous distributions of dose and clonogenic cell density. *Phys Med Biol*, 38(6):653–666, Jun 1993.

[157] W. A. Weber, N. Avril, and M. Schwaiger. Relevance of positron emission tomography (pet) in oncology. *Strahlenther Onkol*, 175(8):356–373, Aug 1999.

[158] W.A. Weber, V. P., B. Schmidt, L. Tyndale-Hines, T. Link, C. Peschel, and M. Schwaiger. Positron emission tomography in non-small-cell lung cancer: prediction of response to chemotherapy by quantitative assessment of glucose use. *Journal of Clinical Oncology*, 21(14):2651–2657, July 2003.

[159] H. R. Withers, J. M. Taylor, and B. Maciejewski. Treatment volume and tissue tolerance. *Int J Radiat Oncol Biol Phys*, 14(4):751–759, Apr 1988.

[160] X. Wu and D. Chen. Optimal net surface problems with applications. *LNCS*, 2380:775–775, 2002.

[161] Jinzhong Yang, Yongbin Zhang, Lifei Zhang, and Lei Dong. Automatic segmentation of parotids from ct scans using multiple atlases. *Workshop Proceedings from the 13th International Conference on Medical Image Computingand Computer Assisted Intervention, Medical Image Analysis for the Clinic: A Grand Challenge*, pages 323–330, 2010.

[162] Y. Yin, Q. Song, and M. Sonka. Electric field theory motivated graph construction for optimal medical image segmentation. In *Proceedings of the 7th IAPR-TC-15 International Workshop on Graph-Based Representations in Pattern Recognition*, pages 334–342, 2009.

[163] Huan Yu, Curtis Caldwell, Katherine Mah, and Daniel Mozeg. Coregistered fdg pet/ct-based textural characterization of head and neck cancer for radiation treatment planning. *IEEE Trans Med Imaging*, 28(3):374–383, Mar 2009.

[164] Huan Yu, Curtis Caldwell, Katherine Mah, Ian Poon, Judith Balogh, Robert MacKenzie, Nader Khaouam, and Romeo Tirona. Automated radiation targeting in head-and-neck cancer using region-based texture analysis of pet and ct images. *Int J Radiat Oncol Biol Phys*, 75(2):618–625, Oct 2009.

[165] Marco Zaider and Leonid Hanin. Tumor control probability in radiation treatment. *Med Phys*, 38(2):574–583, Feb 2011.

[166] Habib Zaidi and Issam El Naqa. Pet-guided delineation of radiation therapy treatment volumes: a survey of image segmentation techniques. *Eur J Nucl Med Mol Imaging*, 37(11):2165–2187, Nov 2010.

[167] Tiezhi Zhang, Yuwei Chi, Elisa Meldolesi, and Di Yan. Automatic delineation of on-line head-and-neck computed tomography images: toward on-line adaptive radiotherapy. *Int J Radiat Oncol Biol Phys*, 68(2):522–530, Jun 2007.

[168] X. Zhang, J. Tian, Y. Wu, J. Zheng, and K. Deng. Segmentation of head and neck ct scans using atlas-based level set method. 08 2009.